Building-Integrated Solar Energy Devices based on Wavelength Selective Films

A THESIS SUBMITTED TO THE FACULTY OF THE GRADUATE SCHOOL OF

THE UNIVERSITY OF MINNESOTA BY

Tejas Ulavi

IN PARTIAL FULFILLMENT OF THE REQUIREMENTS FOR THE DEGREE OF

MASTER OF SCIENCE

Dr. Jane H. Davidson, Adviser

June, 2013

Acknowledgements

Abstract

A potentially attractive option for building integrated solar is to employ hybrid solar collectors which serve dual purposes, combining solar thermal technology with either thin film photovoltaics or daylighting. In this study, two hybrid concepts, a hybrid photovoltaic/thermal (PV/T) collector and a hybrid 'solar window', are presented and analyzed to evaluate technical performance. In both concepts, a wavelength selective film is coupled with a compound parabolic concentrator (CPC) to reflect and concentrate the infrared portion of the solar spectrum onto a tubular absorber. The visible portion of the spectrum is transmitted through the concentrator to either a thin film Cadmium Telluride (CdTe) solar panel for electricity generation or into the interior space for daylighting. Special attention is given to the design of the hybrid devices for aesthetic building integration. An adaptive concentrator design based on asymmetrical truncation of CPCs is presented for the hybrid solar window concept.

The energetic and spectral split between the solar thermal module and the PV or daylighting module are functions of the optical properties of the wavelength selective film and the concentrator geometry, and are determined using a Monte Carlo Ray-Tracing (MCRT) model. Results obtained from the MCRT can be used in conjugation with meteorological data for specific applications to study the impact of CPC design parameters including the half-acceptance angle θ_c, absorber diameter D and truncation on the annual thermal and PV/daylighting efficiencies.

The hybrid PV/T system is analyzed for a rooftop application in Phoenix, AZ. Compared to a system of the same area with independent solar thermal and PV modules, the hybrid PV/T provides 20% more energy, annually. However, the increase in total

delivered energy is due solely to the addition of the thermal module and is achieved at an expense of a decrease in the annual electrical efficiency from 8.8% to 5.8% due to shading by the absorber tubes. For this reason, the PV/T hybrid is not recommended over other options in new installations.

The hybrid solar window is evaluated for a horizontal skylight and south and east facing vertical windows in Minneapolis, MN. The predicted visible transmittance for the solar window is 0.66 to 0.73 for single glazed systems and 0.61 to 0.67 for double glazed systems. The solar heat gain coefficient and the U-factor for the window are comparable to existing glazing technology. Annual thermal efficiencies of up to 24% and 26% are predicted for the vertical window and the horizontal skylight respectively. Experimental measurements of the solar thermal component of the window confirm the trends of the model. In conclusion, the hybrid solar window combines the functionality of an energy efficient fenestration system with hybrid thermal energy generation to provide a compelling solution towards sustainable design of the built environment.

Table of Contents

List of Tables

List of Figures

Chapter 1

Introduction

Buildings are the primary sinks of global energy resources. Figure 1.1 shows that out of the 19% total world energy consumption represented by the US, commercial and residential building sectors collectively contribute to 41%. Only 9% of the energy consumption in the building sector is obtained from sustainable sources of energy (hydroelectric, wood, solar, wind, geothermal). Solar energy represents less than 1% of this portion [1]. Challenges associated with solar technology include low efficiency of solar electricity, availability of less expensive conventional fossil fuel based sources of energy and a lack of architecturally aesthetic and functional building integrated solar energy collection and distribution systems. As relatively mature solar technologies such as solar thermal systems for domestic hot water and solar photovoltaics decline in costs, it is important to adapt the built environment to harness the solar resource. Ideally, sustainable building design will entail the integration of these devices to exterior walls or roofs consistent with the overall architectural intent of the building.
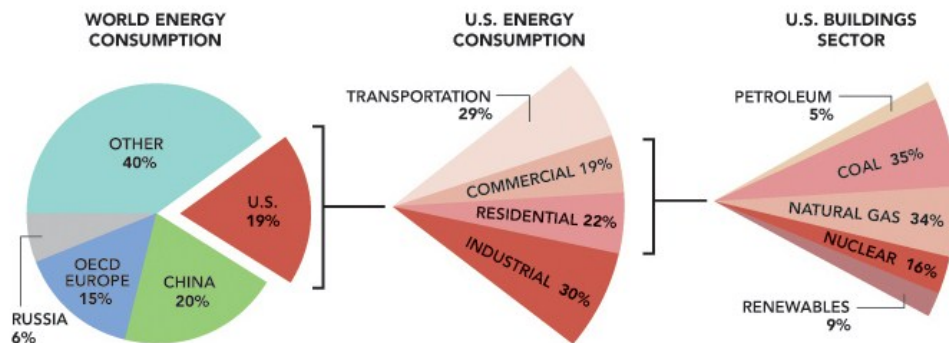
Fig. 1.1 Overview of U.S energy consumption [1]

In the present work, two concepts are presented for hybrid solar energy generation with special attention to aesthetics and building integration. The concepts were conceived to use wavelength selective films developed by the 3M Companies. Specifically, the film of interest has a high transmission band in the visible portion of the solar spectrum, which closely matches the quantum efficiency curve for a Cadmium Telluride (CdTe) solar cell, and a high reflectance band in the near infrared (for wavelengths up to 1850nm). For the present study, the wavelength selective film is utilized in combination with non-tracking compound parabolic concentrators to concentrate the infrared spectrum on an absorber tube to produce sensible heat. The transmitted visible spectrum is used for two alternative applications: to generate electricity via thin film CdTe, or for daylighting an interior space.

This thesis is organized into two papers that are self-sustaining in scope and presentation and can be read independently. The papers share common design principles and analysis techniques. Chapter 2 consists of a paper submitted at the ASME Energy Sustainability 2013 conference. It presents and analyzes a hybrid photovoltaic/thermal (PV/T) collector. Chapter 3 analyzes an architecturally integrated hybrid solar window design that generates useful thermal energy that can be used to heat water, in addition to the primary function of daylighting the interior space. The paper presented in Chapter 3 has been submitted to the Solar Energy (Elseiver). A prototype of the solar window was built and tested. Preliminary results for the thermal efficiency of the built prototype are presented in Chapter 4. Chapter 5 presents the overall conclusions of the research and recommendations for future work. A bibliography is presented at the end of each chapter.

References

[1] DOE. Buildings Energy Data Book, Chapter 1 Buildings Sector. United States Department of Energy, 2011

Chapter 2

Analysis of a Hybrid PV/T Concept based on a Wavelength Selective Film[1]

The technical performance of a non-tracking hybrid PV/T concept that uses a wavelength selective film is modeled. The wavelength selective film is coupled with a compound parabolic concentrator to reflect and concentrate the infrared portion of the solar spectrum onto a tubular absorber while transmitting the visible portion of the spectrum to an underlying thin-film photovoltaic module. The optical performance of the CPC/selective film is obtained through Monte Carlo Ray-Tracing. The CPC geometry is optimized for maximum total energy generation for a roof-top application. Applied to a rooftop in Phoenix, Arizona USA, the hybrid PV/T provides 20% more energy compared to a system of the same area with independent solar thermal and PV modules, but the increase is achieved at the expense of a decrease in the electrical efficiency from 8.8% to 5.8%.

2.1 Introduction

Hybrid collectors incorporating solar energy conversion to both thermal energy and electricity within a single device are popularly referred to as PV/T systems [1-3]. Non-tracking PV/T systems are an enticing concept for buildings where there is demand for space heating, hot water and electrical energy, and where roof space is limited [4, 5].

---

[1]This paper was co-authored by Tim Hebrink and Jane H. Davidson

Concentrating PV/T collectors have been considered to extract more energy from a given solar cell area [6-8], but require tracking and are thus not as attractive for residential buildings as they are for commercial applications. Two general approaches have been proposed to manage the thermal and electrical performance in such hybrid systems.

In the first and most common approach, the PV is cooled via buoyancy-driven or forced flow using a liquid (usually water) [4-13], air [14-17] or a combination [18]. Most PV/T concepts employ glazing to achieve higher thermal efficiency, at the expense of lowering of the electrical efficiency [9-12]. Zondag et al. [9] predicted the annual performance of nine PV/T concepts using a PV laminate with a predicted annual efficiency of 7.2%. For implementation in The Netherlands, predicted efficiencies are 7.6%/24% for unglazed and 6.1-6.6%/38-35% for glazed PV/T. The range reported for glazed collectors is due to differences in position and geometry of the cooling channel. Recently, Dupeyrat et al. [13] proposed the use of fluorinated ethylene propylene (FEP) lamination to replace PV glass covers, and alternate PV encapsulation material to improve the optical performance of liquid PV/T systems.

In the second approach, the insolation is split into spectral bands optimized for each generation technology. The PV operating temperature is lowered if the spectrum of the incident radiation matches the quantum efficiency band of the PV cell. The radiant energy outside this band can be converted to heat via a solar thermal collector. Spectral filters are classified as multilayer filters (present work), liquid absorptive filters, heat mirrors, prism spectrum splitters, luminescent filters, or holographic filters [19]. System development is limited by cost constraints and various limitations relating to application of spectrum splitting optics to real systems [19, 20]. Among the optical limitations is the

5

reduction in filter performance at incident angles different from the design angle [20]. To counter this issue in tracking applications, dish receivers or heliostat field receivers have been used to limit the range of incident angles at the beam splitter [21, 22]. Although a number of innovative concept designs have been proposed for compact collectors utilizing beam splitting [23], none has been commercialized.

In the present study, we consider using spectral band splitting for a non-tracking hybrid collector intended for building applications (Fig. 2.1). A wavelength selective film is attached to a compound parabolic concentrator (CPC) which concentrates the infrared portion of the solar spectrum on to an absorber tube while transmitting the visible portion to a thin film PV module. A Monte-Carlo ray tracing (MCRT) model predicts the optical performance of the CPC with a wavelength selective film, and the energetic and spectral split between the PV and thermal modules as a function of incidence angle for a range of CPC geometries as defined by the half acceptance angle, tube diameter and degree of truncation. The results of the MCRT can be used in conjugation with meteorological data to calculate the annual and electrical collector efficiencies. A roof-top collector for Phoenix, AZ is considered in the present study. A parametric study optimizes the half-acceptance angle, the tube diameter and the concentration factor of the CPC for maximum total energy generation. Finally, a case study is presented which compares the annual efficiency of the hybrid collector to an independent system of thermal and PV modules.

2.2 PV/T Design

The concentrator geometry, the type of the PV module and the optical properties of the wavelength selective film are the major design parameters. Here, we consider a
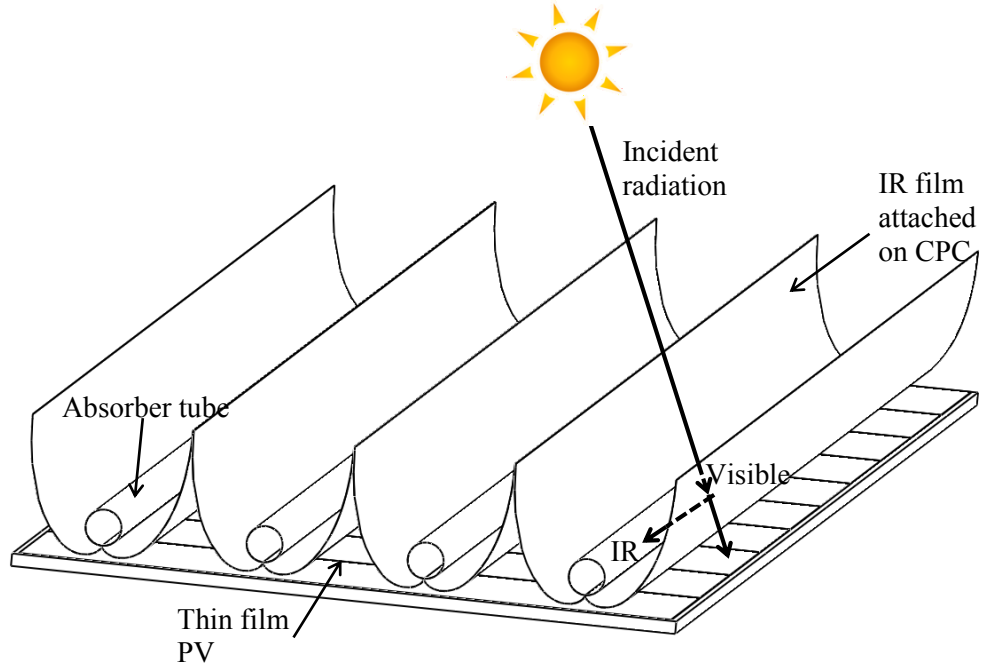
Fig. 2.1 Design concept for the hybrid PV/T collector

hybrid collector with 2m x 1m aperture area. The height is constrained to 0.13m for aesthetic installation on residential or commercial rooftops. A thin film CdTe film is selected for the PV module to match the characteristics of the wavelength selective film.

The CPC concentrator is geometrically defined by the tube diameter D, the nominal half-acceptance angle θ_c and the effective geometrical concentration factor C_e, or truncation (Fig. 2.2) [24]. For a perfectly specular concentrator surface, all radiation within the acceptance angle is collected at the absorber tube. The tube diameter D determines the size of the concentrator, and the nominal half-acceptance angle θ_c determines the maximum geometric concentration factor for the nominal CPC,

$$C_{max} = \frac{1}{\sin \theta_c} \tag{2.1}$$

The truncation of the top portion of a CPC is common practice to save reflector
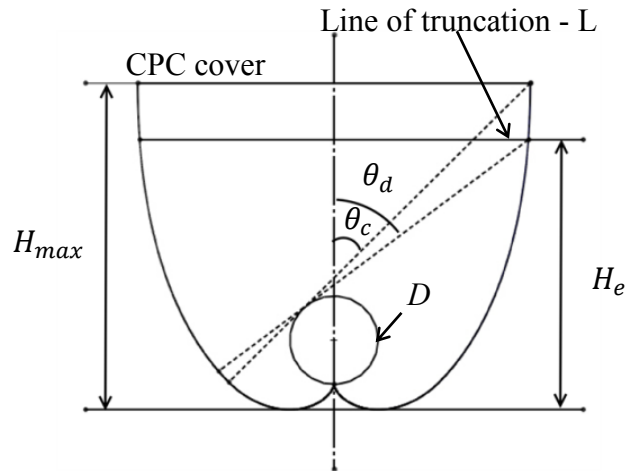
Fig. 2.2 CPC geometry – Nominal and truncated parameters

material and to reduce the vertical dimension of the CPC. The truncation results in lower

geometric concentration, but modifies the field of view of the concentrator to allow

diffuse radiation outside the nominal half-acceptance angle to reach the absorber [25].

Figure 2.2 graphically shows the effect of truncation. θ_c and H_{max} represent the nominal

parameters of the CPC, yielding a geometric concentration factor given by Eq. (2.1). The

line L truncates the CPC symmetrically to yield the truncated parameters: θ_d, the

truncated half-acceptance angle and H_e, the effective truncated height of the CPC. With

truncation, the effective geometric concentration factor is C_e, defined as the ratio of

truncated aperture area and the area of the absorber.

The wavelength selective film belongs to a group of infrared reflective mirrors

that utilize constructive quarter-wave interference in multi-layer optical films

comprising multiple layers of transparent dielectric materials. Alternating layers of high

refractive index polymers and low refractive index polymers are coextruded into optical

stacks containing 100 to 1000 layers with layer thicknesses of approximately a quarter of

the wavelength of radiation to be reflected [26]. The manufacturer has developed

coextrusion and orientation processes that yield layer thickness control at the nanometer

scale. Each polymer layer pair contains polymers of differing refractive indices and works constructively with the next layer to create broad reflection bands. Figure 2.3 shows the spectral reflectance for normal and 60° off-normal incidence for the wavelength selective film considered for the present study. The data for $\lambda \leq 1110$nm were measured by spectroscopy. For $\lambda > 1110$nm the curves are those expected for a selective film under development. The reflection bands shift to lower wavelengths by ~20% for 60° off-normal incidence according to Fresnel reflection and phase thickness equations. Birefringent polymers with matched z-direction (along the thickness) refractive indices are used so that the reflectivity of p-polarized light is independent of incidence angle, in spite of the band-edge shift [26]. The increase in reflectivity for s-polarized light by about 2-3% for incidence higher than 45° is neglected. The spectral absorptance for the film is negligible in the band considered.

Thin film Cadmium Telluride (CdTe) PV cells are selected for two reasons. First, as shown in Fig. 2.4, the quantum efficiency curve [27] matches the transmitted spectrum of the wavelength selective film at normal incidence. Second, thin film cells can be arranged so that the detrimental effect of shading by the absorber tubes is minimized. Thin film solar cells can be oriented in a direction such that all cells are shaded equally, and thus current mismatch can be avoided, albeit with a reduction in electrical efficiency [28].

2.3 Numerical Approach

A 3-D Monte Carlo Ray-Tracing (MCRT) model was implemented to predict the reflectance of the CPC/selective film as a function of the direction and wavelength of the incident radiation for a range of CPC geometries. The value of these results is that they
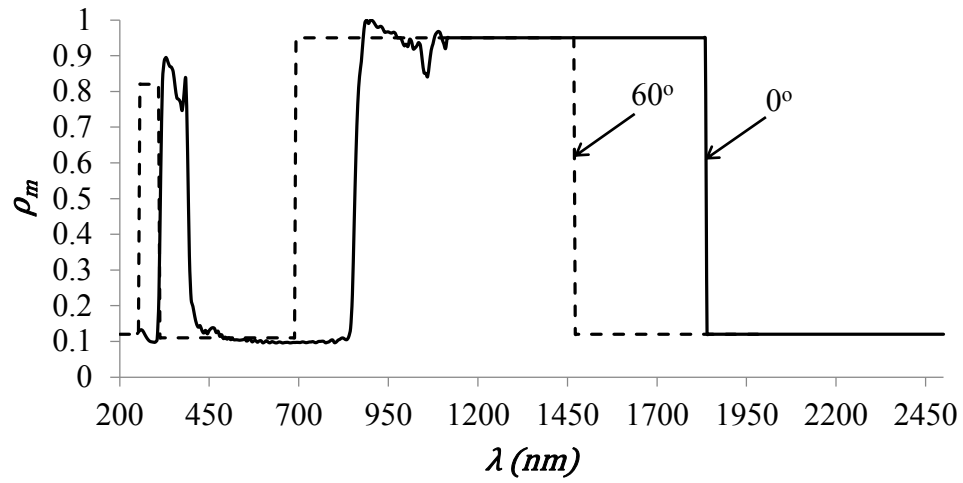
Fig. 2.3 Spectral reflectance of the wavelength selective film at 0° and 60° incidence
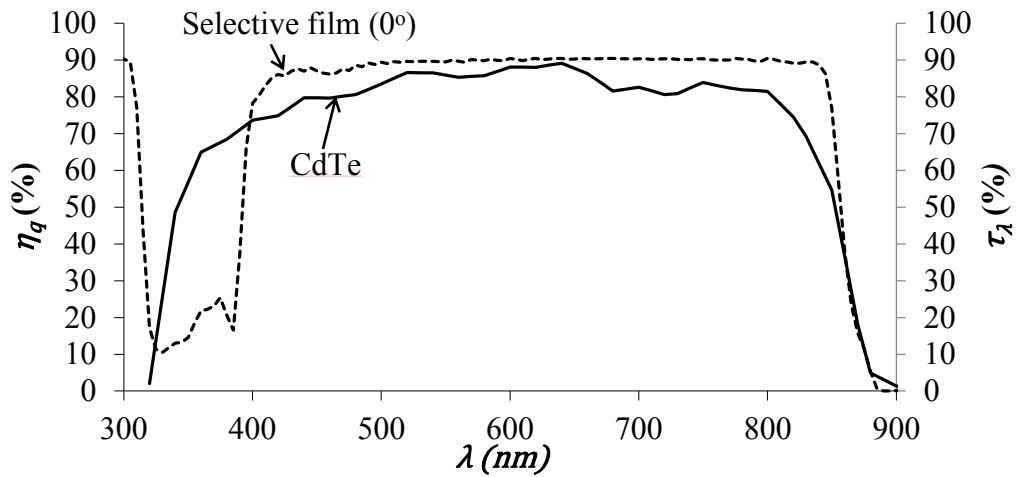
Fig. 2.4 Quantum efficiency (left) for CdTe [26] and spectral reflectance (right) for the selective film at normal incidence

can be used to determine the thermal and electrical efficiency of the collector for any roof-top application. In the present study, we selected a roof-top in Phoenix, AZ to illustrate the annual efficiency of the collector.

2.3.1 MCRT Model

The following parameters were calculated with the MCRT model:

- $\left(g_{b,\vec{r}}^T \equiv \frac{G_{b,\vec{r}}^T}{G_{b,\vec{r}}}\right)$, $\left(g_d^T \equiv \frac{G_d^T}{G_d}\right)$ – The fractions of incident beam radiation (as a function of incident direction), and incident diffuse radiation reaching the absorber tube, respectively

- $\left(g_{b,\vec{r}}^{PV} \equiv \frac{G_{b,\vec{r}}^{PV}}{G_{b,\vec{r}}}\right)$, $\left(g_d^{PV} \equiv \frac{G_d^{PV}}{G_d}\right)$ – The fractions of incident beam radiation (as a function of incident direction), and incident diffuse radiation transmitted to the PV, respectively

- $W_{\lambda,b,\vec{r}}$ and $W_{\lambda,d}$ – The PV module spectral weighting factors for beam radiation as a function of incident direction, and for diffuse radiation, respectively

The gas in the CPC was assumed to be non-participating and the reflector surface was assumed to be 1.5 mm thick, with a specular reflectance ρ_s of 0.95. The direction of the incident beam radiation, $\vec{r}$, is represented by component angles θ_{xy} and θ_{yz} in the xy and yz planes. The ray path was computed separately in the two planes and was superimposed to obtain a 3-D solution. Figure 2.5 depicts the MCRT for a single ray. Each MCRT simulation consists of a stochastically large number of rays, $N_{i,b}$ for beam radiation and $N_{i,d}$ for diffuse radiation, being launched from the cover. To achieve convergence, $N_{i,b}$ and $N_{i,d}$ are chosen as 10^5 and 10^6, respectively. Each ray has a

11

direction $(\theta_{xy}, \theta_{yz})$, an energy $\frac{G}{N_i}$, a wavelength λ_i and an origin (x_0, y_0, z_0). The origin

has a uniform random distribution over the CPC cover area. For beam radiation, a series

of MCRT simulations were performed by varying θ_{xy} and θ_{yz} from 0° to 60° in intervals

of 1° and 5° respectively, to obtain data from the entire range of directions expected in a

roof-top collector. For diffuse radiation, θ_{xy} and θ_{yz} were chosen based on standard

MCRT distributions for the zenith and azimuth angles for diffuse emission from an

isotropic surface [29]. The spectral distribution of the rays was obtained by considering

the sun to be a blackbody at 5777K [30].

The wavelength for a launched ray was selected by computing the right-hand side

of Eq. (2.2) numerically over discrete wavelength intervals of 5 nm until the value closest

to the generated random number was obtained.

$$R_\lambda = \frac{1}{\sigma T^4} \int_0^\lambda E_{b\lambda} \, d\lambda = f_{0-\lambda T} \qquad (2.2)$$
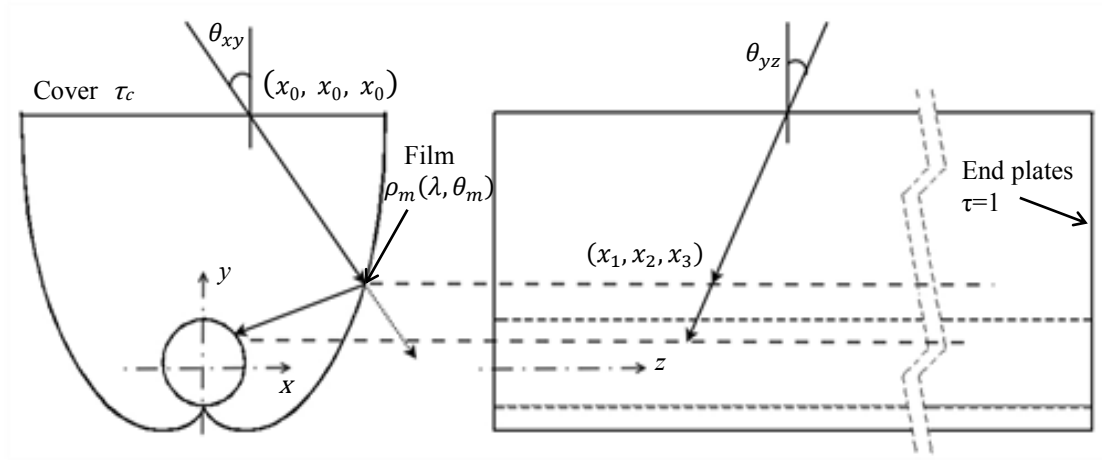
Fig. 2.5 Monte Carlo Ray-Trace in the CPC cavity

Once a ray was launched from the aperture plane, its path was traced through the CPC cavity, accounting for randomized surface interactions within the cavity until the ray either (i) struck the absorber tube, (ii) was transmitted to the PV module or (iii) was lost through the cover or ends of the CPC. The path of the ray in the xy and yz planes can be represented by straight lines. The intersection of the ray with the cover and the absorber were calculated by simple geometrical relations. Intersection with the CPC was calculated numerically using the equation of the CPC curve for tubular absorbers defined in [31].

Whenever the ray intersected a surface, a random reflectance R_ρ was generated to determine a statistically meaningful outcome over the large sample of rays – either reflection or transmission at the cover or the CPC/selective film, based on the surface properties. The transmittance of the cover τ_c is based on Snell's law for refraction and Bouguer's law for absorption losses in the cover [32]. For the selective film, the reflectance depends upon the angle of incidence at the point of intersection, θ_m, and the wavelength λ_i. θ_m is the resultant of the intersection angles in the xy and the yz planes. A specular error θ_s having a normal distribution with a standard deviation $\sigma_s = 3$ mrad accounts for the irregularities in the CPC surface. The film reflectance given by Eq. (2.3) was calculated in terms of film spectral reflectance at normal incidence, based on the band-edge shifts for the selective film.

$$\rho_m(\lambda, \theta_m) = \rho_m \left(\frac{\lambda}{f(\theta_m)}, 0 \right) \tag{2.3}$$

$f(\theta_m)$ is a fourth order polynomial in θ_m that has different forms for $\lambda < 1350$ nm and $\lambda > 1350$ nm, representative of the two band-edges.

13

The number and wavelength of each ray were tracked iteratively, and the fractions of beam and diffuse radiation available for the thermal and PV modules were derived from the results of the ray-tracing.

$$g_{b,\vec{r}}^{T} = \frac{N_{a,b}}{N_{i,b}}, \, g_{d}^{T} = \frac{N_{a,d}}{N_{i,d}} \qquad\qquad (2.4), (2.5)$$

$$g_{b,\vec{r}}^{PV} = \frac{N_{t,b}}{N_{i,b}}, \, g_{d}^{PV} = \frac{N_{t,d}}{N_{i,d}} \qquad\qquad (2.6), (2.7)$$

The spectral weighting factors for beam radiation and diffuse radiation, $W_{\lambda,b,\vec{r}}$ and $W_{\lambda,d}$, have a value from 0 to 1 and modify the PV module efficiency to account for transmission losses through the wavelength selective film and shading effects due to the absorber tubes. For an independent PV module without the film, the spectral weighting factors equal unity. For the present application, they are defined by Eqs. (2.8) and (2.9), weighting the spectral characteristics of the wavelength selective film by the quantum efficiency.

$$W_{\lambda,b,\vec{r}} = \frac{\sum_{N_{t,b}} \lambda_{t,b} \cdot \eta_q(\lambda_{t,b})}{\sum_{N_{i,b}} \lambda_{i,b} \cdot \eta_q(\lambda_{i,b})}, \, W_{\lambda,d} = \frac{\sum_{N_{t,d}} \lambda_{t,d} \cdot \eta_q(\lambda_{t,d})}{\sum_{N_{i,d}} \lambda_{i,d} \cdot \eta_q(\lambda_{i,d})} \qquad (2.8), (2.9)$$

2.3.2 Annual thermal and electrical efficiency

The efficiencies of the solar thermal and PV modules were calculated independently using the results obtained from the MCRT. A quasi-steady state 1-D energy balance was applied for the thermal module. A selective coating of black chrome on nickel was assumed for the absorber tubes and weighted absorptance of 0.945 was calculated [32]. A fixed fluid inlet temperature of 293K was assumed. To simplify the mathematical analysis, a number of assumptions were made. The heat flux at the absorber tube was assumed uniform over the circumference. Flow through the absorber tube was

assumed to be uniform and fully developed. Conduction losses through the low iron glass cover were neglected. The annual thermal efficiency is given by Eq. (2.10) [32].

$$\eta_{th} = \frac{1}{A_c}\Sigma_{hours}\frac{nA_aF_R[S- U_L(T_{fi}-T_\infty)]}{G} \tag{2.10}$$

The solar radiation incident on the absorber tube, S, was obtained by interpolating from the MCRT results for the direction of beam radiation obtained from the hourly TMY2 data [34], and accounting for transmittance of the low iron glass cover and the absorptance of the absorber tube.

$$S = \left(G_{b,\hat{r}}^T + G_d^T\right)\tau_c\alpha \tag{2.11}$$

The overall thermal loss coefficient U_L was computed from the equivalent thermal resistance network shown in Fig. 2.6.

$$U_L = \frac{1}{R_{th}A_a} \tag{2.12}$$

Table 2.1 lists the assumed heat transfer coefficients. The convective losses in the CPC cavity were approximated by treating the cavity as a horizontal annulus formed by eccentric cylinders [35]. An effective outer diameter D_o was calculated. An experimentally derived factor, f_{rat} having a value of 0.55 [36] was used in the calculation of the convective heat loss from the absorber to the reflector and the cover. The equivalent emittances, ε_{a-c}, ε_{a-m} and ε_{c-m} were calculated from relations derived in literature [24].

For CPCs with tubular absorbers, the heat removal factor is given by Eq. (2.13).

$$F_R = \frac{\dot{m}c_p}{A_cU_L}\left[1 - exp\left(-\frac{A_cU_LF'}{\dot{m}c_p}\right)\right] \tag{2.13}$$

where

$$F' = \left[\frac{1/U_L}{\left[\frac{1}{U_L}+\frac{D}{h_{fi}D_i}+\left(\frac{D}{2k}\ln\frac{D}{D_i}\right)\right]}\right] \tag{2.14}$$

15
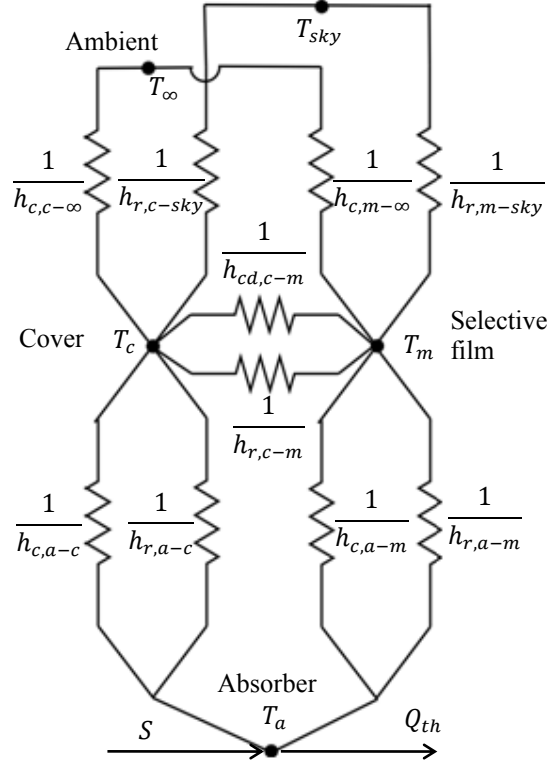
Fig. 2.6 Thermal resistive network for the thermal module

Table 2.1 Heat transfer coefficients between different components of the thermal module

Convective heat transfer	Radiative heat transfer
$h_{c,a-c} = \frac{Nu_D k_{air}}{D(1+f_{rat})}$ [35, 36]	$h_{r,a-c} = \frac{\varepsilon_{a-c}\sigma(T_a{}^4 - T_c{}^4)}{(T_a - T_c)}$ [24,36]
$h_{c,a-m} = f_{rat} \cdot h_{c,a-c}$ [36]	$h_{r,a-m} = \frac{\varepsilon_{a-m}\sigma(T_a{}^4 - T_m{}^4)}{(T_a - T_m)}$ [24,36]
$h_{c,c-\infty} = 2.8 + 3.0v_w$ [32]	$h_{r,c-b} =$ $\frac{\sigma\varepsilon_c(T_c+T_{sky})(T_c^2+T_{sky}^2)(T_c-T_{sky})}{(T_c - T_\infty)}$
$h_{cd,c-m} = 4\left(\frac{k_m t}{L^2}\right)$ [36] (Conductive heat transfer coefficient)	$h_{r,c-m} = \frac{\varepsilon_{c-m}\sigma(T_c{}^4 - T_m{}^4)}{(T_c - T_m)}$ [24,36]
$h_{c,m-\infty} = \left(0.6 + \frac{0.387Ra_{D_o}{}^{1/6}}{[1+(0.559/Pr)^{9/16}]^{8/27}}\right)^2 \frac{k_{air}}{D_o}$ [37]	$h_{r,m-b} = \frac{\varepsilon_m\sigma(T_m{}^4 - T_\infty{}^4)}{(T_m - T_\infty)}$ [24,36]

h_{fi} is the heat transfer coefficient between the fluid and inner wall of the absorber tube. For $Re < 2300$, Nu was assumed to be 4.36 for constant heat flux and fully developed flow, and for $Re > 2300$ correlations developed for turbulent flow in a smooth pipe were used [38].

The empirical model used to estimate the PV efficiency is given by Eq. (2.15) [39] where W_λ is the spectral weighting factor that accounts for the transmission losses through the wavelength selective film and shading, given by Eq. (2.16).

$$\eta_{PV} = \eta_{ref} \left\{ W_\lambda + \beta(T_{cell} - 298) + \gamma \left(\frac{G^{PV}}{1000} \right) \right\} \tag{2.15}$$

$$W_\lambda = W_{\lambda,b,\vec{r}} \frac{G_{b,\vec{r}}}{G} + W_{\lambda,d} \frac{G_d}{G} \tag{2.16}$$

n_{ref} is the reference PV module efficiency computed at standard testing conditions, and was assumed equal to 0.1234 for the thin-film CdTe [40]. The factors γ and β were chosen as 0 [39] and -0.0028°C^{-1} based on measured data [41]. Empirical relations developed for closed-rack PV installations [42] were used to determine T_{cell}. The method involves calculating the back surface temperature of the PV module, T_{back}, by Eq. (2.17), arrived at by a steady state energy balance. The coefficients (a, b) were chosen as (-2.976, -0.0471) for closed rack mountings. T_{cell} was then calculated assuming an empirically estimated temperature difference ΔT of 3 °C [42].

$$T_{back} = G^{PV} e^{(a+bv_w)} + T_\infty \tag{2.17}$$

$$T_{cell} = T_{back} + \frac{G^{PV}}{1000} \Delta T \tag{2.18}$$

The annual electrical output is

$$Q_{PV} = \eta_{PV} A_e G \tag{2.19}$$

A_e is the effective PV area that is exposed to insolation based on the direction of beam

radiation. For simplicity, the same effective area is assumed for diffuse radiation.

2.4 Results

2.4.1 Monte Carlo Ray-Trace (MCRT)

Figure 2.7 shows plots for $g_{b,\vec{r}}^{T}$, $g_{b,\vec{r}}^{PV}$ and $W_{\lambda,b,\vec{r}}$ as a function of θ_{xy} and $\theta_{yz}/4$, for

one of the geometries considered: $\theta_c = 45^{\circ}$, $D = 0.03$m, $\dot{m} = 0.015$ kg/s-m^2. The values

of the corresponding diffuse parameters are inset.

θ_{xy} and θ_c (45°) for the CPC geometry are both defined in the xy plane. Consider

the graphs at $\theta_{yz} = 0^{\circ}$ as θ_{xy} is varied from 0° to 60°. For radiation incident within the

acceptance angle ($\theta_{xy} < 45^{\circ}$), the fraction of incident radiation concentrated at the

absorber tube, $g_{b,\vec{r}}^{T}$, is 0.49-0.57 while visible radiation is transmitted to the PV module.

$g_{b,\vec{r}}^{PV}$ ranges from 0.41-0.49. For $\theta_{xy} > \theta_c$, $g_{b,\vec{r}}^{T}$ is zero as expected. In contrast, $g_{b,\vec{r}}^{PV}$

increases to 0.6-0.7 as the number of average reflections in the CPC increase and make

transmission more probable. The spectral directional weighting factor $W_{\lambda,b,\vec{r}}$ depends on

the wavelength of the transmitted radiation and has a trend similar to $g_{b,\vec{r}}^{PV}$. It ranges from

0.65 to 0.78 for $\theta_{xy} < 45^{\circ}$ and approach the ideal value of 1 for $\theta_{xy} > 45^{\circ}$, where $W_{\lambda,b,\vec{r}}$

ranges from 0.87-0.94.

As θ_{yz} is increased from 0° to 60°, more radiation is lost through both ends of the

CPC. As a result, $g_{b,\vec{r}}^{T}$, $g_{b,\vec{r}}^{PV}$ and $W_{\lambda,b,\vec{r}}$ have progressively lower values compared to the

case when $\theta_{yz} = 0^{\circ}$. The shift to lower values as θ_{yz} increases from 0° to 60° is ~2% for

$g_{b,\vec{r}}^{T}$, ~15% for $g_{b,\vec{r}}^{PV}$ and ~18% for $W_{\lambda,b,\vec{r}}$.

18
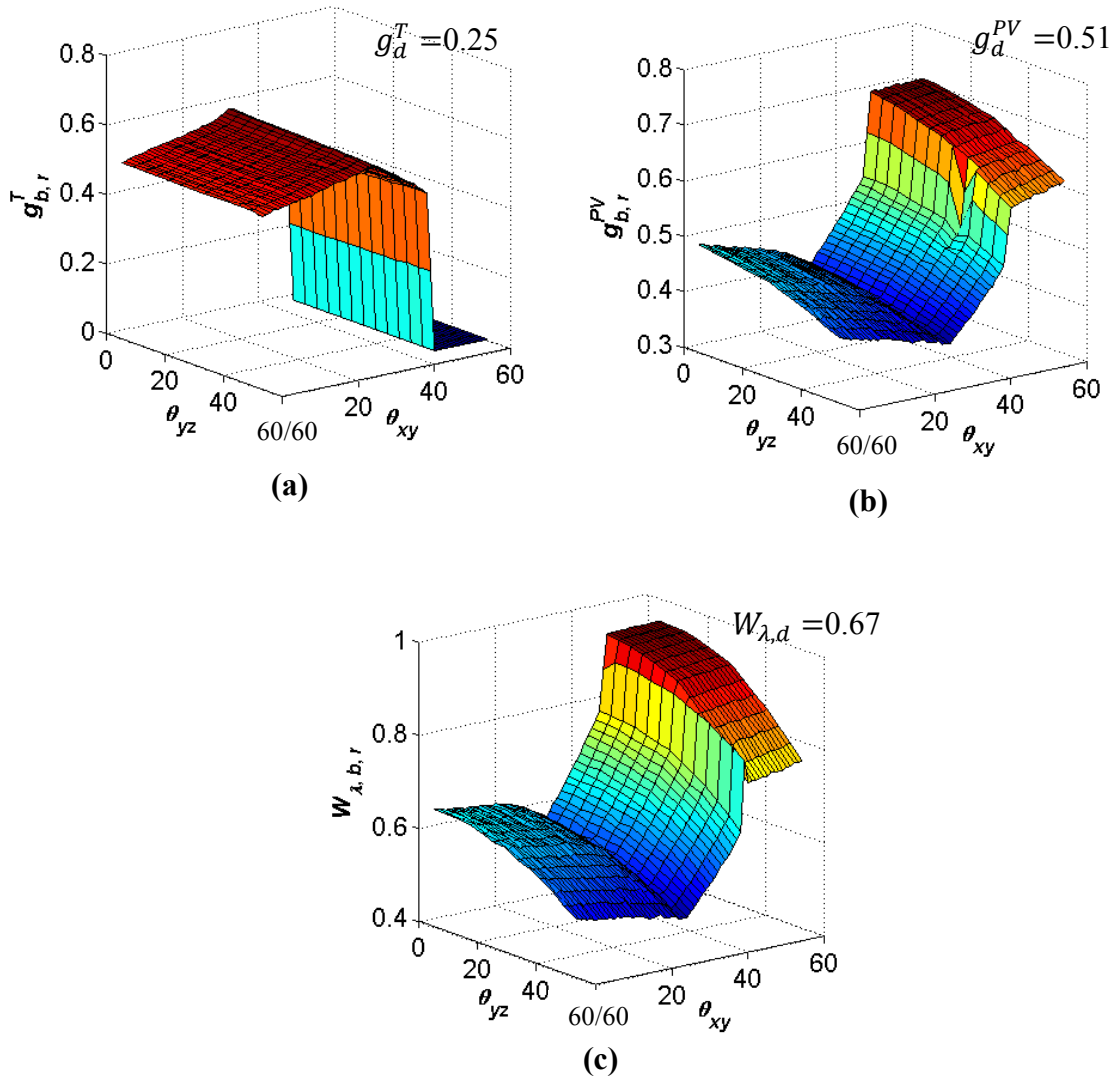
Fig. 2.7 Parameters obtained through MCRT as a function of θ_{xy} and θ_{yz} for a CPC with $\theta_c = 45^o$, $D = 0.03$m and $C_e = 1.4$ (a) $g_{b,\vec{r}}^T$, g_d^T (b) $g_{b,\vec{r}}^{PV}$, g_d^{PV} (c) $W_{\lambda,b,\vec{r}}$, $W_{\lambda,d}$

2.4.2 Parametric Study

A parametric study is presented to determine the sensitivity of the hybrid collector annual performance to θ_c (25-55°), C_e (1.2 to 2), and D (0.02-0.03m). Table 2.2 lists the fixed and variable parameters.

Effect of concentrator geometry

Figure 2.8 shows the annual thermal (left ordinate) and PV (right ordinate) efficiencies of the collector as a function of θ_c for $D = 0.03$m and $\dot{m} = 0.015$kg/s-m^2. The values of C_e corresponding to θ_c are also indicated on the abscissa. Geometries with $\theta_c < 40°$ are truncated to comply with the height restriction of 0.13m, and thus $C_e < C_{max}$. As θ_c is increased, the CPC accepts a wider angular range of incident beam radiation. Consequently, C_e decreases, allowing a larger fraction of the diffuse radiation ($\sim\frac{1}{C_e}$) to reach the absorber tube [24]. Thus, annual thermal efficiency increases with increasing θ_c. The non-linear behavior of η_{th} with respect to θ_c for $\theta_c < 40°$ is due to the effects of truncation.

The annual efficiency of the PV varies over a narrow range from 0.0585 to 0.053 as θ_c is increased from 25° to 55°. As θ_c is increased, the width of the corresponding CPC concentrator decreases. For a fixed collector aperture area, a larger number of absorbers can be accommodated, causing more shading. If the PV module were operated without the CPC, the electrical efficiency would be ~8.8% (not shown). The transmission losses through the film and the loss of efficiency due to shading outweigh the benefit of reduced operation temperature.

Table 2.2 Fixed and variable parameters for the parametric study

Fixed Parameters	Value
1. General	
Geographical Location	Phoenix, AZ
Aperture area, A_c	2 m²
Concentrator height	0.13 m
Collector orientation	E-W, facing south, slope 30º
2. Solar Thermal module	
Heat transfer fluid	Ethylene glycol 40% (v/V)
Inlet fluid temperature, T_{fi}	293K
Mass flow rate, $\dot{m}$	0.015 kg/s-m²
3. PV module	
PV module type	Thin film CdTe
PV reference efficiency, η_{ref}	12.34%
Variable Parameters	
Half-acceptance angle, θ_c	25º – 55º
Effective concentration factor, C_e	1.2, 1.4, 1.7, 2.0
Tube diameter, D	0.02m, 0.025m, 0.03m
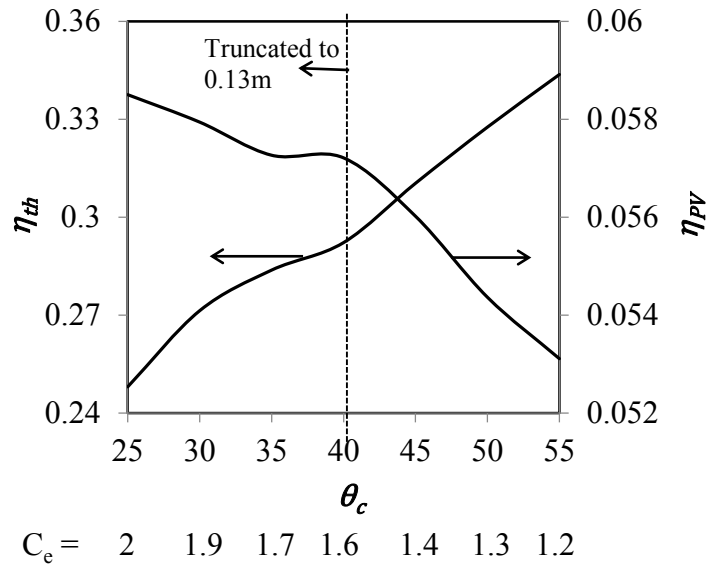
Fig. 2.8 Annual thermal (left) and PV (right) efficiency, $D = 0.03$m, $\dot{m} = 0.015$ kg/s-m²

Figures 2.9(a) and (b) plot the annual thermal and PV efficiencies as a function of θ_c when truncation is allowed even when not mandated by the height restriction. Table 2.3 lists the values of θ_c and C_e considered along with the corresponding values of θ_d and $\frac{H_e}{H_{max}}$. The dashed curves in Figs. 2.9(a) and (b) show the same case as Fig. 2.8 and represent the maximum C_e and $\frac{H_e}{H_{max}}$, or minimum truncation required to meet the height restriction. The solid curves represent the truncated CPCs for four levels of truncation represented by C_e. For $C_e = 1.2$, the solid curve is terminated at $\theta_c = 40^o$ because for lower values of θ_c, it is not possible to install glazing. As shown in Fig. 2.9(a), higher thermal efficiencies are obtained by truncation for a fixed θ_c. Along lines of constant C_e, η_{th} decreases with increasing θ_c for $\theta_c > 25^o$ as the level of truncation decreases. For $\theta_c = 25^o$, the loss of efficiency due to the narrow acceptance angle overshadows the favorable impact of increased truncation.

In contrast to thermal efficiency, PV efficiency decreases with increasing truncation at fixed θ_c as shown in Fig. 2.9(b). Also in contrast to the trends for η_{th}, η_{PV} increases with increasing θ_c at fixed C_e. In summary, a 9% increase in thermal efficiency can be obtained through truncation for the geometry with $\theta_c = 40^o$ and $C_e = 1.2$, but this increase is obtained at the expense of a 1.2% reduction in the PV efficiency.

Effects of tube diameter

Diameters of 0.02m, 0.025m and 0.03m were considered. Geometries that exceed the height requirement were truncated to $H_e = 0.13$m. As the tube diameter is increased, the size of the CPC (the height and width for a single concentrator) increases for a fixed
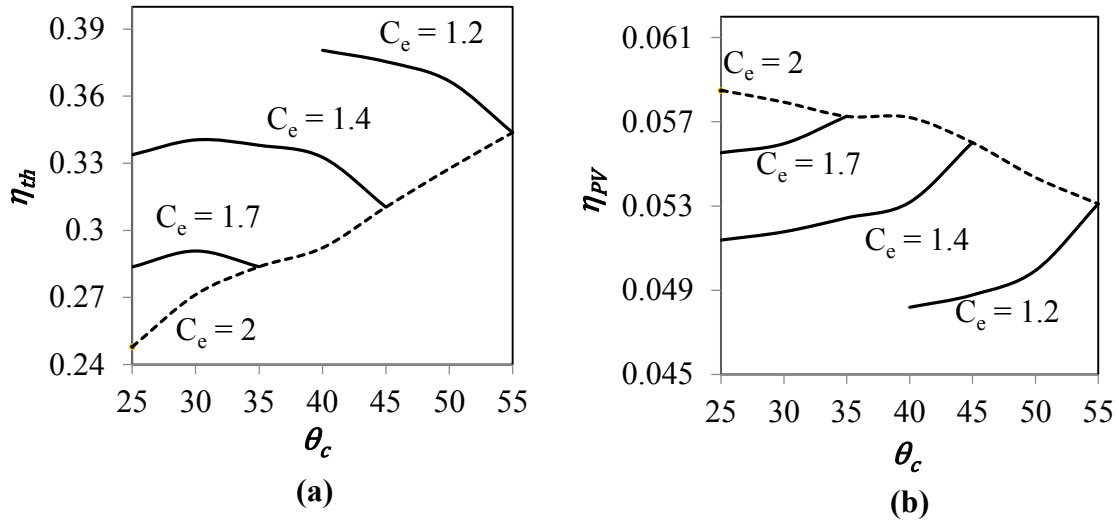
Fig. 2.9 Annual thermal (a) and PV (b) efficiency as a function of θ_c and C_e, $D = 0.03$m, $\dot{m} = 0.015$ kg/s-m^2

Table 2.3 Truncated parameters for different CPC geometries used in Fig. 2.9

θ_c	C_e	θ_d	H_e/H_{max}
25°	1.4	86°	0.16
	1.7	68°	0.25
	2	50°	0.42
30°	1.4	81°	0.24
	1.7	59.6°	0.41
35°	1.4	74.6°	0.35
	1.7	45°	0.75
40°	1.2	87.2°	0.31
	1.4	66.2°	0.52
	1.2	82°	0.42
	1.4	45°	1
50°	1.2	74.6°	0.58
55°	1.2	55°	1

θ_c. Figure 2.10(a) shows that for 25°< θ_c < 55°, η_{th} is relatively insensitive to changes in

the diameter of the absorber tube. The level of truncation is responsible for slight changes

in the slope of the curves. As shown in Fig. 2.10(b), η_{PV} is also insensitive to changes in

the tube diameter for $\theta_c \geq 40°$. For $\theta_c < 40°$, a smaller diameter yields higher

efficiency because less truncation is required.
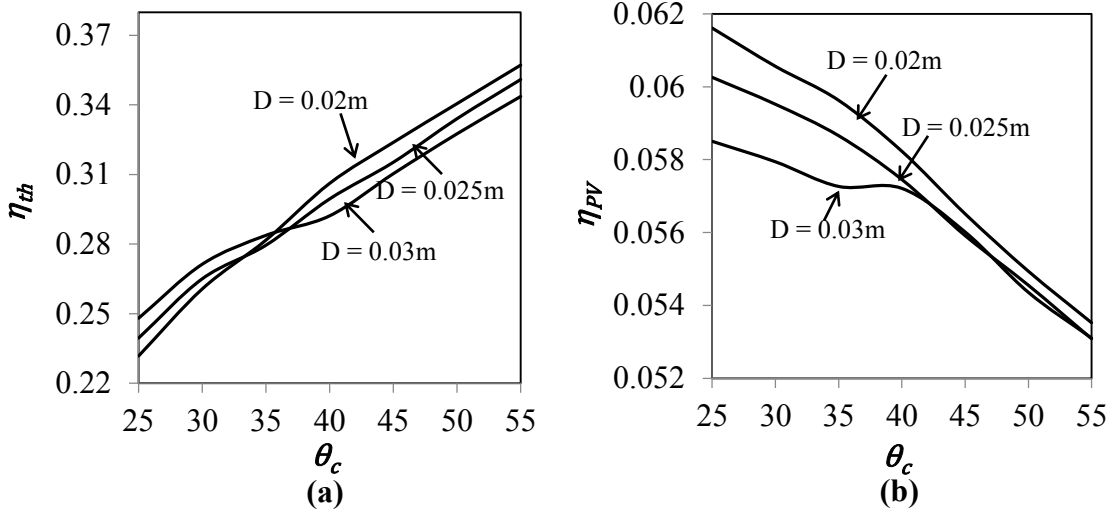
Fig. 2.10 Annual thermal (a) and PV (b) efficiency as a function of θ_c and D, $\dot{m} = 0.015$ kg/s-m^2

4.3 Case Study

The performance of the hybrid PV/T collector is compared to a system with independent solar thermal and PV modules with the same total collector area. Based on the results of the parametric study, a CPC geometry with $D = 0.02$m and C_e as large as possible subject to a maximum CPC height of 0.13m was selected to maximize η_{PV}. θ_c was varied from 25° to 55°.

The independent solar thermal module was assumed to be a glazed flat plate collector with selective absorber coating. The assumed efficiency of the thermal module, based on a representative SRCC OG-100 rating [43], is

$$\eta = 0.779 - 4.28 \frac{T_{fi} - T_b}{G} - 0.00483 \frac{(T_{fi} - T_b)^2}{G} \tag{2.20}$$

The PV module for the independent system is a thin film CdTe module with the same reference efficiency as the PV module in the hybrid system. Figure 2.11 is a sketch of the dimensions of the hybrid PV/T collector and the independent system with separate thermal and PV collectors. Both have a total area of 2m^2. To size the independent

24
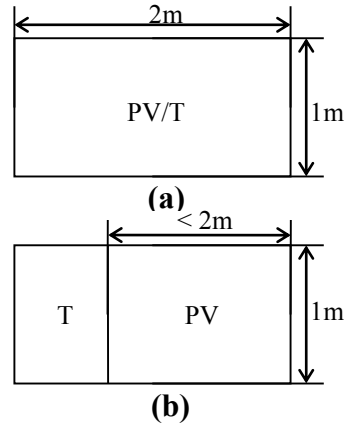
Fig. 2.11 A schematic for (a) the hybrid PV/T system and (b) the independent system of PV and T collectors
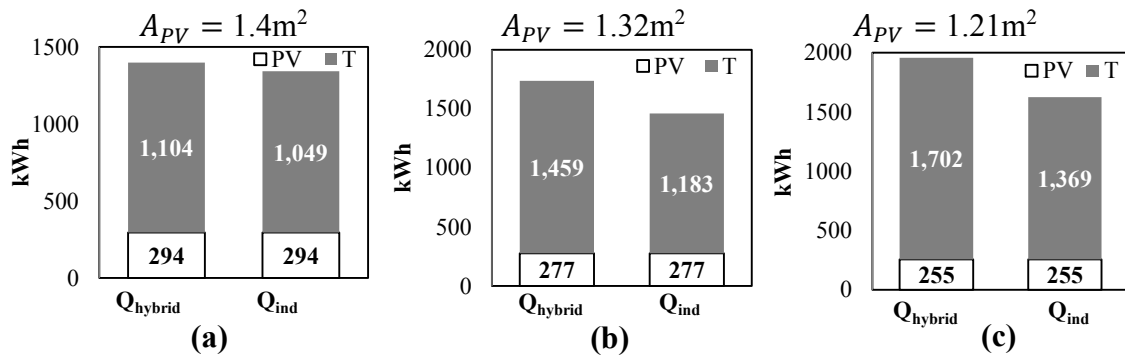
Fig. 2.12 Total annual output (kWh) for the hybrid collector and the independent system at (a) $\theta_c = 25°$, (b) $\theta_c = 40°$ and (c) $\theta_c = 55°$, $D = 0.02$m, $\dot{m} = 0.015$ kg/s-m^2

modules, the PV output was set equal to that of the hybrid PV/T with the remaining area allocated to the thermal collector. The area A_{PV} of the independent PV module is less than 2 m^2 due to the loss of efficiency of the hybrid PV module resulting from shading and transmission losses through the wavelength selective film.

Figure 2.12 compares the annual energy delivered (kWh) by the hybrid module and the corresponding independent system. The incident radiation for Phoenix, AZ over the collector area is 4765 kWh. At $\theta_c = 25°$, the combined output (PV + thermal) is 1343 kWh for the independent collector and 1398 kWh for the hybrid collector. The PV

25

module output in forced to be the same in both collectors and is 294 kWh. The area of the

independent PV module is 1.4 m². At $\theta_c = 40°$, the total output of the hybrid module

increases to 1736 kWh. The increase in thermal output is obtained at the expense of a

decrease in PV output to 277 kWh. Accordingly, the area of the independent PV system

is decreased to 1.32 m². The total output of the independent system increases to 1460

kWh. As θ_c is further increased to 55°, the total output increases to 1955 kWh (a further

increase of 25%) accompanied by a decrease in PV output to 255 kWh. The area of the

independent PV system is 1.21 m². The total output of the independent system is 1624

kWh. The comparison of the hybrid systems is described by the gain ratio.

$$Gain = \frac{Q_{hybrid}}{Q_{ind}} \tag{2.21}$$

The gain for $D = 0.02$m and $\dot{m} = 0.015$ kg/s-m² is plotted in Fig. 2.13 as a function of

θ_c. The gain is 1.04 at $\theta_c = 25°$ and rises to 1.19 at $\theta_c = 40°$. For $25° < \theta_c < 40°$, the

increase in gain is due to the increase in the thermal output for the hybrid system. The PV

output decreases as θ_c is increased, accompanied by a corresponding decrease in the PV

module area in the independent system to achieve the same PV output. As a result, a

larger area is available for the independent thermal module.
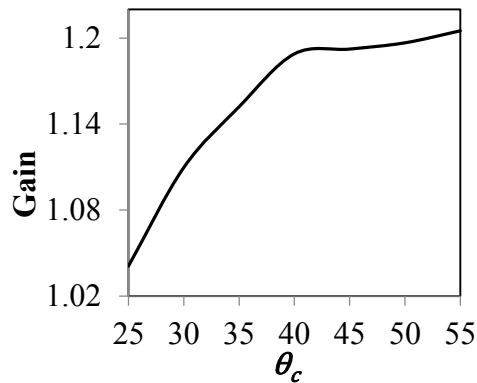
Fig. 2.13 Gain (Eq. 31) as a function of θ_c, for $D = 0.02$m, $\dot{m} = 0.015$ kg/s-m²

2.5 Conclusion

A concept for a non-tracking hybrid photovoltaic/solar thermal collector that uses a wavelength selective film to split incident radiation between a thin-film CdTe PV module and a solar thermal module is analyzed. A Monte Carlo Ray-Trace algorithm to determine optical performance of the CPC/selective film is presented. To illustrate the use of MCRT to assess annual thermal collector performance, annual thermal and electrical simulations are performed for Phoenix, AZ. The parametric trends are similar for different geographical locations.

For this concept, the thermal and electrical performance of the hybrid collector depends strongly on the half-acceptance angle θ_c and the truncation of the CPC. Higher thermal efficiencies can be achieved by increasing θ_c from 25 to 55° or by truncation of the CPC. Truncation enhances the apparent field of view of the CPC and allows a larger fraction of the incident diffuse radiation to reach the absorber tube. The electrical efficiency is most significantly affected by direct shading by the absorber tubes. While the electrical efficiency is not directly dependent on the concentrator geometry, the geometric concentration factor C_e has a direct bearing on the number of absorber tubes shading the PV module; a higher C_e corresponds to less shading. The truncation and half-acceptance angle can be chosen for an application based on established trade-offs, along with a suitable diameter.

For the analyzed system, the hybrid collector provides up to 20% higher total energy conversion efficiency (output) but lower individual electrical and thermal efficiencies compared to independent PV and solar thermal modules. The use of an additional glazing to reduce thermal losses plus the addition of the film reduces

transmission of insolation to the PV. This penalty is not offset by the efficiency gain attributed to matching the spectral content of the radiation incident at the PV cell to the quantum efficiency band of the PV cell. Thus PV efficiency drops from the nominal value of 8.8% to 5.8% for the optimized geometry. Incident radiation on the thermal absorber is restricted to primarily the near infrared and thus thermal output is reduced compared to a conventional thermal collector, yielding an annual thermal efficiency of ~31%.

On the positive side, the concept is unique compared to other proposed PV/T collectors because the thermal component can be envisioned as an add-on to an existing roof-top PV installation. Such a retrofit would increase the amount of usable energy per unit installed collector area.[2]

2.6 Nomenclature

A Area, m^2

C Geometric concentration factor

c_p Specific heat capacity at constant pressure, J/kgK

D Tube diameter, m

$E_{b\lambda}$ Blackbody spectral emissive power

F_R Heat removal rate

F' Collector efficiency factor

f Fourth order polynomial

$f_{0-\lambda T}$	Fraction of blackbody emissive power from 0 to λ nm
f_{rat}	experimentally derived factor that relates $h_{c,a-c}$ and $h_{c,a-m}$ [36]
G	Incident solar radiation, W/m^2
g	Fraction of incident solar radiation
Gain	Ratio of total outputs of the hybrid and independent systems
Gr	Grashoff number
H	Height, m
h	Heat transfer coefficient, W/m^2K
k	Thermal conductivity, W/mK
L	Length of CPC reflector, m
$\dot{m}$	Mass flow rate, kg/s-m^2
N	Number of rays
Nu	Nusselt number
n	number of concentrators in the collector
Pr	Prandtl number
Q	Energy, kWh
Q_u	Useful energy, W/m^2 ($3600J/m^2$ for hourly data)
R	Random number, uniformly distributed in (0,1)
Ra	Rayleigh number
$\vec{r}$	Direction of incident radiation
R_{th}	Equivalent resistance of the thermal network, m^2K/W
Re	Reynolds number
S	Energy absorbed per unit absorber area, W/m^2 ($3600J/m^2$ for hourly data)

T	Temperature, K
t	Thickness of the CPC/selective film, m
U_L	Overall loss coefficient, W/m²K
v_w	Wind velocity, m/s
W_λ	Spectral weighting factor
x, y, z	Cartesian coordinates

Greek symbols

α	Absorptance of the absorber tube
β	PV cell temperature coefficient, °C⁻¹
γ	PV cell irradiance coefficient
ε	Emittance
η	Efficiency
θ	Angle, deg
θ_c	Nominal half-acceptance angle, deg
θ_d	Truncated half-acceptance angle, deg
λ	Wavelength
ρ	Reflectance
σ	Stefan-Boltzmann constant, J/s-m²K; standard deviation
τ	Transmittance

Subscripts

a	Absorber tube, absorbed rays
air	Air
b	Beam radiation

back	Back surface of the PV cell
c	CPC cover; collector; convection
cd	Conduction
cell	PV cell
d	Diffuse radiation
D	Associated with tube outer diameter
e	Effective value
fi / fo	Fluid inlet/outlet
fi	Between fluid and tube
hybrid	Hybrid collector
ind	Independent collector
i	Index, inner
m	Wavelength selective film
max	Maximum value at a fixed θ_c
min	Minimum value
o	Outer
PV	PV module
q	Quantum
$\vec{r}$	Directional
ref	Reference value
s	Specular reflection
sky	Sky
t	Transmitted rays

th	Thermal module
xy, yz	xy, yz planes
∞	Ambient
λ	Spectral

Superscripts

PV	PV module
T	Thermal module

2.7 References

[1] Tripanagnostopoulos, Y., Nousia, T, Souliotis, M., and Yianoulis, P., 2002, "Hybrid Photovoltaic/Thermal Solar Systems," Solar Energy, 72(3), pp. 217-234.

[2] Tyagi, V. V., Kaushik, S. C., and Tyagi, S. K., 2012, "Advancement in Solar Photovoltaic/Thermal (PV/T) Hybrid Collector Technology," Renewable and Sustainable Energy Reviews, 16(3), pp. 1383-1398.

[3] Chow, T. T., 2010, "A Review on Photovoltaic/Thermal Hybrid Solar Technology," Applied Energy, 87(2), pp. 365-379.

[4] Anderson, T. N., Duke, M., Morrison, G. L., and Carson, J. K., 2009, "Performance of a Building Integrated Photovoltaic/Thermal (BIPVT) Solar Collector," Solar Energy, 83(4), pp. 445-455.

[5] Davidsson, H., Perers, B., and Karlsson, B., 2012, "System Analysis of a Multifunctional PV/T Hybrid Solar Window," Solar Energy, 86(3), pp. 903-910.

[6] Coventry, J. S., 2005, "Performance of a Concentrating Photovoltaic /Thermal Solar Collector," Solar Energy, 78(2), pp. 211-222.

[7] Li, M., Li, G. L., Ji, X., 2011, "The Performance Analysis of the Trough Concentrating Solar Photovoltaic/Thermal System," Energy Conversion and Management, 52(6) pp. 2378-2383

[8] Zhu, L., Boehm, R. F., Wang, Y., 2011, "Water Immersion Cooling of PV Cells in a High Concentration System," Solar Energy Materials and Solar Cells, 95(2) pp. 538-545.

[9] Zondag, H. A., de Vries, D. W., van Helden, W. G. J., van Zolingen, R. J. C., and van Steenhoven, A. A., 2003, "The Yield of Different Combined PV-Thermal Collector Designs," Solar Energy, 74(3), pp. 253-269.

[10] Fraisse, G., Ménézo, C., and Johannes, K., 2007, "Energy Performance of Water Hybrid PV/T Collectors Applied to Combisystems of Direct Solar Floor Type," Solar Energy, 81(11), pp. 1426-1438.

[11] Kim, J., and Kim, J., 2012, "The Experimental Performance of an Unglazed PV-ThermalCollector with a Fully Wetted Absorber," Energy Procedia, 30(0) pp. 144-151.

[12] Chow, T. T., Pei, G., Fong, K. F., 2009, "Energy and Exergy Analysis of

Photovoltaic–Thermal Collector with and without Glass Cover," Applied Energy, 86(3) pp. 310-316.

[13] Dupeyrat, P., Ménézo, C., Wirth, H., 2011, "Improvement of PV Module Optical Properties for PV Thermal Hybrid Collector Application," Solar Energy Materials and Solar Cells, 95(8) pp. 2028-2036.

[14] Amori, K. E., and Taqi Al-Najjar, H. M., 2012, "Analysis of Thermal and Electrical Performance of a Hybrid (PV/T) Air Based Solar Collector for Iraq," Applied Energy, 98(0) pp. 384-395.

[15] Tonui, J. K., and Tripanagnostopoulos, Y., 2007, "Improved PV/T Solar Collectors with Heat Extraction by Forced or Natural Air Circulation," Renewable Energy, 32(4), pp. 623-637.

[16] Hegazy, A. A., 2000, "Comparative Study of the Performances of Four Photovoltaic/Thermal Solar Air Collectors," Energy Conversion and Management, 41(8), pp. 861-881.

[17] Hj. Othman, M. Y., Yatim, B., Sopian, K., and Abu Bakar, M. N., 2005, "Performance Analysis of a Double-pass Photovoltaic/Thermal (PV/T) Solar Collector with CPC and Fins," Renewable Energy, 30(13), pp. 2005-2017.

[18] Assoa, Y. B., Menezo, C., Fraisse, G., 2007, "Study of a New Concept of Photovoltaic–Thermal Hybrid Collector," Solar Energy, 81(9) pp. 1132-1143.

[19] Imenes, A. G., and Mills, D. R., 2004, "Spectral Beam Splitting Technology for Increased Conversion Efficiency in Solar Concentrating Systems: a Review," Solar Energy Materials and Solar Cells, 84(1–4), pp. 19-69.

[20] Imenes, A. G., Buie, D., and McKenzie, D., 2006, "The Design of Broadband, Wide-Angle Interference Filters for Solar Concentrating Systems," Solar Energy Materials and Solar Cells, 90(11), pp. 1579-1606.

[21] Segal, A., Epstein, M., and Yogev, A., 2004, "Hybrid Concentrated Photovoltaic and Thermal Power Conversion at Different Spectral Bands," Solar Energy, 76(5), pp. 591-601.

[22] Jiang, S., Hu, P., Mo, S., and Chen, Z., 2010, "Optical Modeling for a Two-Stage Parabolic Trough Concentrating Photovoltaic /Thermal System using Spectral Beam Splitting Technology," Solar Energy Materials and Solar Cells, 94(10), pp. 1686-1696.

[23] Izumi, H., 2000, "Hybrid Solar Collector for Generating Electricity and Heat by Separating Solar Rays into Long Wavelength and Short Wavelength," U.S. 6057504.

[24] Rabl, A., 1976, "Optical and Thermal Properties of Compound Parabolic Concentrators," Solar Energy, 18(6), pp. 497-511.

[25] Carvalho, M. J., Collares-Pereira, M., Gordon, J. M., and Rabl, A., 1985, "Truncation of CPC Solar Collectors and Its Effect on Energy Collection," Solar Energy, 35(5), pp. 393-399.

[26] Weber, M. F., Stover, C. A., Gilbert, L. R., 2000, "Giant Birefringent Optics in Multilayer Polymer Mirrors," Science, 287(5462) pp. 2451-2456.

[27] Nann, S., and Emery, K., 1992, "Spectral Effects on PV-Device Rating," Solar Energy Materials and Solar Cells, 27(3), pp. 189-216.

[28] Koishiyev, G. T., 2010, "Analysis of Impact of Non-Uniformities on Thin-Film Solar Cells and Modules with 2-D Simulations,"Ph.D Thesis, Colorado State University.

[29] Howell, J. R., 1998, "The Monte Carlo Method in Radiative Heat Transfer," Journal

of Heat Transfer, 120(3), pp. 547-560.

[30] Modest, M. F., 2003, Radiative Heat Transfer, Second Edition, Academic Press, pp. 653

[31] Rabl, A., 1976, "Solar Concentrators with Maximal Concentration for Cylindrical Absorbers," Appl. Opt., 15(7), pp. 1871-1873.

[32] Duffie, J. A., Beckman, W. A., 2006, Solar Engineering of Thermal Processes, Third edition, John Wiley and Sons, New York, NY.

[33] Krueger, K. R., Davidson, J. H., and Lipiński, W., 2011, "Design of a New 45 kWe High-Flux Solar Simulator for High-Temperature Solar Thermal and Thermochemical Research," Journal of Solar Energy Engineering, Transactions of the ASME, 133(1).

[34] Renewable Resource Data Center, National Renewable Energy Laboratory, 2012, http://rredc.nrel.gov/solar/old_data/nsrdb/1961-1990/tmy2/

[35] Kuehn, T. H., Goldstein, R. J., 1976, "Correlating Equation for Natural Heat Transfer between Horizontal Circular Cylinders," Int. J. Heat Mass Transfer, Vol. 19, pp. 1127-1134

[36] Prapas, D. E., Norton, B., and Probert, S. D., 1987, "Thermal Design of Compound Parabolic Concentrating Solar-Energy Collectors," Journal of Solar Energy Engineering,109(2), pp.161-168.

[37] Churchill, S. W., and Chu, H. H. S., 1975, "Correlating Equations for Laminar and Turbulent Free Convection from a Vertical Plate," International Journal of Heat and Mass Transfer, 18(11) pp. 1323-1329.

[38] Gnielinski, V., 1976, "New Equations for Heat and Mass Transfer in Turbulent Pipe and Channel Flow," Int. Chem. Engng., vol. 16, pp. 359-368.

[39] Mattei, M., Notton, G., Cristofari, C., Muselli, M., and Poggi, P., 2006, "Calculation of the Polycrystalline PV Module Temperature Using a Simple Method of Energy Balance," Renewable Energy, 31(4), pp. 553-567.

[40] Vigil-Galán, O., Arias-Carbajal, A., Mendoza-Pérez, R., Santana, G., Sastré-Hernández, J., Contreras-Puente, G., Morales-Acevedo, A., and Tufiño-Velázquez, M., 2006, "Spectral Response of CdS/CdTe Solar Cells Obtained with Different S/Cd Ratios for the CdS Chemical Bath," Solar Energy Materials and Solar Cells, 90(15), pp. 2221-2227.

[41] AlBusairi, H. A., Muller, H. A., "Performance Evaluation of CdTe PV Modules under Natural Outdoor Conditions in Kuwait," Proc. 25th European Solar Energy Conference and Exhibition/5th World Conference on Photovoltaic Energy Conversion, pp. 3468-3470.

[42] King, D. L., Boyson, W. E., and Kratochvill, J. A., Sandia National Laboratories, 2004, "Photovoltaic Array Performance Model."

[43] Solar Rating and Certification Corporation, "https:// secure.solar-rating.org/.", accessed March 1, 2011.

Chapter 3

Analysis of a Hybrid Solar Window for Building Integration[2]

The technical performance of a hybrid 'solar window' that provides heating in addition to daylighting is evaluated. A wavelength selective film is coupled with a compound parabolic concentrator (CPC) to reflect and concentrate the infrared portion of the solar spectrum onto a tubular absorber while transmitting the visible portion of the spectrum into the interior space. The optical performance of the CPC/selective film is predicted using a Monte Carlo Ray-Tracing model. An adaptive concentrator geometry based on asymmetrical truncation of CPCs is analyzed for vertical windows and horizontal skylights. The predicted visible transmittance is 0.66 to 0.73 for single glazed windows and 0.61 to 0.67 for double glazed windows. The solar heat gain coefficient and the U-factor are comparable to existing glazing technology. The annual thermal efficiency for double glazed windows/skylights based on use in Minneapolis, MN is 24-26%.

Keywords: hybrid, solar window, wavelength selective film, building integration

3.1 Introduction

Daylighting is widely recognized as a key strategy towards an aesthetically pleasing and energy efficient built environment. Several studies link human health and productivity to natural light (Kim G. and Kim J., 2010; Plympton et al., 2000;Vandewalle

---

[2]This paper was co-authored by Tim Hebrink and Jane H. Davidson

et al., 2006). Daylight produces a true color rendering, provides visual comfort, and is considered to be a major cue to the human circadian rhythm (Gochenour and Anderson, 2009). With appropriate lighting control systems, daylighting can reduce electrical energy consumption by more than 30% (Chow S. et al., 2013; Li et al., 2006). As highly glazed commercial buildings are synonymous with modern architectural design, the development of energy efficient commercial glazing technologies is important.

Modern glazing technologies offer various approaches to regulate their thermal and optical performance. Multi-layer glazing separated by air, vacuum, inert gas or transparent insulators such as silica aerogel (Buratti and Moretti, 2012) reduce thermal losses. Tinted or reflective glazing technologies (Chow T. et al., 2010; Mohelnikova, 2009; Alvarez et al., 2013), low emissivity coatings (Alvarez et al., 2013; Martin-Palma, 2009) and spectrally selective glazing (Alvarez et al., 2013; Martin-Palma, 2009; Xu et al., 2006) regulate the spectral response of the window. Switchable glazing technologies such as electrochromic (Page et al., 2007; Piccolo et al., 2009; Granqvist et al., 2010), thermochromic (Granqvist et al., 2010; Mlyuka et al., 2009) or photochromic glazing and liquid crystals (Gardiner et al., 2009) have been developed as part of 'smart' fenestration systems to provide varying levels of daylighting and passive thermal control for the interior.

An attractive approach for glazing systems is to harness the sunlight not utilized for daylighting to generate alternate forms of energy to supplement the overall sustainability of the built structure. Semi-transparent building integrated photovoltaic (BIPV) glazing (Chow T. et al., 2010; Li et al., 2009) can be used to offset interior lighting loads, but suffer from low transmittance in the visible. Chow T. et al. (2010,

2011) analyzed water-flow double-pane window. Water is circulated through the cavity of a double glazed window to reduce solar heat gains by 32% as compared to a double glazed window with absorptive and clear glass, in addition to annual heat extraction by water that was equal to the annual solar heat gain through the double glazed window. Davidsson et al. (2010) proposed and tested a multifunctional, window integrated PV/T with tiltable aluminum reflectors to concentrate incident solar energy. The electrical and thermal performance of the window was comparable to roof-integrated PV and solar thermal collectors of the same area. A drawback of the design is that in the active mode, the window acts more like a wall due to the opaque concentrators.

In the present work, a hybrid 'solar window' based on the principle of spectral band splitting is proposed and analyzed. The proposed device performs multiple functions: it daylights the interior space; it generates useful thermal energy which can be used to offset domestic hot water or spaceheating loads; and it can be used to regulate heat gains through the window. Figure 3.1 shows the design concept. A wavelength selective film is attached to a series of compound parabolic concentrators (CPCs) made of transparent PMMA or polycarbonate, and integrated into a window on the interior side of a low-iron glazing. The wavelength selective film divides the incident solar spectrum into visible (transmitted) and near-infrared (reflected) bands. The low iron glazing ensures high transmittance (~91%) over the entire visible and near infrared regions of the spectrum. The spectrally selective CPCs are connected to tubular absorbers via end plates that can pivot about rubber bushings. A heat transfer fluid such as water or a water/antifreeze mixture is circulated through the absorber tubes. The inlet/outlet

37

manifolds to supply fluid to the absorbers are incorporated into the window frame for aesthetic architectural integration.

The window may be operated in two modes by adjusting the position of the CPCs. In the concentrating mode, the CPCs are 'closed'. The CPC/selective film transmits the visible portion of the incident solar spectrum to the interior space for daylighting. Because the film transmits visible radiation, it does not suffer the drawback of the concentrated PV/T concept proposed by Davidsson et al. (2010). The infrared portion of the spectrum is concentrated on to the absorber tubes to generate useful thermal energy. Blocking the infrared portion of the solar spectrum serves to passively cool the interior space. In an alternative non-concentrating mode, the concentrators can be opened to allow the full solar spectrum to be transmitted into the interior space. In this case, the solar window acts as a passive space heating device.

In this paper, we model the solar window with the objective of identifying the effects of CPC geometry on the thermal and daylighting technical performance. A Monte-Carlo Ray Tracing (MCRT) algorithm is formulated to model the optical behavior of the wavelength selective film (Ulavi et al., 2013). The MCRT model determines the spectral and energetic split between the solar thermal module and the daylit space as a function of the wavelength and direction of incident radiation. These results are used to predict the annual thermal efficiency of the system, and the daylighting and heat insulating properties of the window. A case study for east and south facing vertical windows and a horizontal skylight is presented for Minneapolis, MN.

3.2 Wavelength Selective Film

The wavelength selective film is a co-extruded multilayer dielectric reflector consisting of alternating layers of high refractive index polymers and low refractive index polymers each with thicknesses equal to one-fourth of the wavelength to be reflected (Weber et al., 2000). Each polymer layer constructively interferes with the next layer to create a broad reflection band in the near infrared and a high transmission band in the visible wavelengths.

Figure 3.2 plots the reflectance (ρ_m) of the film for normal and 60° off-normal incidence angles (θ_m) as a function of wavelength (λ). The data are constructed assuming sunlight consists of 50% p-polarized and 50% s-polarized light. The data for $\lambda \leq$ 1110nm are for a commercially available film. Data beyond 1100nm represent properties expected for a film under development. At normal incidence, the film has a low reflectance (measured at ~8-12%) from 400 to 850nm and a high reflectance in the infrared from 850 to 1835nm (~95%). At 60° off-normal incidence, the reflection band edges shift to shorter wavelengths but the average reflectance remains the same for the p-polarized component of light. Reflectivity for p-polarized light is independent of the incidence angle θ_m for birefringent polymers with matched refractive indices along the film thickness (Weber et al., 2000). The reflectance for the s-polarized component of light is about 2-3% higher for θ_m = 60° than at normal incidence; this slight increase is not included in Fig. 3.2.

The quality of the transmitted daylight depends on the relative sensitivity of the human eye to different wavelengths, indicated by the photopic luminosity function $V(\lambda)$ [1] shown in Fig. 3.3. The plot shows that the human eye is sensitive to light in a narrow band from 460< λ < 680nm, with a peak at 550nm. Daylighting metrics such

39

illuminance and visible transmittance are weighted by the photopic luminosity function. As shown in Fig. 3.2, the film has a high transmittance (~0.9) for $450 \leq \lambda \leq 700$nm for $\theta_m = 0°$ and $\theta_m = 60°$. Because the film is well matched to the photopic luminosity function, it is ideal for daylighting.

3.3 Design approach

In this section, a design approach that can be used to select an appropriate CPC geometry for any facade orientation and geographical location is described. To examine the versatility of the proposed design, three cases are evaluated – vertical windows on east and south facing facades and a horizontal skylight in Minneapolis, MN. For this analysis, the window and skylight size is fixed at 1 x 1.5m (Fig. 3.4(a)). Two adjacent windows of this size represent a window-to-wall ratio (WWR) of 35% for a typical single person office space having dimensions 3 x 3 x 2.75m. The concentrators are oriented such that they have a flow length of 1m, and the concentrator depth H is restricted to 0.05m based on typical vane sizes for window blinds (Fig. 3.4(b)). The tube diameter is 0.016m. Single glazed (3.2mm glass) and double glazed (3.2mm glass, 12.7mm air, 3.2mm glass) are considered to represent conventional window glazing options. The concentrators are 1.5mm thick acrylic.

The CPC geometry, shown in Fig. 3.5, is defined by the tube diameter D, the nominal half-acceptance angle θ_c and the nominal geometrical concentration factor C (the ratio of the CPC aperture area to the absorber area) (Rabl, 1976).

$$C = \frac{1}{\sin \theta_c} \tag{3.1}$$

For a specular, opaque concentrator surface, the geometry concentrates all radiation within the acceptance angle, a useful attribute for low-concentration, non-tracking solar applications such as windows. For the window/skylight application, an asymmetrically truncated CPC has several advantages. The CPC can be aligned in a direction so that it receives maximum annual radiation within the nominal acceptance angle for a particular geographical location. The truncated CPC provides higher concentration and efficiency for the solar thermal module. Truncation also provides a more compact, visually appealing design that can be adapted to the façade orientation. The line indicated by the letter 'T' in Fig. 3.5(a) represents the plane of asymmetric truncation. The corresponding truncated geometry (Fig. 3.5(b)) has an effective geometric concentration factor $C_e > C$, and an enhanced field of view, represented by the truncated half-acceptance angles θ_{d1} and θ_{d2} ($> \theta_c$).

Figure 3.6 depicts the use of asymmetrically truncated CPCs for a vertical window and a horizontal skylight. It is possible to use the solar window as a skylight in the full range of orientations. Figures 3.6(a) and (b) show two concentrator designs for a vertical window collector having nominal half-acceptance angles of 40º and 25º respectively. The smaller concentrator ($H = 0.04$m, $W = 0.09$m) in Fig. 3.6(a) has a higher optical efficiency than that shown in Fig. 3.6(b) at the absorber tube due to a wider half-acceptance angle. However, a window consisting of the concentrators in Fig. 3.6(b) would have fewer absorber tubes and as a result, transmit more light into the daylit space. In Figs. 3.6(a) and (b), the CPC axis is oriented in a direction such that maximum radiation transmitted through the window is incident on the concentrator within the

41

respective acceptance angles. For Minneapolis, this orientation is 50° and 45° from the vertical for $\theta_c = 40°$ and 25°, respectively.

Figure 3.6(c) shows a CPC design for a horizontal skylight. The CPC axis is inclined at 35° with the vertical towards the south to maximize incident radiation within the acceptance angle. For an arbitrary façade orientation, a similar approach can be used to choose a suitable plane of truncation. In the present study, a range of concentrator designs for 25°≤ θ_c ≤45° were evaluated.

3.4. Model

A 3-D Monte Carlo ray-tracing (MCRT) model was implemented to predict the reflectance of the CPC/wavelength selective film, and the resultant optical efficiency of the solar thermal module as a function of the direction and wavelength of incident radiation. The model yields incidence angle modifiers for the solar thermal module. Results are also used to determine the visible transmittance (τ_{vis}), solar heat gain coefficient ($SHGC$) and U-factor for the hybrid solar window. The latter results are independent of geographical location and can be used as parameters in commercial software such as RADIANCE [2], IES VE Pro [3] to perform daylighting simulations.

3.4.1 MCRT

The MCRT model for the CPC is described in detail by the authors in Ulavi et al. (2013). For the present application, the procedure was modified for asymmetrically truncated geometries to determine the following quantities.

- $\left(g_{b,\vec{r}}^T \equiv \frac{G_{b,\vec{r}}^T}{G_{b,\vec{r}}} \right)$, $\left(g_d^T \equiv \frac{G_d^T}{G_d} \right)$ – The fractions of incident beam radiation (as a function of incident direction $\vec{r}$) and diffuse radiation reflected to the absorber tube

- $\left(g_{b,\vec{r}}^{DL} \equiv \frac{G_{b,\vec{r}}^{DL}}{G_{b,\vec{r}}} \right)$, $\left(g_d^{DL} \equiv \frac{G_d^{DL}}{G_d} \right)$ – The fractions of incident beam radiation (as a function of incident direction $\vec{r}$) and diffuse radiation transmitted to the daylit space

- $\{ \lambda_{t,\vec{r}} \mid 1 < t < N_{b,\vec{r}}^{DL} \}, \{ \lambda_{t,d} \mid 1 < t < N_d^{DL} \}$ – The spectral distribution of radiation transmitted to the daylit space

The MCRT procedure launches a stochastically large number of rays, N_i, from the bottom plane of the glazing to predict the optical behavior of the system based on the interactions of each ray with the optical and geometrical elements of the CPC cavity system. The concentrator geometry, the wavelength selective film, the low iron glass cover and the selective absorber form the elements of the CPC cavity system. Figure 3.7 shows the ray-tracing procedure for a representative ray. Each ray has a fraction of the incident irradiance $q = {}^G/_{N_i}$, a wavelength λ_i and direction $\vec{r}(\theta_{xy}, \theta_{yz})$. The spectral distribution of the rays represents a blackbody distribution at 5777K. Each ray is tracked independently in the xy and yz planes and the path is superimposed to obtain the intersection point with the CPC, cover or absorber tube. The ray tracing algorithm is terminated when: (i) the ray is intercepted at the absorber tube, (ii) is transmitted through the wavelength selective film to the daylit space, or (iii) exits the system by transmission through the cover or the ends of the CPC.

The interaction (reflection or transmission) with the cover and the wavelength selective film is approached statistically by comparing a generated random number R_ρ with the predicted reflectance at the point of intersection. The reflectance at the cover is predicted using a combination of Snell's law and Bouguer's law (Duffie and Beckman, 2006). The refractive index and extinction coefficient for low iron glass are 1.526 and $4m^{-1}$ respectively. The film reflectance is a function of the wavelength λ_i and incident angle θ_m (resultant of incident angles in the xy and yz planes) at the film, further details for which can be found in previous work (Ulavi et al, 2013). A specular reflectance $\rho_s = 0.95$ is assumed for the film. A specular error θ_s having a normal distribution with a standard deviation $\sigma_s = 3$ mrad, accounts for the irregularities in the CPC surface.

Multiple MCRT simulations were performed for each concentrator geometry by varying θ_{xy} from -60° to 60° and θ_{yz} from 0° to 60° (due to symmetry in the yz plane about the CPC axis) for the incoming beam radiation in increments of 1° and 5° respectively. The number of rays required for convergence of the numerical solution are $N_{i.b} = 10^5$ and $N_{i.d} = 10^6$ for beam and diffuse radiation, respectively. A separate simulation was performed for incident diffuse radiation requiring $N_{i.d} = 10^6$ rays. θ_{xy} and θ_{yz} for diffuse radiation were chosen based on MCRT distributions for the zenith and azimuth angles for diffuse emission from an isotropic, isothermal surface (Howell, 1998). The fractions of incident beam radiation and diffuse radiation reflected to the absorber tube and transmitted to the daylit space are given by Eqs. (3.2)-(3.5). The number of rays required for convergence of the MCRT solution to a steady value within 1% are $N_{i.b} = 10^5$ for beam radiation and $N_{i.d} = 10^6$ for diffuse radiation. The model was also used to track the transmitted spectrum into the daylit space for daylighting calculations.

$$g_{b,\vec{r}}^{T} = \frac{N_{b,\vec{r}}^{T}}{N_{i,b}} \ , \ g_{d}^{T} = \frac{N_{d}^{T}}{N_{i,d}} \qquad\qquad (3.2), (3.3)$$

$$g_{b,\vec{r}}^{DL} = \frac{N_{b,\vec{r}}^{DL}}{N_{i,b}} \ , \ g_{d}^{DL} = \frac{N_{d}^{DL}}{N_{i,d}} \qquad\qquad (3.4), (3.5)$$

3.4.2 Annual thermal efficiency

The thermal efficiency of the solar thermal module was determined from a quasi-steady state 1-D energy balance. The heat flux at the absorber tube is assumed uniform over the circumference. Flow through the absorber tube is assumed to be uniform and fully developed. Conduction losses across the low iron glass [4] cover are neglected as they are insignificant compared to convective and radiative losses. Table 3.1 lists the assumptions and system properties for the solar thermal model.

The solar radiation absorbed by the absorber tube, S, given in Eq. (3.6) is obtained by interpolating $g_{b,\vec{r}}^{T}$ and g_{d}^{T} obtained by the MCRT model for the direction of incident beam radiation, and magnitudes of the incident beam and diffuse radiation from hourly TMY2 data.

$$S = \left(g_{b,\vec{r}}^{T}G_{b,\vec{r}} + g_{d}^{T}G_{d}\right)\tau_{c}\alpha_{a} \qquad\qquad (3.6)$$

In this expression, τ_{c} represents the transmittance of the cover obtained from Snell's law and Bouger's law, and is a function of incidence angle. The absorptance of the selectively coated (black chrome on nickel) absorber, α_{a}, is weighted for the reflected spectrum. The annual thermal efficiency of the collector is determined by

$$\eta_{th} = \frac{1}{A_{c}}\Sigma_{hours}\frac{nA_{a}F_{R}[S- U_{L}(T_{fi}-T_{\infty})]}{G} \qquad\qquad (3.7)$$

where n represents the number of absorber tubes, and T_{fi} and T_{∞} are the fluid inlet temperature and the hourly ambient temperature, respectively. The overall thermal loss

coefficient U_L is calculated from a thermal resistive network that accounts for the convective, radiative and conductive losses from the absorber tube to the cover and the selective film and subsequent losses to the ambient. The thermal resistive network is provided in Ulavi et al. (2013), with minor modifications listed here. The daylit space is assumed to at a fixed temperature $T_{in} = 25^\circ C$ and the convective losses from the CPC to the room are calculated using heat transfer correlations for natural convection from a horizontal cylinder (Kakaç et al., 1987). For the double glazed window/skylight, an additional resistance $\frac{1}{U_{c-c_2}}$ accounts for convective and radiative heat transfer in the air gap. The natural convection in the vertical/horizontal air cavity (Wright, 1996) is modeled as per ISO 15099, a standard for windows set by the National Fenestration Rating Council (NFRC). Radiation in the cavity enclosed by the glazing layers is modeled assuming a view factor of 1 (for a thin cavity compared to glazing dimensions). The heat removal rate F_R is a function of U_L, the absorber tube thickness and the heat transfer coefficient from the inner absorber wall to the fluid h_{fi} (Ulavi et al., 2013).

3.4.3 Evaluation of fenestration

The visible transmittance (τ_{vis}), the solar heat gain coefficient ($SHGC$) and the U-factor characterize the daylighting and thermal performance of the fenestration. These characteristics are evaluated according to standard rating procedures prescribed by the National Fenestration Rating Council (NFRC).

The center-of-glazing (excluding the window frame) visible transmittance and the solar heat gain coefficient are determined in accordance with NFRC 200-2010 using the reference conditions listed in Table 3.2. The visible transmittance is calculated by

weighting the transmitted spectrum for direct normal radiation ($\vec{r} = \hat{n}$) obtained from the MCRT model by the photopic luminosity function in Fig. 3.3, and accounting for transmission through the cover. In addition, a visible transmittance value for diffuse radiation, $\tau_{vis,d}$, is calculated to simulate uniform overcast sky conditions, a common assumption in daylighting studies (Rosa et al., 2010; Du and Sharples, 2011).

$$\tau_{vis} = \frac{\sum_{t=1}^{N_{b,\hat{n}}^{DL}} V(\lambda_{t,b,\hat{n}})}{\sum_{i=1}^{N_{i,b}} V(\lambda_{i,b})} \tau_{c,\hat{n}} \tag{3.8}$$

$$\tau_{vis,d} = \frac{\sum_{t=1}^{N_d^{DL}} V(\lambda_{t,d})}{\sum_{i=1}^{N_{i,d}} V(\lambda_{i,d})} \tau_{c,d} \tag{3.9}$$

The transmittance through the cover for diffuse radiation is assumed equal to the cover transmittance for beam radiation at an incidence angle of 60° (Duffie and Beckman, 2006).

The solar heat gain coefficient is the fraction of the incident solar energy directly transmitted through the fenestration plus the energy reradiated or convected into the interior space. The CPC/selective film temperature T_m and the overall heat transfer coefficient from the film to the interior, U_{m-in}, are calculated using the thermal model discussed in Ulavi et al. (2013) for the standard NFRC 200-2010 conditions.

$$SHGC = g_{b,\hat{n}}^{DL} + U_{m-in}(T_m - T_{in}) \tag{3.10}$$

$$U_{m-in} = h_{c,m-in} + h_{r,m-in} \tag{3.11}$$

The NFRC 100-2010 procedure is applied to calculate the U-factor for the environmental conditions listed in Table 3.2. The absorber is assumed to be in thermal equilibrium with the air in the CPC cavity. The overall heat transfer coefficient from the selective film to the glazing, U_{m-c}, consists of the convective heat transfer coefficient

based on Nusselt number correlations for natural convection in a vertical cavity as per the approach in ISO 15099, and the conductive and radiative heat transfer coefficients presented in Ulavi et al. (2013).

$$\text{U-factor} = \frac{1}{\frac{1}{U_{c-b}} + \frac{1}{U_{m-c}} + \frac{1}{U_{in-m}}} \tag{3.12}$$

3.5 Results

3.5.1 MCRT

Results obtained from the MCRT model are specific to a CPC geometry, but are independent of geographical location. The annual thermal and daylighting performance of the hybrid solar window for any building integrated application can be analyzed using the MCRT results for the CPC geometry as an input to the respective thermal and daylighting models. To illustrate the type of data obtained from the MCRT model, Fig. 3.8 shows results for one vertical window geometry: $\theta_c = 30°$, $D = 0.016$m, $\theta_{d1} = -86.35°$, $\theta_{d2} = 32.25°$.

Figure 3.8(a) shows the fraction of incident radiation concentrated on the absorber tube, $g_{b,\vec{r}}^{T}$, as a function of direction of the incident radiation, $\vec{r}$, expressed through components θ_{xy} and θ_{yz} as defined in Section 4.1. θ_{xy} is varied from -45° to 45° about the CPC axis in the xy plane to account for expected incidence angles on the vertical façade in the plane of the CPC. θ_{yz} is varied from 0° to 60° about the CPC axis in the yz plane to characterize losses through the ends of the CPC. The corresponding value for incident diffuse radiation, g_d^{T}, is inset. The information in this figure can be used to determine the optical performance of the solar thermal module depending on the local solar angles. Consider the results at $\theta_{yz} = 0°$ (no end losses). Within the nominal half acceptance

angle ($-30^\circ \leq \theta_c \leq 30^\circ$), the CPC geometry is a perfect concentrator for reflected radiation. In this range, $g^T_{b,\vec{r}}$ is ~0.52-0.62 (i.e. 52-62% of the incident radiation reaches the absorber tube). Outside this angular range, the geometry ceases to be a perfect concentrator. For $-45^\circ < \theta_{xy} < -30^\circ$, the incident radiation is outside the nominal half-acceptance angle but is within the truncated half-acceptance angle θ_{d1}; $g^T_{b,\vec{r}}$ ~0.19-0.2..

Beyond the truncated half-acceptance angle $\theta_{d2} = 32.25^\circ$, $g^T_{b,\vec{r}}$ drops to zero. As θ_{yz} is increased, radiation is lost through the ends of the CPC. For the presented case, $g^T_{b,\vec{r}}$ shifts to ~2% lower values as θ_{yz} is increased from 0° to 60°. The end losses are low since the concentrators have a high aspect ratio $\frac{L}{W}$.

Figures 3.8(b) and (c) compare the incident spectrum for a blackbody at 5777K and the spectrum transmitted by the CPC, for direct normal beam radiation and diffuse radiation respectively. These plots can be used to predict the visible transmittance and the solar heat gain for the solar window employing the considered CPC geometry. For each wavelength λ, the value of the ordinate indicates the fraction of rays transmitted though the CPC having wavelengths within $\lambda \pm 5$ μm. In both graphs, a peak is observed near 520-550nm, corresponding to the peak of the photopic luminosity function.

3.5.2 Case study

Results for east and south facing vertical windows and a horizontal skylight are presented for Minneapolis, MN to illustrate their performance in northern latitudes. Figure 3.9 shows the monthly global radiation (beam + diffuse) transmitted through a single low-iron glazing for the three cases. The horizontal skylight receives an annual radiation of 1208 kWh/m^2. The east and south facing windows receive 752 and 1007

49

kWh/m^2, respectively. The horizontal skylight and the east facing façade receive maximum radiation in the summer (May to August), while the south facing façade receives maximum radiation in the winter months (October to March). A combination of a horizontal skylight and vertical windows installed with the hybrid concentrators can be used in the concentrating mode in the summer for passive space cooling and heating loads. The south facing window can be used in the non-concentrating mode in the winter for passive space heating during daylight hours. The non-concentrating mode can be employed during the night to lower thermal losses.

In this section we consider the impact of the CPC geometry on the annual thermal efficiency and the diffuse visible transmittance through the solar window for the concentrating mode of operation. The nominal half-acceptance angle θ_c is varied from 25º to 45º and the respective concentrators are truncated as described in Section 3.3. The resulting geometrical concentration factor C_e ranges from 2.3 at θ_c=25º to 1.5 at θ_c=45º for the horizontal skylight and from 2.6 at θ_c=25º to 1.5 at θ_c=45º for the vertical window.

3.5.2.1 Horizontal skylight

The diffuse visible transmittance for the horizontal skylight is plotted in Fig. 3.10 as a function of θ_c. The corresponding number of concentrators (or equivalently, the number of absorber tubes) n is also indicated on the abscissa. As θ_c is increased, the overall size of the concentrator decreases and consequently the number of concentrators is increased. The solid curves represent a single low-iron glazing and the dashed curves represent double glazing. For reference, curves 1 and 4 provide the transmittance for the

low iron glazing only. Curves 2 and 5 provide the transmittance through the selective film plus the low iron glazing. The transmittance for the entire hybrid window assembly (glazing + selective film + absorbers) is represented by curves 3 and 6 for single and double glazed systems respectively. The transmittances of the single and double glazing are 0.83 and 0.74 respectively (curves 1 and 4). With the addition of the wavelength selective film, the transmittance decreases to ~0.77 and ~0.69 respectively (curves 2 and 5) and is constant for the concentrator geometries considered. The visible transmittance of the hybrid system varies from 0.65 to 0.58 (curve 3) for a single glazed skylight and from 0.58 to 0.51 (curve 6) for a double glazed skylight as θ_c is increased from 25° to 45°. Shading by the absorber tubes account for 35-50% of the transmission loss through the entire system.

Figure 3.11 shows the annual thermal efficiency for single (solid line) and double (dashed line) glazed skylights as a function of the half-acceptance angle θ_c. As θ_c is increased, the CPC accepts a wider angular range of incident beam radiation. Consequently, the effective concentration factor C_e decreases and a larger fraction of the diffuse radiation $(\sim\frac{1}{C_e})$ reaches the absorber tube. Thus, annual thermal efficiency increases from 0.22 to 0.28 for single glazing and from 0.21 to 0.26 for double glazing as θ_c is increased from 25° to 45°. Double glazing reduces the thermal losses and the overall loss factor U_L, but also lowers the transmission of incident radiation. The net result of using double glazing is a drop in the annual thermal efficiency by ~1.5%. Although double glazed systems indicate a drop in visible transmittance and thermal efficiency, they offer better thermal insulation and are widely preferred for fenestrations.

3.5.2.2 Vertical window

Plots similar to those for the horizontal skylight are presented for the south and east facing vertical windows in Figs. 3.12 and 3.13. Figure 3.12 shows the visible transmittance for diffuse radiation, a quantity independent of the window orientation. As in the case of the skylight, the addition of the wavelength selective film decreases the transmission slightly (~6% percentage points), but the concentrator shape has negligible impact on the visible transmittance. The number of absorber tubes governs the transmittance through the system. The visible transmittance of the hybrid vertical window varies from 0.66 to 0.55 for single glazing and from 0.59 to 0.49 for double glazing. The visible transmittance for the hybrid vertical window is nearly identical with the hybrid skylight for geometries with the same number of absorber tubes. For example, with $\theta_c = 35°$, $\tau_{vis,d} = 0.63$ for the vertical window. For a skylight with the same number of absorber tubes, $\tau_{vis,d} = 0.64$.

The thermal efficiency of the hybrid systems depends strongly on the concentrator geometry and the orientation. Figures 3.13(a) and (b) plot the annual thermal efficiency for the south and east facing windows, respectively, as a function of θ_c. The thermal efficiency increases from 0.21 to 0.28 for single glazing and 0.19 to 0.26 for double glazing in case of the south facing window, and from 0.17 to 0.17 for single glazing and 0.16 to 0.25 for double glazing for the east facing window as θ_c is increased from 25° to 45°.

3.5.3 Comparison with commercial fenestration systems

Table 3.3 lists the NFRC visible transmittance τ_{vis}, solar heat gain coefficient

$SHGC$, and U-factor for the vertical 'solar window' for nominal half-acceptance angles $25° \leq \theta_c \leq 45°$. At $\theta_c = 25°$, τ_{vis} is 0.73 for single glazing and is 0.67 for double glazing. As θ_c is increased to $45°$, τ_{vis} decreases to 0.66 for single glazing and 0.61 for double glazing. This trend is similar to the trend for the diffuse visible transmittance $\tau_{vis,d}$. The values of τ_{vis} are higher than the corresponding values of $\tau_{vis,d}$ due to higher transmittance through the glazing for direct normal beam radiation (0.91 and 0.825 for single and double glazed low-iron clear glass). Because the hybrid window concentrates the infrared portion of the solar spectrum onto the absorber tube, the solar heat gain coefficient for the window is lowered. Further, the additional insulating air cavity formed by the concentrators increase the thermal resistance of the window, lowering the U-factor. $SHGC$ and the U-factor are relatively insensitive to changes in θ_c. For single glazing, $SHGC$ changes from 0.48 at $\theta_c = 25°$ and 0.45 at $\theta_c = 45°$. For double glazing, $SHGC$ is ~0.43. The U-factor for the solar window is 3.1 W/m²K and 2 W/m²K for single and double glazing respectively.

Table 3.4 lists the values of the NFRC center-of-glazing τ_{vis}, $SHGC$, and U-factor calculated for commercial single and double glazed fenestration systems calculated using WINDOW [5]. The visible transmittance of the single glazed solar window is equivalent to or higher than several options presented for single glazed fenestrations, such as grey tinted glass (1.2), tinted glass with low-e coating (1.5, 1.6) and glass with reflective coating (1.7, 1.8). Similarly, the visible transmittance of the double glazed solar window is comparable to commercial double glazed fenestrations, only surpassed by the double clear glass (2.1), the combination of green tinted glass and clear glass (2.3), and the double clear glazing with a low-e coating (2.4). In fact, the double glazed solar window

has higher visible transmittance than several single glazed fenestrations (tinted glass (1.2, 1.5, 1.6), glass with reflective coating (1.8)).

In addition to serving as daylighting devices, windows are required to thermally insulate the interior space. The solar heat gain coefficient for the proposed hybrid solar window is approximately mid-way between the solar heat gains for the corresponding single or double glazed commercial windows. Both, the single and double glazed hybrid windows have lower solar gains than corresponding single or double glazed commercial systems employing clear glass, tinted glass or a combination (1.1-1.3, 1.7 for single glazed systems and 2.1-2.3 for double glazed systems). The thermal advantage of spectrally selective glazing systems is often quantified by the light to solar gain (LSG) which is the ratio of the visible transmittance to the solar heat gain coefficient. Both the single and double glazed hybrid windows have LSG in the range 1.48-1.55. This ratio is superior to a majority of the presented commercial systems. Only single glazed low-e coated on clear or low-e coated on green tinted glass (1.4, 1.6) or double glazed systems with one or more low-e coated layer (2.4, 2.6, 2.9, 2.10) have a higher spectral selectivity.

With regards to the U-factor, the single glazed hybrid window has better or equivalent heat insulation properties as compared to single glazed fenestrations. This improvement is due to the presence of an additional insulation air cavity enclosed by the concentrator. The U-factor for the double glazed solar window is lower than double glazed fenestrations that do not employ a low-coating, and is only 0.3 W/m^{2}K higher than the ones that employ a single coating (2.4-2.6). Double glazed windows with two low-e coated glass layers (2.9, 2.10) have better heat insulation.

54

In summary, the double glazed solar window has daylighting and heat insulating properties that are better than clear, tinted or reflective glazing, and comparable to double glazed commercial windows with single low-e coating. The solar window design has the added flexibility of possible operation in a non-concentrating mode to achieve higher solar heat gain for passive space heating, if required. In this mode, the visible transmittance of the solar window will also be 4-5 percentage points higher due to removal of the wavelength selective film.

3.6 Conclusion

A unique concept for a hybrid solar window that uses a wavelength selective film to split the incident radiation into spectral bands for daylighting and heating is presented for the first time. A Monte Carlo ray tracing model is used to analyze the annual thermal and daylighting performance of the hybrid window. In the present study, vertical windows and a horizontal skylight in Minneapolis, MN are evaluated to illustrate the versatility of the concentrator design to different façade orientations and to predict the impact of the concentrator geometry on the daylighting and thermal performance of the window. The performance of the proposed solar window is compared to commercial fenestration systems.

The daylighting performance of the solar window is characterized by the visible transmittance, calculated for diffuse radiation to emulate a uniform overcast sky, and for direct normal radiation according to the standard set by the National Fenestration Rating Council (NFRC). The visible transmittance is relatively insensitive to concentrator shape, but depends strongly on the number of absorber tubes, which block light. As the half-acceptance angle θ_c of the CPC is increased from 25º to 45º, the diffuse visible

transmittance of the double glazed solar window changes from 0.59 to 0.49 and the NFRC visible transmittance changes from 0.67 to 0.61. The solar heat gain coefficient and the U-factor for these geometries is relatively constant having values of 0.44-0.42 and 2 W/m²K respectively. For commercial double glazed fenestration systems, the visible transmittance, the solar heat gain coefficient and the U-factor can range from 0.19-0.84, 0.31-0.84 and 1-2.7 W/m²K respectively. With respect to heat insulation (U-factor) and spectral selectivity ($^{\tau_{vis}}/_{SHGC}$), the hybrid solar window has performance that is equivalent to or closely approaches double glazed systems with low-e coating.

The hybrid solar window is extremely versatile in terms of its functional adaptability and utilization of the solar resource. The proposed hybrid window harnesses energy not used for daylighting to generate sensible heat that can offset the hot water loads of the daylit space. The thermal efficiency of the window is a strong function of the CPC geometry. It ranges from 21-26% for a horizontal skylight and from 18-24% and 15-23% for south and east facing windows for CPC geometries ranging from -25°≤ θ_c ≤45°. The hybrid window can also be used in an alternative, non-concentrating mode in which it has higher solar heat gains.

The proposed hybrid solar window offers a compelling possibility for alternative, energy efficient glazing systems. The architecturally integrated design, adaptability and multi-functionality offered by the hybrid window could drive future concepts for integration of solar energy into the built environment. Figure 3.14 shows one such rendering of a building facade consisting of the proposed hybrid window and skylights.[2]

3.7 Tables and Figures

Table 3.1. Assumptions and system properties for the annual thermal model

Property	Value
Geographical location	Minneapolis, MN
Aperture area A_c	1m x 1.5m
Absorber tube diameter D	0.016m
Heat transfer fluid	Ethylene glycol 40% (v/V)
Mass flow rate	0.015 kg/s-m^2
Inlet fluid temperature T_{fi}	293K
Absorber absorptance α_a	0.94
Absorber emittance ϵ_a	0.09 (Duffie and Beckman, 2006)
Cover emittance ε_c	0.84
CPC emittance ε_m	0.85 for acrylic (Duffie and Beckman, 2006)

Table 3.2. Standard NFRC environmental conditions

Standard	T_{in} (ºC)	T_b (ºC)	v_w (m/s)	G (W/m^2)
NFRC 200-2010	24	32	2.75	783
NFRC 100-2010	21	-18	5.5	0

Table 3.3. The NFRC visible transmittance, solar heat gain coefficient and U-factor the vertical solar window application for considered CPC geometries

θ_c	Single glazing			Double glazing		
	τ_{vis}	$SHGC$	U-factor (W/m^{2}K)	τ_{vis}	$SHGC$	U-factor (W/m^{2}K)
25	0.73	0.48	3.1	0.67	0.44	2.0
30	0.72	0.47	3.1	0.66	0.43	2.0
35	0.70	0.47	3.1	0.64	0.43	2.0
40	0.67	0.46	3.1	0.61	0.42	2.0
45	0.66	0.45	3.1	0.61	0.42	2.0

Table 3.4. The NFRC visible transmittance, solar heat gain coefficient and U-factor for commercial single and double glazed window systems

|	Glass Type	τ_{vis}	SHGC	U-factor (W/m²K)
	Single glazed units (center of glazing)			
1.1	Low iron clear glass	0.91	0.91	5.71
1.2	Tinted glass (grey)	0.60	0.69	5.70
1.3	Tinted glass (green)	0.77	0.59	5.70
1.4	Low-e on clear	0.78	0.42	2.98
1.5	Low-e on tinted (grey)	0.54	0.36	2.99
1.6	Low-e on tinted (green)	0.69	0.40	3.03
1.7	Reflective on clear	0.36	0.50	5.76
1.8	Reflective on tinted (grey)	0.21	0.41	5.68
	Double glazed units (center of glazing, 12.7mm air layer)			
2.1	Clear + Air + Clear	0.84	0.84	2.69
2.2	Tinted (grey) + Air + Clear	0.54	0.58	2.69
2.3	Tinted (green) + Air + Clear	0.70	0.48	2.69
2.4	Low E on clear + Air + Clear	0.70	0.39	1.64
2.5	Low E on tinted (grey) + Air + Clear	0.49	0.31	1.65
2.6	Low E on tinted (green) + Air + Clear	0.63	0.35	1.67
2.7	Reflective on clear + Air + Clear	0.33	0.39	2.70
2.8	Reflective on tinted (grey) + Air + Clear	0.19	0.33	2.68
2.9	Low E on clear + Air + Low E on clear	0.61	0.33	1.18
2.10	Low E on clear + Argon + Low E on clear	0.61	0.33	0.99
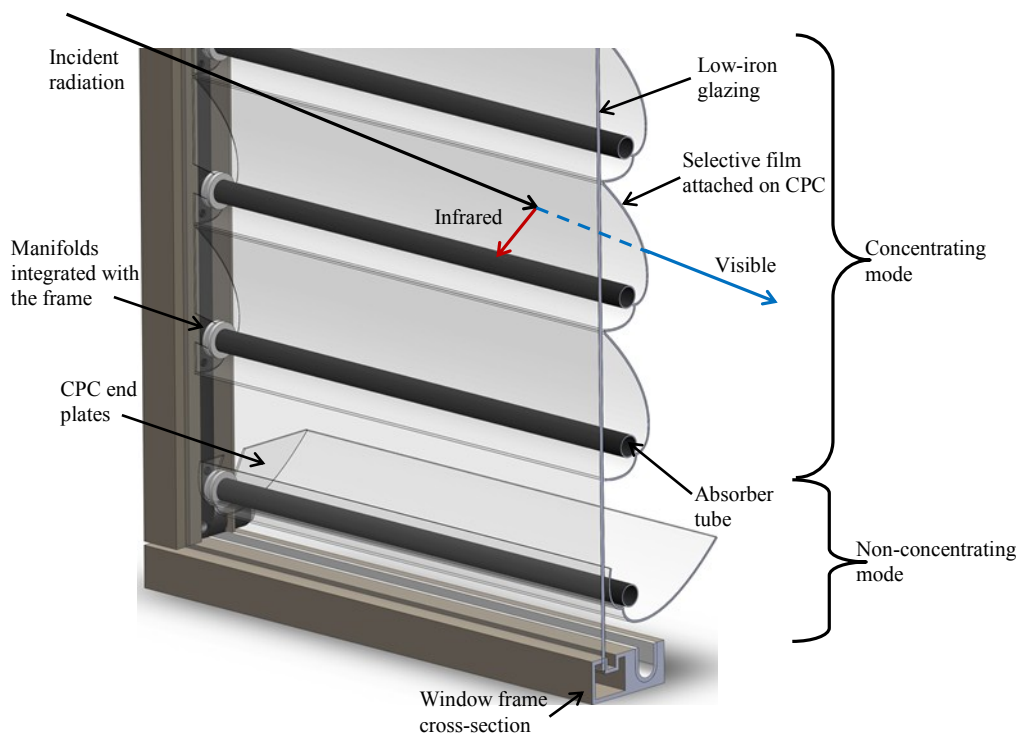
Fig. 3.1. Design concept for the hybrid solar window
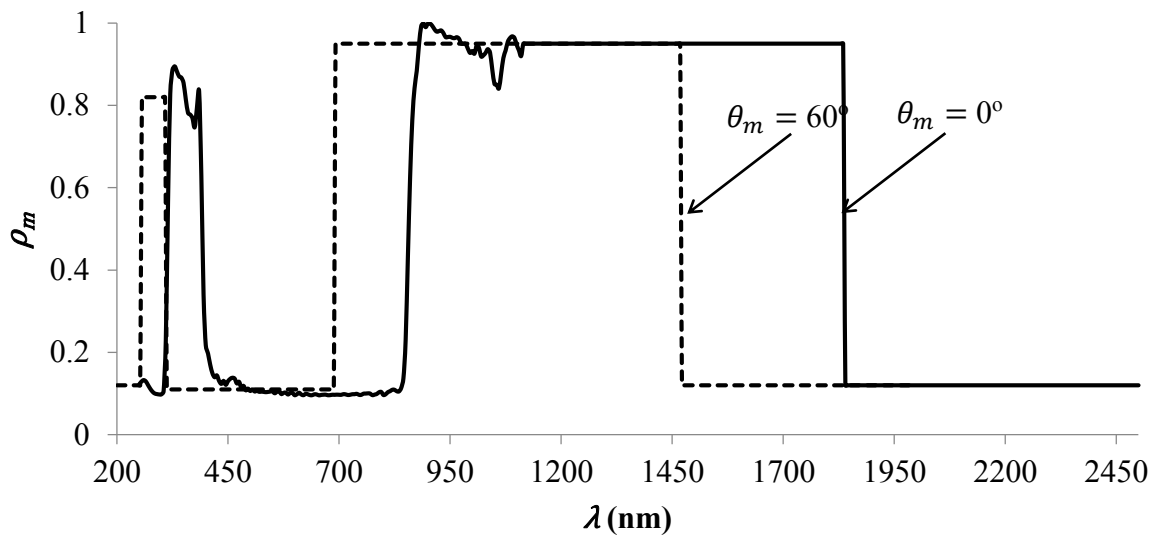
Fig. 3.2. Spectral directional reflectance for the wavelength selective film at 0° and 60° incidence
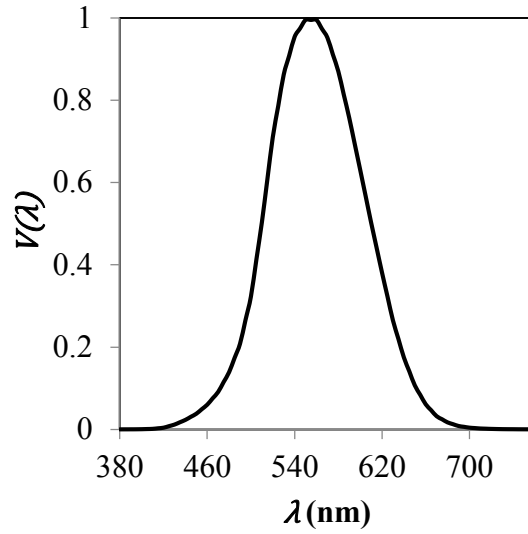
Fig. 3.3. CIE Photopic luminosity function [1]

(a)

(b)
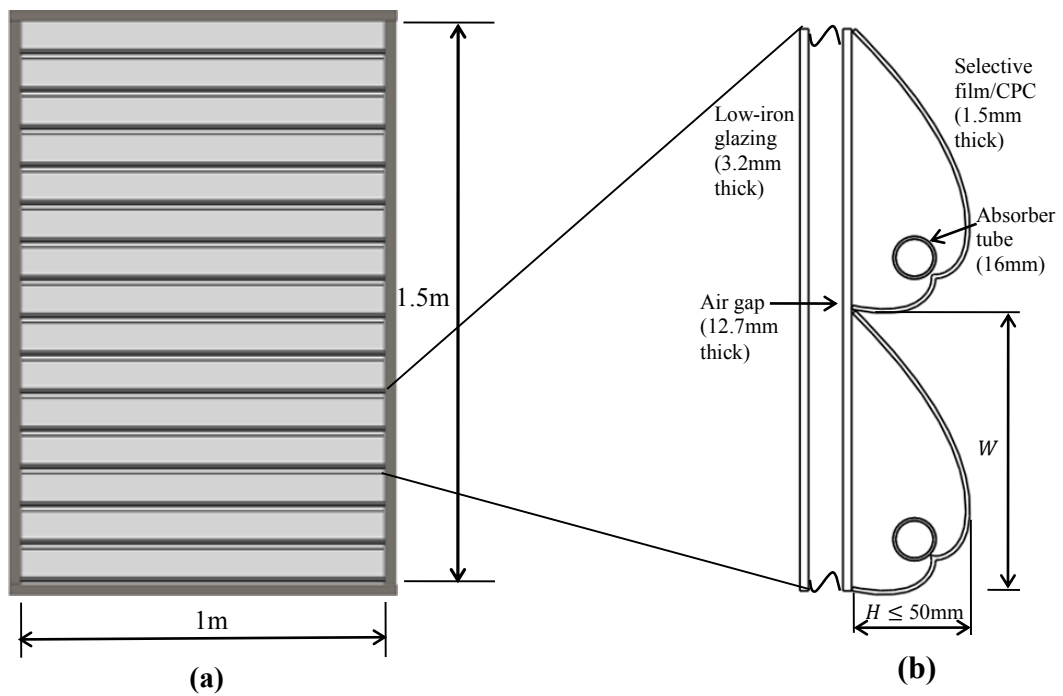
Fig. 3.4. (a) Hybrid window/skylight overall dimensions (b) Typical cross-section of the hybrid system with component thicknesses
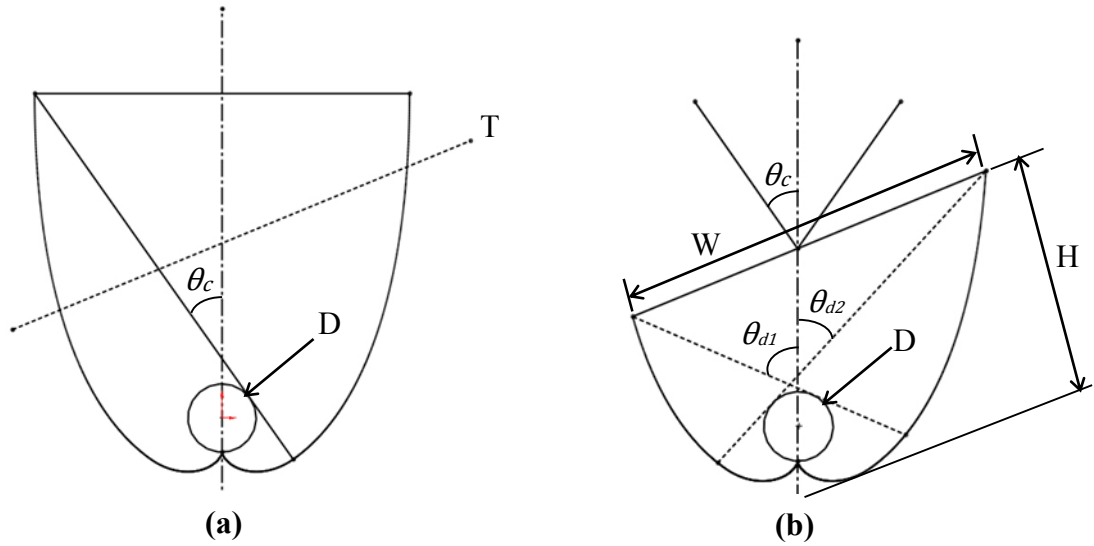
Fig. 3.5. (a) Asymmetrical truncation of a CPC geometry showing truncated and untruncated parameters (b) Resultant asymmetrically truncated CPC
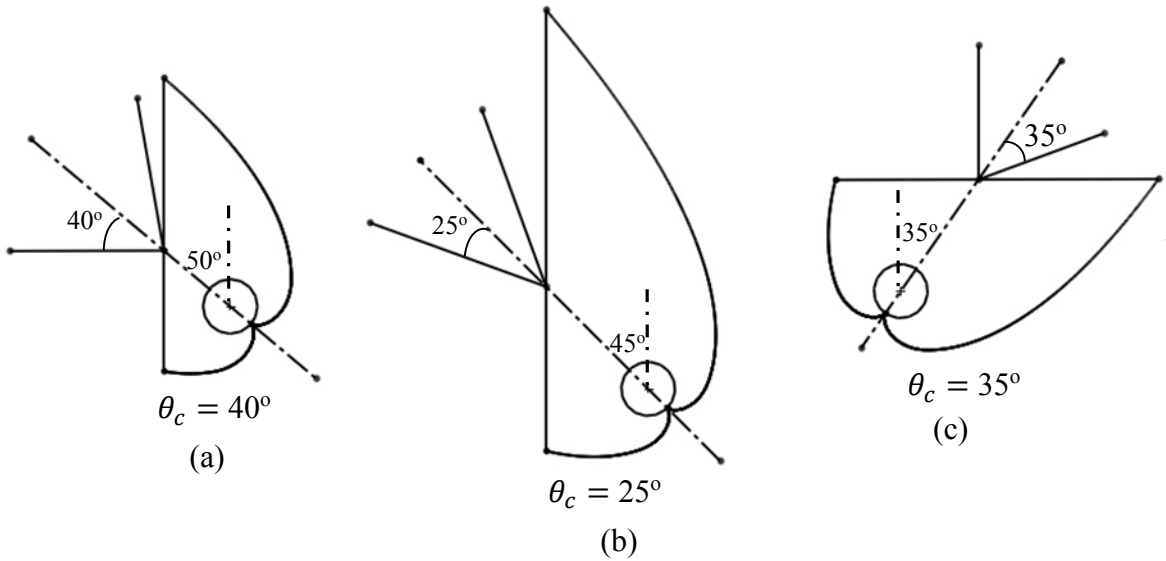
Fig. 3.6. Truncated CPC geometries for (a), (b) vertical window and (c) horizontal skylight for maximum optical efficiency at the absorber tube for the respective half-acceptance angles
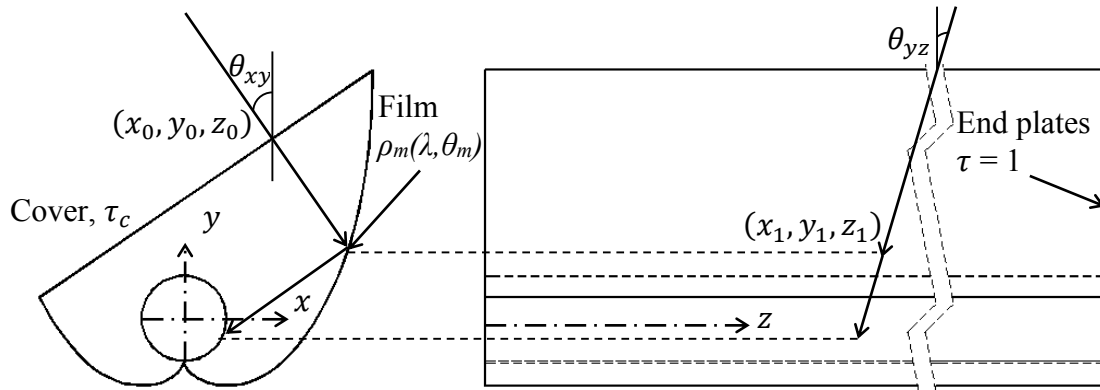
Fig. 3.7. MCRT for a single ray in the asymmetrically truncated CPC cavity
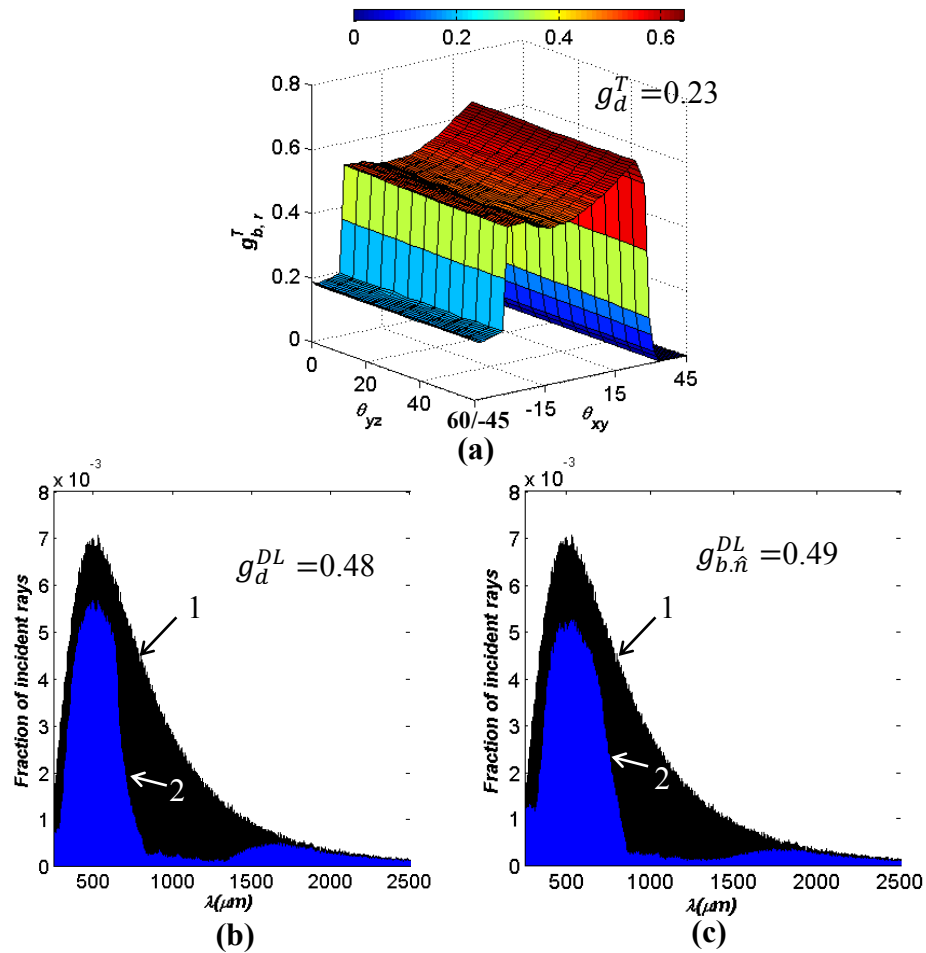
Fig 3.8. (a) The fraction of incident beam radiation reaching the absorber tube as a function of θ_{xy} and θ_{yz} (b) 1-Incident and 2-transmitted spectrum for diffuse radiation (c) 1-Incident and 2-transmitted spectrum for beam radiation normal to the glazing
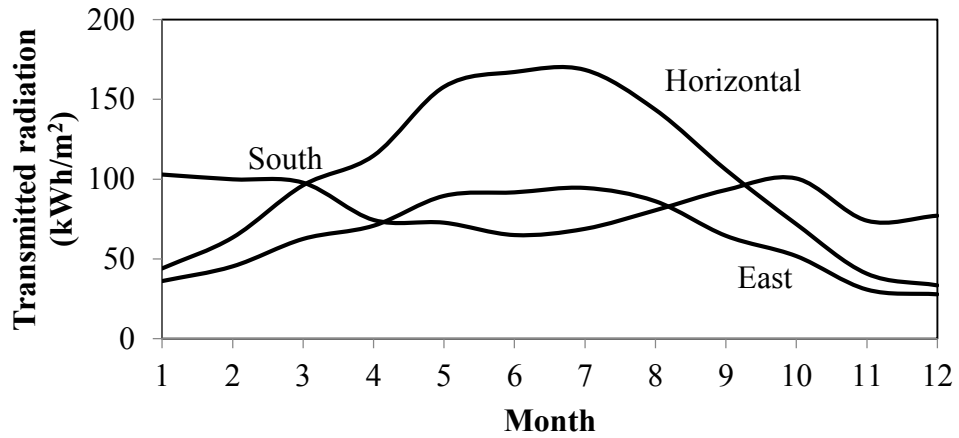
Fig. 3.9. Monthly transmitted radiation for single glazed horizontal skylight and south and east facing windows
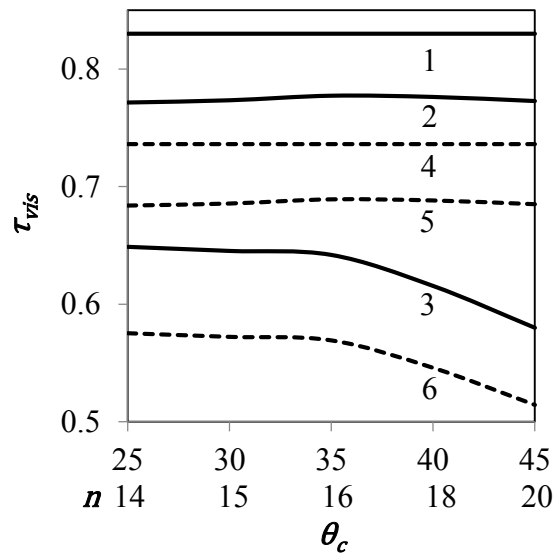
Fig. 3.10. Visible transmittance for diffuse radiation as a function of θ_c for single (solid) and double (dashed) glazed horizontal skylight application. Curves 1, 4 are for glazing alone; 2, 5 are for glazing plus wavelength selective mirror; and 3, 6 are for window assembly

63
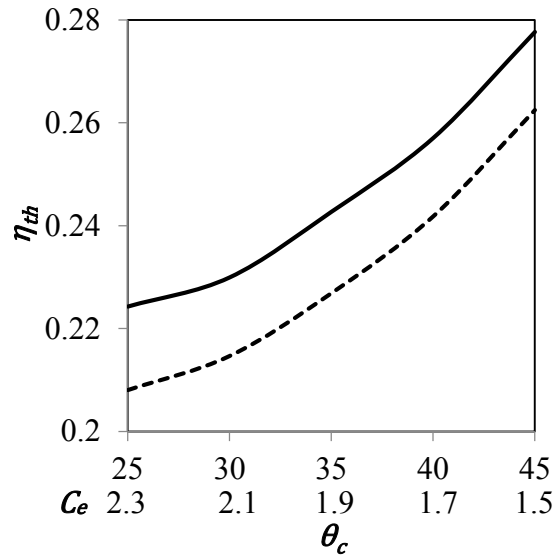
Fig. 3.11. Annual thermal efficiency for single (solid line) and double (dashed line) glazed horizontal skylights as a function of θ_c
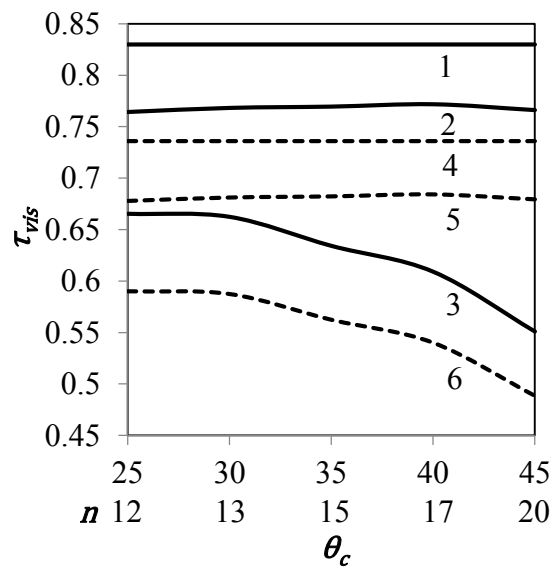
Figure 3.12. Visible transmittance for diffuse radiation as a function of θ_c for single (solid) and double (dashed) glazed vertical window application. Curves 1, 4 are for glazing alone; 2, 5 are for glazing plus wavelength selective mirror; and 3, 6 are for window assembly
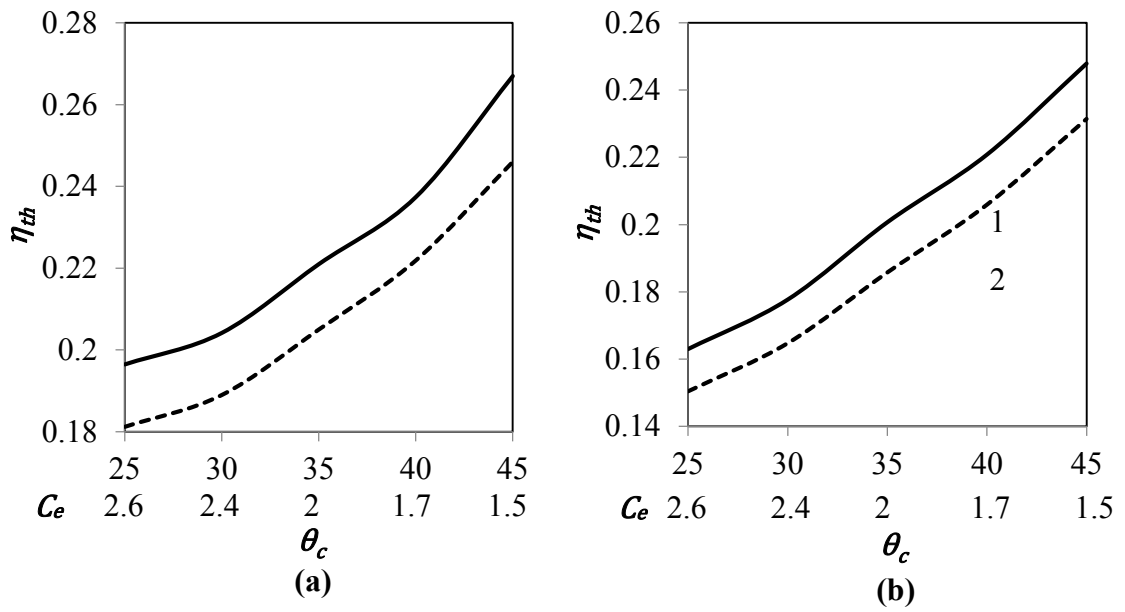
Fig. 3.13 Annual thermal efficiency for single (solid line) and double (dashed line) glazed (a) south facing and (b) east facing vertical window as a function of θ_c

Fig. 2.14 A visual rendering of the the exterior and interior appearance of a building facade employing hybrid solar windows and skylights. [Rendering made by Becky Alexander, School of Architecture, University of Minnesota]

3.8 Nomenclature

A	Area, m^2
C	Geometric concentration factor
c_p	Specific heat capacity at constant pressure, J/kgK
D	Tube diameter, m
F_R	Heat removal rate
G	Incident solar irradiance, W/m^2
g	Fraction of incident solar radiation
h	Heat transfer coefficient, W/m^2K
H	Depth of the CPC, m
L	Length of CPC reflector, m
$\dot{m}$	Mass flow rate, kg/s-m^2
N	Number of rays
n	Number of concentrators/absorber tubes in the collector
R	Random number, uniformly distributed in (0, 1)
Q_u	Useful energy, W/m^2 ($3600J/m^2$ for hourly data)
$\vec{r}$	Direction of incident radiation
S	Energy absorbed per unit absorber area, W/m^2 ($3600J/m^2$ for hourly data)
$SHGC$	Solar heat gain coefficient
T	Temperature, K
U	Net heat transfer coefficient between two surfaces, W/m^2K
U-factor	Net transmittance through the window, W/m^2K
U_L	Overall loss coefficient, W/m^2K

$V(\lambda)$	CIE photopic luminosity function
v_w	Wind velocity, m/s
W	Width of the CPC, m
x, y, z	Cartesian coordinates

Greek symbols

α	Absorptance of the absorber tube
β	PV cell temperature coefficient, $^{o}C^{-1}$
γ	PV cell irradiance coefficient
ε	Emittance
η	Efficiency
θ	Incidence angle, deg
θ_c	Nominal half-acceptance angle, deg
θ_{d1}, θ_{d2}	Truncated half-acceptance angle, deg
λ	Wavelength, nm
ρ	Reflectance
σ	Stefan-Boltzmann constant, J/s-m^{2}K; standard deviation
τ	Transmittance
τ_{vis}	Visible transmittance

Subscripts

a	Absorber tube; absorbed rays
b	Beam radiation
c	CPC glass cover; convection
c_2	Additional CPC glass cover

cd	Conduction
d	Diffuse radiation
e	Effective value
fi, fo	Fluid inlet, outlet
i	Incident rays
in	Interior
m	Wavelength selective film
$\hat{n}$	Normal (to a surface)
r	Radiation
$\vec{r}$	Directional
s	Specular reflection
t	Transmitted rays
th	Thermal module
xy, yz	xy, yz planes
∞	Ambient
λ	Spectral

Superscripts

DL	Daylit space
T	Thermal module

3.9 References

Alvarez, R., González, J.C., Espinós, J.P., González-Elipe, A.R., Cueva, A., Villuendas, F., 2013. Growth of silver on ZnO and SnO2 thin films intended for low emissivity applications. J. Appl. Surf. Sci. 268, 507-515.

Buratti, C., Moretti, E., 2012. Glazing systems with silica aerogel for energy savings in buildings. J. Appl. Energy 98, 396-403.

Chow, S.K.H., Li, D.H.W., Lee, E.W.M., Lam, J.C., 2013, Analysis and prediction of daylighting and energy performance in atrium spaces using daylight-linked lighting controls. J. Appl. Energy.

Chow, T., Li, C., Lin, Z., 2011. Thermal characteristics of water-flow double-pane window. Int. J. Therm. Sci. 50, 140-148.

Chow, T., Li, C., Lin, Z., 2010. Innovative solar windows for cooling-demand climate. Sol. Energ. Mat. Sol. C. 94, 212-220.

Davidsson, H., Perers, B., Karlsson, B., 2010. Performance of a multifunctional PV/T hybrid solar window. Sol. Energy 84, 365-372.

De Rosa, A., Ferraro, V., Kaliakatsos, D., Marinelli, V., 2010. Calculating indoor natural illuminance in overcast sky conditions. Appl. Energy 87, 806-813.

Du, J., Sharples, S., 2011. The variation of daylight levels across atrium walls: Reflectance distribution and well geometry effects under overcast sky conditions. Sol. Energy 85, 2085-2100.

Duffie, J.A., Beckman, W.A., 2006. Solar Engineering of Thermal Processes, Third Edition. John Wiley and Sons, New York.

Gardiner, D.J., Morris, S.M., Coles, H.J., 2009. High-efficiency multistable switchable glazing using smectic A liquid crystals. Sol. Energ. Mat. Sol. C. 93, 301-306.

Gochenour, S.J., Andersen, M., 2009. Circadian Effects of Daylighting in a Residential Environment. In Proceedings LuxEuropa, Istanbul.

Granqvist, C.G., Green, S., Niklasson, G.A., Mlyuka, N.R., von Kraemer, S., Georen, P., 2010. Advances in chromogenic materials and devices. Thin Solid Films 518, 3046-3053.

Howell, J.R., 1998. The Monte Carlo Method in Radiative Heat Transfer. J. Heat Transfer 120(3), 547-560.

Kakaç, S., Shah, R., Aung, W., 1987. Handbook of Single-Phase Convective Heat Transfer. John Wiley and Sons, New York, NY.

Kim, G., Kim, J.T., 2010. Healthy-daylighting design for the living environment in apartments in Korea. Build. Environ. 45, 287-294.

Li, D.H.W., Lam, T.N.T., Chan, W.W.H., Mak, A.H.L., 2009. Energy and cost analysis of semi-transparent photovoltaic in office buildings. Appl. Energy 86, 722-729.

Li, D.H.W., Lam, T.N.T., Wong, S.L., 2006. Lighting and energy performance for an office using high frequency dimming controls. Energy. Convers. Manage. 47, 1133-1145.

Martin-Palma, R.J., 2009. Commentary: Spectrally selective coatings on glass: solar-control and low-emissivity coatings. J. Nanophoton. 3, 030305.

Mlyuka, N.R., Niklasson, G.A., Granqvist, C.G., 2009. Thermochromic multilayer films of VO2 and TiO2 with enhanced transmittance. Sol. Energ. Mat. Sol. C. 93, 1685-1687.

Modest, M.F., 2003. Radiative Heat Transfer, Second Edition. Academic Press.

Mohelnikova, J., 2009. Materials for reflective coatings of window glass applications. Constr. Build. Mater. 23, 1993-1998.

NFRC 100-2010: Procedure for Determining Fenestration Product U-factors, 2010. National Fenestration Rating Council.

NFRC 200-2010: Procedure for Determining Fenestration Product Solar Heat Gain Coefficient and Visible Transmittance at Normal Incidence, 2010. National Fenestration Rating Council.

Page, J., Scartezzini, J.L., Kaempf, J., Morel, N., 2007. On-site performance of electrochromic glazings coupled to an anidolic daylighting system. Sol. Energy 81, 1166-1179.

Piccolo, A., Pennisi, A., Simone, F., 2009. Daylighting performance of an electrochromic window in a small scale test-cell. Sol. Energy 83, 832-844.

Plympton, P., Conway, S., Epstein, K., 2000. Daylighting in Schools: Improving Student Performance and Health at a Price Schools can Afford. American Solar Energy Society Conference, Madison.

Rabl, A., 1976. Optical and thermal properties of compound parabolic concentrators. Sol. Energy 18, 497-511.

ISO 15099:2003 Thermal performance of windows, doors and shading devices - Detailed calculations, 2003. International Organization for Standardization.

Ulavi, T.U., Davidson, J.H., Hebrink, T., 2013. Analysis of a Hybrid PV/T Concept Based on Wavelength Selective Films.

Vandewalle, G., Balteau, E., Phillips, C., Degueldre, C., Moreau, V., Sterpenich, V., Albouy, G., Darsaud, A., Desseilles, M., Dang-Vu, T.T., Peigneux, P., Luxen, A., Dijk, D.J., Maquet, P., 2006. Daytime light exposure dynamically enhances brain responses. Curr. Biol. 16, 1616-1621.

Weber, M.F., Stover, C.A., Gilbert, L.R., Nevitt, T.J., Ouderkirk, A.J., 2000. Giant Birefringent Optics in Multilayer Polymer Mirrors. Science 287, 2451-2456.

Wright, J.L., 1996. A Correlation to Quantify Convective Heat Transfer Between Vertical Window Glazings. ASHRAE Trans. 102, Pt. 1, 940-946.

Xu, X., Gibbons, T.H., Cortie, M.B., 2006. Spectrally-selective gold nanorod coatings for window glass. Gold Bulletin 39, 156-165.

Web based references

[1] Colour and Vision Research Laboratory, CIE Photopic Luminosity function (http://www.cvrl.org/lumindex.htm), last accessed 08/20/2012

[2] Lawrence Berkeley Research Laboratory, RADIANCE (http://radsite.lbl.gov/radiance/)

[3] Integrated Environmental Solutions, IES VE Pro (http://www.iesve.com/software/ve-pro)

[4] AGC, 'Solite'(http://www.agc-solar.com/agc-solar-products/patterned-glass/solite.html), last accessed 04/20/2013

[5] Lawrence Berkeley Research Laboratory, WINDOW (http://windows.lbl.gov/software/window/window.html), last accessed 04/20/2013

Chapter 4

Experimental Validation of the Hybrid Solar Window

Due to the potential shown by the results of the numerical model of the hybrid solar window concept, a prototype device was designed, fabricated and tested. Experimental measurements of thermal performance for a clear day are presented and compared with predictions from the numerical model.

4.1 Construction of the prototype

An asymmetrically truncated CPC geometry having a nominal half acceptance angle θ_c of 35° was selected for a vertical façade. Based on numerical results presented in Chapter 3, at $\theta_c = 35°$, a single glazed hybrid window is predicted to have an annual efficiency of 22% while maintaining close to maximum visible transmittance (0.63). Figure 4.1(a) shows the truncated CPC geometry. A total of 8 concentrators, 0.81m long, along with end plates were thermoformed from 1.5mm thick acrylic. The thermoformed parts incorporated a draft angle of ~15.75° for the end plates in order to make the thermoform mold. The wavelength selective film, a laminate consisting of two different films to give the required broadband reflective properties illustrated in Fig. 2.3, was attached on the inside of the concentrators (excluding the end plates) using transparent adhesive strips. The draft angle reduced the effective length of the concentrators over which the wavelength film was attached by ~0.015m on either side, as shown in Figure 4.1(b).

The hybrid solar window prototype has an effective aperture (glazing) area of 0.81m x 0.78m. Figure 4.2 show photographs of the roof-top facility, and the prototype

with the CPCs in the concentrating and non-concentrating modes. The concentrators were

pivot about the absorber tubes via the end plates and nylon bushings. The window

consists of an aluminum frame to house a low iron glazing and the inlet/outlet manifolds

for the heat transfer fluid. The window has inlet and outlet ports at the bottom of the fluid

flow loop through the collector. The absorber tubes and the fluid manifolds are 0.016m

diameter copper pipes. The absorbers are spray coated with SOLKOTE HI/SORB II, a

commercially available spectrally selective solar paint. The manufacturer reports that the

selective coating has an absorptance of ~0.88-0.94 and an emittance of ~0.2-0.49

depending on the dry film thickness, substrate and surface preparation [1].
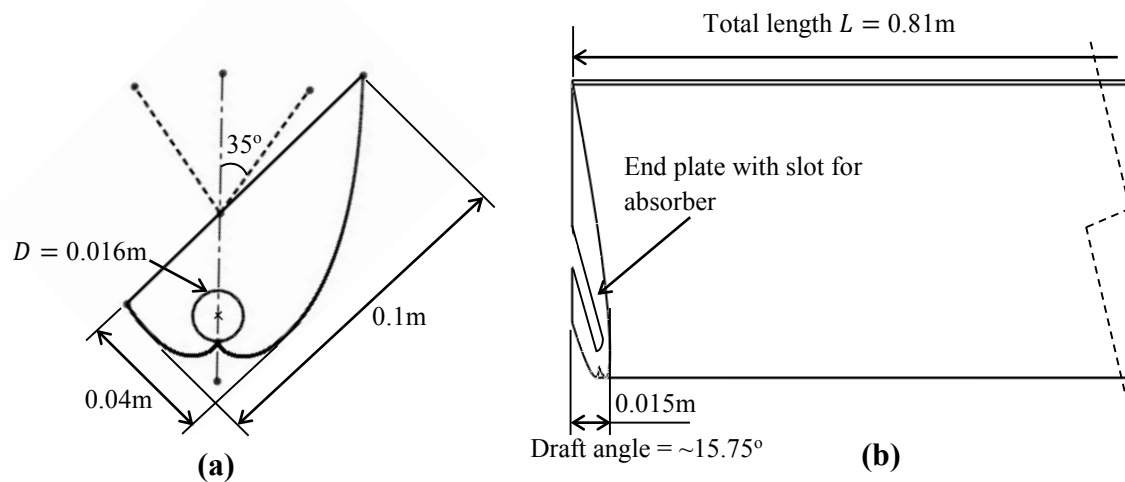

Figure 4.1 (a) CPC geometry (b) Endplate and draft angle for the thermoformed concentrator
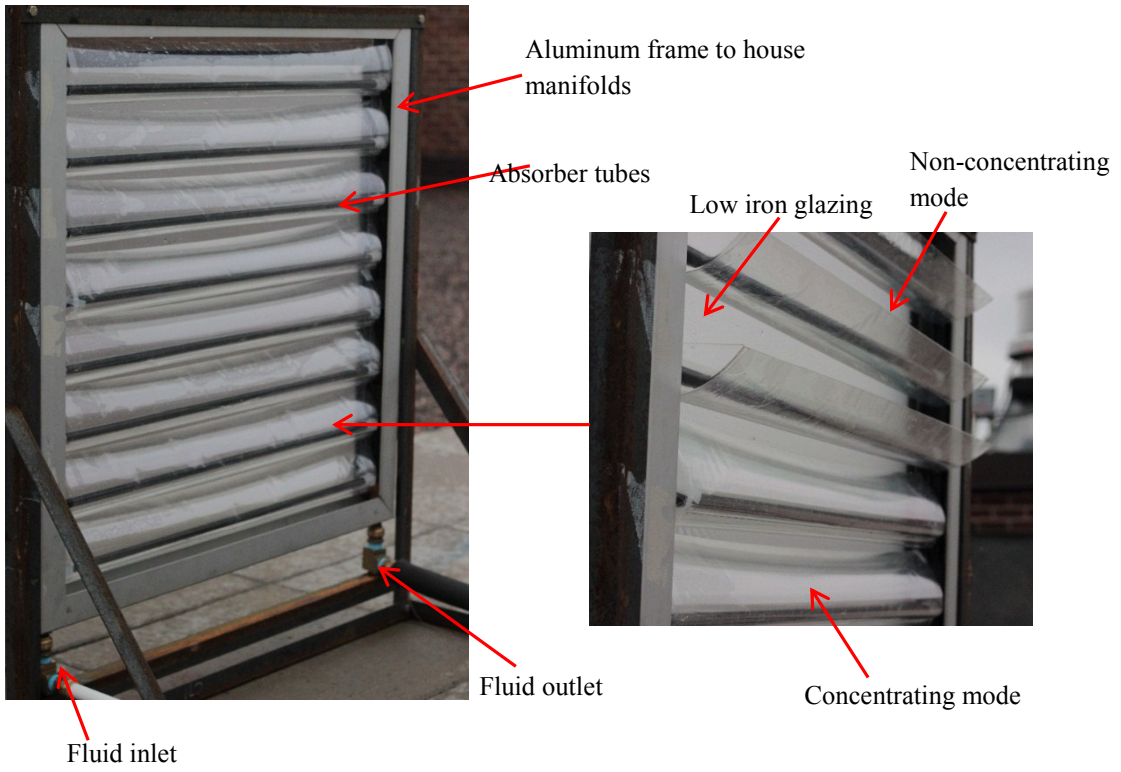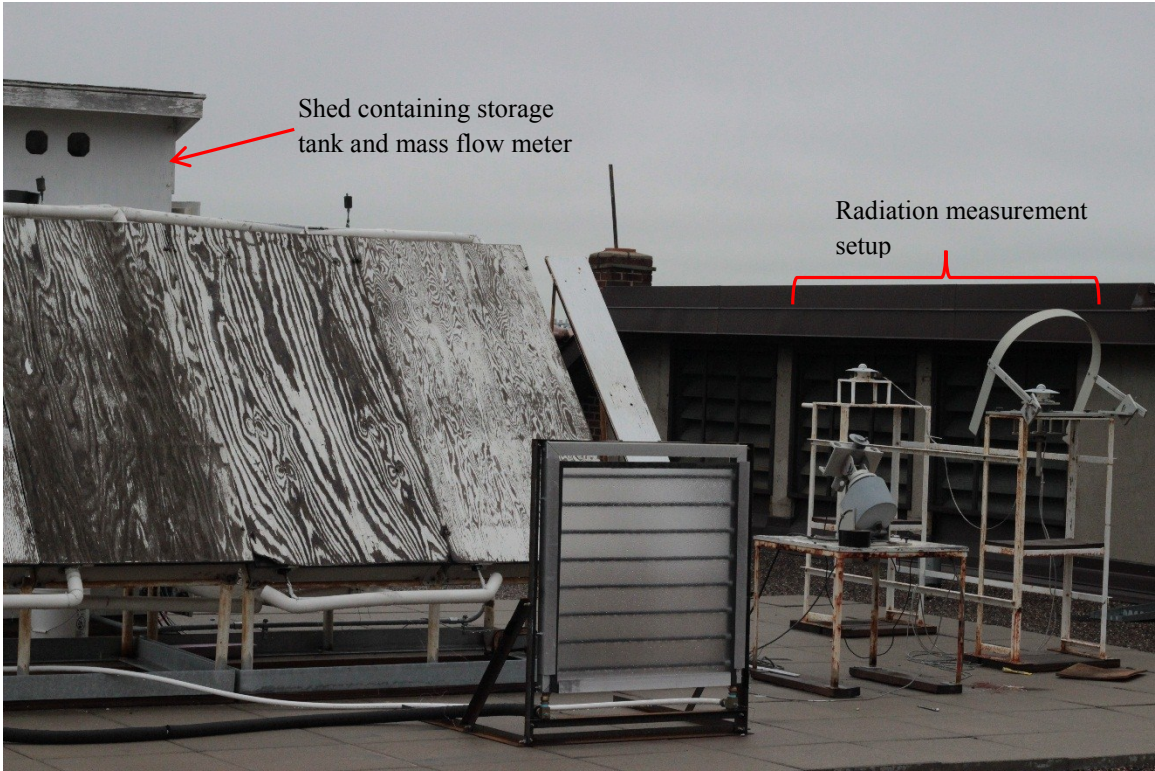
Figure 4.2 The Hybrid solar window prototype

4.2 Experimental Apparatus and Procedure

Figure 4.3 shows the schematic of the outdoor experimental facility used for measuring the thermal efficiency of the hybrid collector. It consists of a 160 liter insulated storage tank filled with 40% by volume ethylene glycol/water. The tank and the associated pump and flow control devices are stored in a wooden shed on the roof of the Mechanical Engineering Building. The solar window was mounted outdoors in the vertical orientation and facing south.

The fluid was circulated through the system using a Teel Model 2P079B pump at a system pressure of ~30 psi. A Micro Motion manufactured Coriolis Model D40 mass flow meter having an accuracy of $\pm$0.2% of the reading was used to measure the total mass flow rate through the tubes. The mass flow rate was adjusted with a needle valve. Fluid temperatures were measured by inserting special limit T-type thermocouples having an accuracy of $\pm$0.5°C into the fluid stream at the inlet and outlet of the collector. A third thermocouple, shaded from direct solar radiation was used to measure the ambient temperature. The setup consists of three devices to measure solar radiation on a horizontal plane. These include a pyranometer to measure total irradiance, a pyreheliometer to measure the direct normal (beam) irradiance and a pyranometer with a shading ring to measure the diffuse irradiance. The pyranometers (Model PSP) and pyreheliometer (Model NIR) were manufactured by the Eppley Laboratory. The shaded and unshaded pyranometers have calibrated sensitivities of 10.06 and 9.23 μV/Wm^{-1} and an accuracy of $\pm$1.5% of reading. The pyreheliometer has a sensitivity of 7.13 μV/Wm^{-1} and an accuracy of $\pm$1.2% of reading. The incident radiation on the collector plane is calculated using determined values for solar zenith and azimuth angles. All instrument

output signals were measured using an Agilent 34970A data acquisition unit having an accuracy of less than 0.005% for voltage measurements, which is negligible in comparison with the instrument uncertainties.

The tank was pressurized with the ethylene glycol/water mixture two to three hours before the beginning of the experiment. The mass flow rate was maintained at ~0.0066 via periodically adjusting the needle valve. The initial two to three hours of operation allowed the system to reach a steady mass flow rate. The fluid inlet, outlet and ambient temperatures, the mass flow rate and the solar irradiance data were recorded every one minute interval. The shading bar on the pyranometer for diffuse radiation was adjusted periodically.
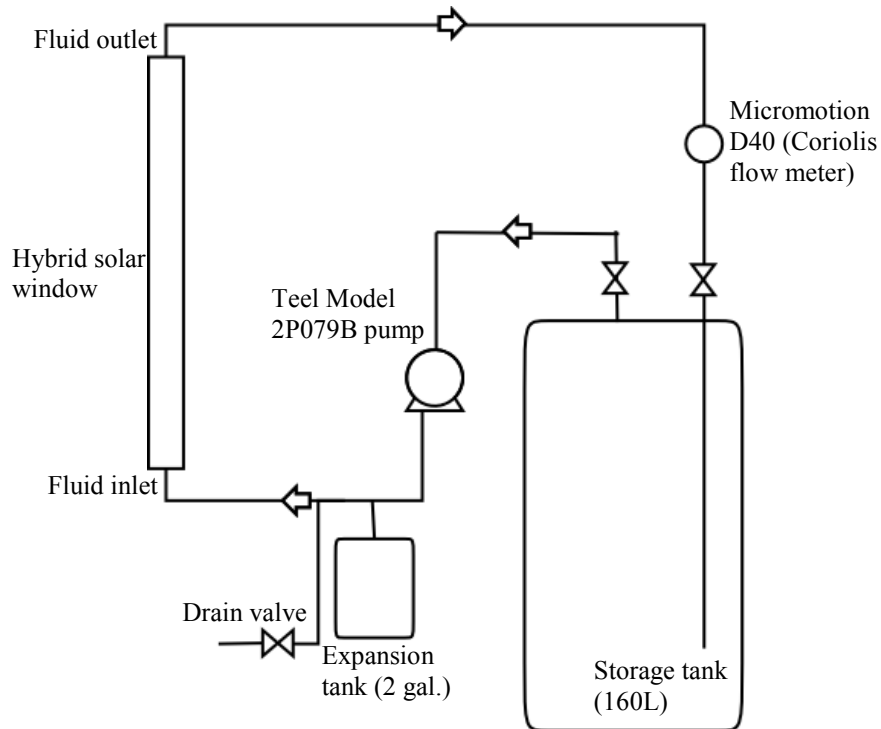

Figure 4.3 Experimental setup for measuring thermal efficiency of the hybrid solar window

4.3 Data Analysis

The incident beam and diffuse radiation on a vertical surface were calculated from the direct normal irradiance and total and diffuse irradiance on a horizontal surface using the solar zenith θ_z and solar azimuth γ_s angles for Minneapolis, MN (44.98°N, 93.27°W). The azimuth angle is assigned a negative sign if it is east of south, otherwise it is assigned a positive sign.

$$\cos\theta_z = \cos\phi\cos\delta\cos\omega + \sin\phi\sin\delta \tag{4.1}$$

$$\cos\gamma_s = \frac{\cos\theta_z\sin\phi - \sin\delta}{\sin\theta_z\cos\phi} \tag{4.2}$$

where δ, ϕ and ω are the local latitude (44.98°N), the solar declination angle and the hour angle respectively.

$$\delta = 23.45\sin\left(360\frac{284+n}{365}\right) \tag{4.1}$$

$$\omega = 15(LST - 12) \tag{4.5}$$

n is the day of the year (in this case, 127) and LST is the local solar time, calculated using the approach presented in [2]. For a south facing collector having a slope $\beta = 90°$, the incidence angle with the vertical surface, θ, is calculated from Eq. (4.6).

$$\cos\theta = \cos\theta_z\cos\beta + \sin\theta_z\sin\beta \tag{4.6}$$

The beam radiation on a vertical surface is

$$G_{b,v} = G_{b,\hat{n}}\cos\theta \tag{4.7}$$

The diffuse component on the vertical surface consists of two components – the diffuse sky radiation and the ground reflected diffuse radiation. Assuming an average reflectance ρ_g of 0.2 from the ground (for cement), the total diffuse component of radiation on the vertical surface is given by

$$G_{d,v} = G_h \frac{1+\cos\beta}{2} + G_{r,v} \qquad (4.8)$$

$$G_{r,v} = \rho_g G_h \frac{1-\cos\beta}{2} \qquad (4.9)$$

The relative uncertainties in $G_{b,v}$ and $G_{r,v}$ are $\pm 1.2\%$ and $\pm 1.5\%$. The uncertainty is calculated from the propagation of error resulting from individual measurements using the Root-Sum-of-Squares method (Appendix E).

The measured rate of useful energy transferred to the fluid $\dot{Q}_{u,m}$ was analyzed assuming a quasi-steady process. The heat transfer was determined over one minute intervals from measured values of mass flow rate and the temperature difference across the collector as

$$\dot{Q}_{u,m} = \dot{m} c_p (T_{fo} - T_{fi}) \qquad (4.10)$$

$\dot{m}$ is the area mass flow rate per unit aperture area of the collector, and has an uncertainty of $\pm 1.1\%$ of reading. Specific heat, c_p, was evaluated assuming a bulk temperature of $\frac{T_{fo}+T_{fi}}{2}$. The temperature difference is measured with an absolute uncertainty of $\pm 0.7^\circ C$. This measurement was the major source of experimental uncertainty. The total useful energy $Q_{u,m}$ can be calculated by integrating $\dot{Q}_{u,m}$ over time.

The numerical heat transfer model to predict the hourly useful energy gain S and the useful energy Q_u is presented in Section 3.2. This model can be used to determine an instantaneous rate of useful energy gain $\dot{S}$ and useful energy $\dot{Q}_u$. The Monte Carlo Ray-Tracing (MCRT) model presented in Section 3.1 predicts the optical efficiency of the hybrid window as a function of the incident direction of solar radiation. The results of the MCRT along with the beam and diffuse radiation on the vertical surface, measured fluid inlet and ambient temperatures, and the measured mass flow rate serve as inputs to the

Table 4.1 Inputs to the thermal model

Parameter	Value
Absorber absorptance α_a	0.9
Absorber emittance ε_a	0.25
Mass flow rate $\dot{m}$	~0.0106 kg/s-m^2 (Measured data)
Inlet temperature T_{fi}	Measured data
Ambient temperature T_∞	Measured data
Wind velocity v_w	1 m/s

numerical model. Absorber tube absorptance and emittance were assumed to be 0.9 and

0.3 respectively, within the range specified by the selective coating manufacturer. Table

4.1 shows the inputs to the numerical heat transfer model. Parameters not listed in the

table such as the glazing and film properties are listed in Section 3.4 of the thesis.

The incident heat flux and the useful energy generated are treated as quasi-steady

for each measurement ($\Delta t = 60$s). Thus, the thermal efficiency over any time period can

be calculated by

$$\eta_{th,m} = \frac{\sum_t \dot{Q}_{u,m} \Delta t}{\sum_t G_v \Delta t} \qquad (4.11)$$

The numerical code calculates the thermal efficiency using Eq. 3.7.

4.3 Results

The presented data were collected for a clear day on May 5, 2013 from 10:30 AM

to 3:30 PM in intervals of a minute. More than 75% of the total radiation incident on the

vertical window during the day was during these hours. The relative uncertainty in the

measurement of temperature difference between the fluid inlet and outlet exceeded 40%

for measurements before 10:30 AM and after 3:30 PM. Hence, these data are not

presented. The mass flow rate through the flow meter was maintained at 0.0066 kg/s,

which for an aperture area of 0.63m^2 gives a mass flow rate of 0.0106$\pm$1.1% kg/s-m^2.
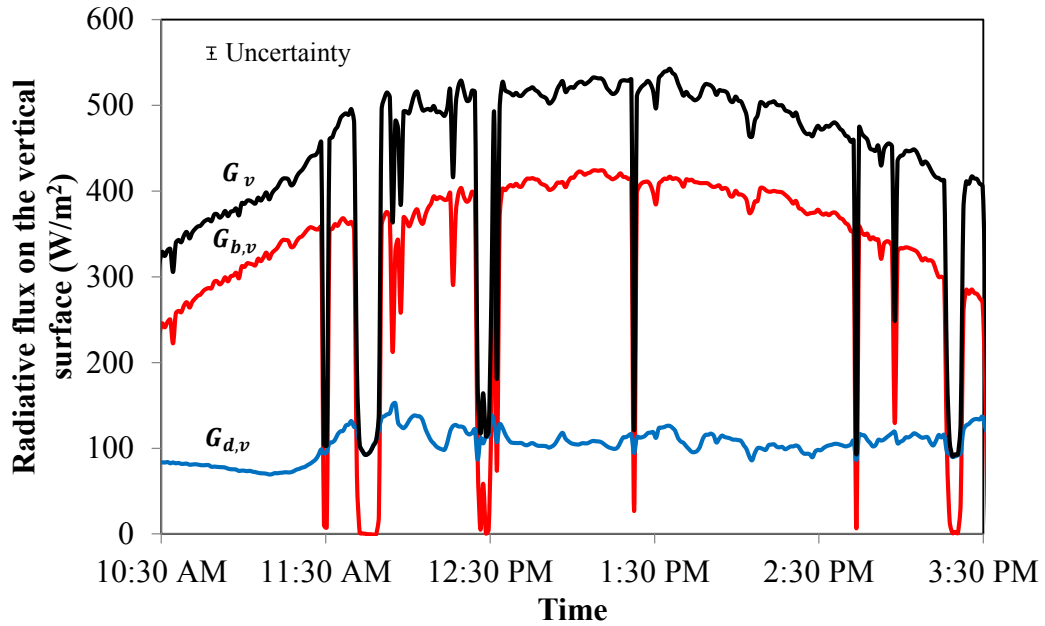
Figure 4.4 Calculated vertical components of radiation – global vertical irradiance, beam vertical irradiance and diffuse vertical irradiance

Figure 4.4 shows the global ($\pm 0.9\%$-$\pm 1.5\%$), beam ($\pm 1.2\%$) and total diffuse ($\pm 1.5\%$) radiation on a vertical surface. The beam radiation is in the range 250-400 W/m^2, approximately 76% of the total radiation. Diffuse radiation (sky + reflected) is relatively constant at around 100W/m^2. The sharp dips observed in the data are due to cloud cover at certain times during the day. The average uncertainty in the quantities over the measured time is shown in the graph.

Figure 4.5 shows measured inlet (T_{fi}), outlet (T_{fo}) and ambient (T_b) temperatures ($\pm 0.5\%$) on the left ordinate. The ambient temperature rose from 23 to 25°C during the experiment. An average fluid temperature rise of ~2.6$\pm$0.7 °C was obtained during time duration presented.

Figure 4.6 compares the measured instantaneous rate of useful energy $\dot{Q}_{u,m}$ to the instantaneous rates of useful energy gain $\dot{S}$ and useful energy $\dot{Q}_u$ predicted by the
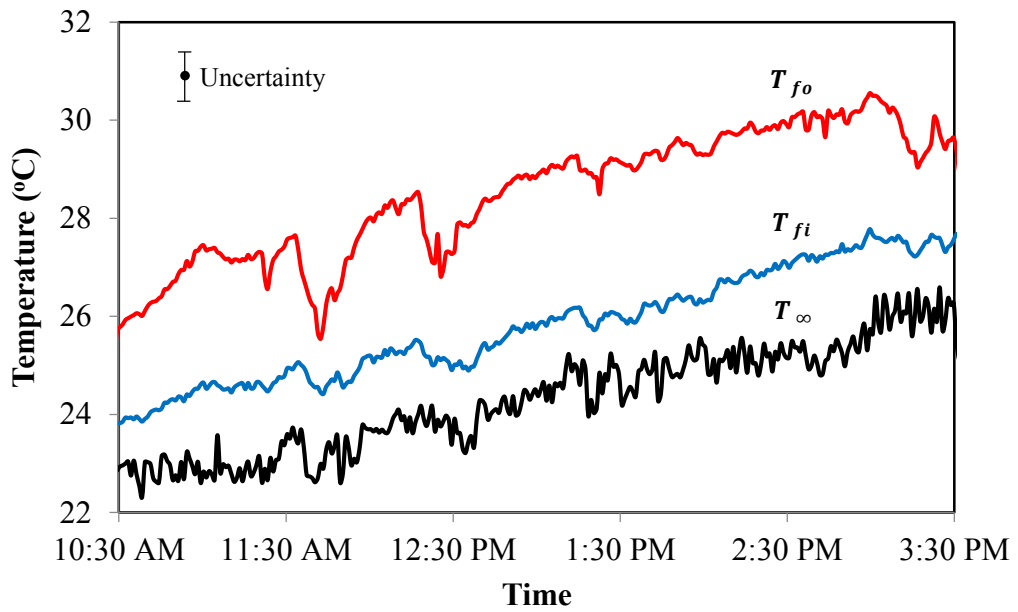
Figure 3.5 Measured inlet, outlet and ambient temperatures
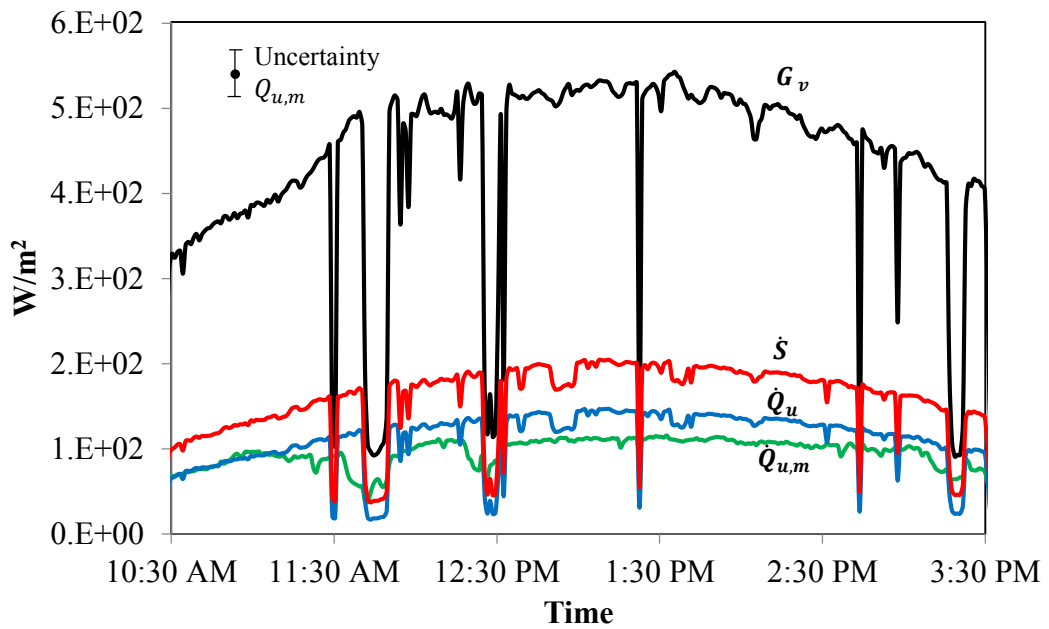
Figure 4.6 Comparison between the measured (green) and predicted (blue) useful energy. Total energy on the vertical surface (black) and the predicted energy gain (red) are given for reference

numerical heat transfer model. For reference, the total energy incident on the vertical surface is plotted. The relative uncertainty is $\dot{Q}_{u,m}$ is $\pm21\%$-$\pm35\%$, due to the uncertainty in the measurement of the temperature difference. The average relative uncertainty of $\pm26\%$ is shown on the graph. The total energy incident on the window from 10:30 AM to 3:30 PM, calculated by taking the area under the entire curve, is 2.2 ± 0.04 kWh/m^2. The numerical model predicts that 36% of this energy is absorbed at the absorber tube ($S = 0.8$ kWh/m^2). The predicted total useful energy generated is 0.56 kWh/m^2 with an efficiency of 25.5%. Q_u is approximately 70% of the useful heat gain. The measured useful energy is 0.48 kWh/m$^2 \pm 0.12$ kWh/m^2 at an efficiency of 22% $\pm$ 5.7%.

The relative difference between the measured and predicted useful energy rate $\left(\frac{Q_u-Q_{u,m}}{Q_u}\right)$ is ~10-23%. This difference is attributed to the following assumptions in the model.

1. The optical properties of the selective coating on the absorber tube depend upon the application technique, and uniformity of the dry-film thickness. The manufacturer's data include a large range of absorptance (0.88-0.94) and emittance (0.2-0.49) values. Changing these optical properties even within this range, would affect the radiative heat transfer characteristics within the CPC cavity. If the absorptance is changed from the assumed 0.9 to 0.88, the thermal efficiency drops by ~2%. A change of emittance from 0.25 to 0.49 causes a decrease in efficiency by ~6%. Changing these parameters together decreases the efficiency by as much as ~8.5%. For the present experiment, the predicted thermal efficiency would decrease to 23.3%.

2. Wind velocities assumed in the numerical model are estimates. The wind velocity and direction would affect the convective heat transfer on the glazed surface as well as from the back of the CPCs. However, the thermal efficiency is found to be relatively insensitive to changes within ± 1m/s in wind velocity. The thermal efficiency changes by less than 1%.

3. The shape of the thermoformed concentrators was not uniform in cross-section along the length of the concentrators. While the total amount of radiation transmitted or reflected would not be expected to change significantly due to the change in the concentrator shape (Figure 3.13), the shape of the concentrator would affect geometrical concentration on the absorber tube. Reducing the optical efficiency of the concentrator to 95% of the predicted value decreases the thermal efficiency of the collector by ~6%, from 25.5% to 24%.

The numerical model is thus sensitive to the optical properties of the absorber tube and the shape of the concentrator. A combined effect of both of these factors within the considered range can decrease the thermal efficiency to as low as 21.8%. Further, better measurement techniques for the temperature difference would decrease the uncertainty in the measured efficiency significantly. A thermopile consisting of 8 thermocouples used for measuring temperature difference has an uncertainty of as low as $\pm 0.5\%$.

4.4 Conclusions

A prototype hybrid solar window (0.81m high x 0.78m long) was developed and tested for its thermal efficiency over a clear day in Minneapolis, MN. The CPC geometry

used for the prototype has a half-acceptance angle of 35º and was developed for a vertical window application in Chapter 3. The prototype was tested on a roof-top testing facility at the Department of Mechanical Engineering, University of Minnesota. A 40% ethylene glycol/water mixture was circulated through the collector at a mass flow rate of 0.011 kg/s-m^2 and the rise in the fluid temperature across the window were measured. The prototype had a thermal efficiency of 22% $\pm$ 6%. The large uncertainty is due to uncertainty in the measurement of temperature difference using thermocouples. This uncertainty can be reduced to $\pm$0.5% by using a thermopile.

Measured data was compared to the numerical thermal model discussed in Sections 2.3 and 3.4. The numerical model used measured data for the fluid inlet temperature, the ambient temperature, the mass flow rate, and the incident radiation as inputs. The numerical model predicts an efficiency of 25.5%. The deviation from the measured data can be explained by certain assumptions in the numerical model. The numerical model is sensitive to the optical properties of the absorber tube and the geometrical shape of the concentrator. The predicted efficiency can be as low as 21.8% within the considered range of uncertainties in both of these properties.

The daylighting parameters such as the visible transmittance, the solar heat gain coefficient and the U-factor have not been tested. These quantities for commercial systems are typically calculated through the numerical approach used in this thesis. Measurable daylighting parameters such as the illuminance and daylight factor distributions require the integration of the prototype window into an appropriately sized room. Alternatively the entire window assembly can be scaled down and tested in an

85

artificial sky facility. A separate daylighting experiment, coupled with the demonstrated thermal testing is essential to validate the hybrid window design as a whole.

4.5 Nomenclature

A	Area, m^2
c_p	Specific heat capacity at constant pressure, J/kgK
D	Tube diameter, m
G	Incident solar radiation, W/m^2
L	Length of CPC reflector, m
LST	Local solar time
$\dot{m}$	Mass flow rate, kg/s-m^2
n	Day of the year
Q_u	Total useful energy, kWh/m^2
$\dot{Q}_u$	Instantaneous useful energy rate per unit aperture area, W/m^2
$\dot{S}$	Instantaneous energy gain per unit aperture area, W/m^2
T	Temperature, K
t	Time
v_w	Wind velocity, m/s

Greek symbols

α	Absorptance of the absorber tube
β	Slope of the collector, deg
γ_s	Solar azimuth angle
δ	Latitude, deg

ε	Emittance
η	Efficiency
θ	Incidence angle, deg
θ_z	Solar zenith angle, deg
ρ_g	Ground reflectance
ϕ	Declination angle, deg
ω	Hour angle, deg

Subscripts

a	Absorber tube
b	Beam radiation
d	Diffuse radiation
fi	Fluid inlet
fo	Fluid outlet
h	Horizontal
m	Measured quantity
$\hat{n}$	Normal
th	Thermal
v	Vertical
∞	Ambient

Superscripts

PV	PV module
T	Thermal module

References

[1] SOLEC-Solar Energy Corporation, 'SOLKOTE Selective solar coating'
"http://www.solec.org/solkote-selective-solar-coating/solkote-technical-specifications/",
accessed March 1, 2012.
[2] Duffie, J. A. B., W. A., 2006, Solar Engineering of Thermal Processes, Third edition,
John Wiley and Sons, New York, NY.

Chapter 5

Conclusions

5.1 Summary and Conclusions

Two building integrated solar energy devices, a hybrid PV/T collector and a hybrid solar window, have been presented and analyzed. Both devices share two key elements: a wavelength selective film tuned to transmit in the visible spectrum and reflect in the infrared; and adaptable, non-tracking reflectors based on compound parabolic concentrators (CPCs).

A 3-D Monte Carlo Ray-Tracing (MCRT) model is implemented to predict the optical performance of the wavelength selective film and the compound parabolic concentrators. The model provides energetic and spectral information regarding the fractions of incident radiation intercepted at the absorber tube, and transmitted through the wavelength selective film to the PV module or daylit space, as a function of the direction of incident beam radiation, and for diffuse radiation. A detailed 1-D quasi-steady state thermal model predicts the annual thermal efficiency of the hybrid collector, coupling meteorological data with the general results from the MCRT. This analysis is common to both hybrid devices presented.

5.1.1 Hybrid PV/T

The hybrid PV/T concept employs compound parabolic concentrators to concentrate the energy reflected by the wavelength selective film onto absorber tubes to heat a fluid. The transmitted spectrum through the selective film is matched to the quantum efficiency curve of the thin film Cadmium Telluride module. This spectral

matching is quantified by a weighting factor W_λ obtained from the MCRT by comparing the transmitted spectrum to the quantum efficiency of the CdTe module. The application of the proposed hybrid concept to PV/T has some inherent disadvantages. For the evaluated geometries, the PV efficiency decreased from 8.8% without the selective film to ~5.4-6.2% for the hybrid assembly. Two factors are responsible for this decrease -

1. The wavelength selective films are spectrally matched to the PV module at normal incidence. At off-normal incidence the reflectance band of the film shifts to shorter wavelengths, effectively reducing the transmitted energy in the PV-matched band.

2. The absorber tubes shade the PV modules directly. Using a thin film PV CdTe module prevents current mismatch due to shading but the reduction in efficiency is substantial,

A comparison with an independent system of PV and thermal collectors having the same total aperture area and a size of the PV module that would yield the same electrical output as the hybrid system shows that the hybrid system produces 20% more total energy per unit area. In general, the PV/T device is not recommended for commercial production. However, it is possible to install the hybrid concentrators over existing PV arrays in order to obtain supplemental thermal energy at the cost of a reduction in the PV output.

The numerical MCRT and thermal model developed to characterize the hybrid PV/T are of value. This part of the work features an important parametric analysis to study the effect of the CPC geometry (acceptance angle, diameter, truncation) on the optical performance of the hybrid device. These results provided useful design insight while choosing CPC geometries for the hybrid solar window.

5.1.2 Hybrid Solar Window

The hybrid solar window concept is based on the same underlying goal as the hybrid PV/T, better utilization of the solar spectrum. The wavelength selective film is used in conjugation with the compound parabolic concentrators to transmit visible light for daylighting, while utilizing the near infrared to supplement thermal loads of the daylit space. Using the hybrid concept for daylighting proves much more promising than for PV/T. Since the ideal spectral band for daylighting (400-700 nm) is much narrower than that for the thin film PV, the wavelength selective film is just as effective at the full range of incidence angles accepted by the CPC.

The hybrid solar window is intended to interface with one of the most key components of the building envelope. With attention to the aesthetic and functional performance of fenestration systems, a novel design for an architecturally integrated solar window has been developed. A modified CPC design based on asymmetric truncation is proposed. The modified design allows the collector to be designed so as to functionally and aesthetically adapt to vertical windows, or skylights of any orientation. The fluid distribution system is integrated within the window frame and other elements of the building architecture (such as walls). The concentrators are designed to function as window blinds and can be operated at two different positions for passive thermal control of the daylit space.

The hybrid solar window was compared to commercial double glazed systems based on the visible transmittance, the solar heat gain coefficient and the U-factor. The hybrid solar window is as effective as most commercial glazing systems, with respect to effective daylighting (visible transmittance) and passive thermal control (solar heat gain

and U-factor). An exception to this is a double low-e coated glazing system, which has better heat insulation than the proposed window. Because the hybrid window can also be operated in a non-concentrating mode, it has the added flexibility of passive space heating/cooling depending on the weather or the personal comfort of the inhabitant. A prototype for the hybrid solar window was built and tested for thermal efficiency on a representative clear day. The measured data show good agreement with the numerical model.

The hybrid solar window has some drawbacks. The absorber tubes obstruct a clear view of the outside. This drawback can be easily mitigated by using the hybrid window for clerestories or skylights. A more important consideration is the integration and cost of the concomitant fluid distribution system. An integrated design effort during the architectural planning or design of a building would be required to make the commercialization of the hybrid solar window feasible.

5.2 Recommendations for future work

Extensive testing and validation of the prototype hybrid solar window to determine both the thermal and daylighting performance of the window is important. Presently, only the thermal efficiency of the prototype has been measured for a clear day with sizeable measurement uncertainty. The measurement uncertainty can be significantly reduced, from $\pm26\%$ to $\pm5\%$ or less by employing a thermopile for measuring the difference in temperatures at the fluid inlet and outlet. Further, the daylighting and passive thermal control characteristics proposed for the hybrid window need to be validated by on-site testing in a residential or commercial space.

A cost analysis of the hybrid window system is important to assess the market potential of the concept. Integration of the fluid distribution system and its implication on architectural design of the building needs to be studied.

Bibliography

Chapter 1

[1] DOE. Buildings Energy Data Book, Chapter 1 Buildings Sector. United States Department of Energy, 2011

Chapter 2

[1] Tripanagnostopoulos, Y., Nousia, T, Souliotis, M., and Yianoulis, P., 2002, "Hybrid Photovoltaic/Thermal Solar Systems," Solar Energy, 72(3), pp. 217-234.

[2] Tyagi, V. V., Kaushik, S. C., and Tyagi, S. K., 2012, "Advancement in Solar Photovoltaic/Thermal (PV/T) Hybrid Collector Technology," Renewable and Sustainable Energy Reviews, 16(3), pp. 1383-1398.

[3] Chow, T. T., 2010, "A Review on Photovoltaic/Thermal Hybrid Solar Technology," Applied Energy, 87(2), pp. 365-379.

[4] Anderson, T. N., Duke, M., Morrison, G. L., and Carson, J. K., 2009, "Performance of a Building Integrated Photovoltaic/Thermal (BIPVT) Solar Collector," Solar Energy, 83(4), pp. 445-455.

[5] Davidsson, H., Perers, B., and Karlsson, B., 2012, "System Analysis of a Multifunctional PV/T Hybrid Solar Window," Solar Energy, 86(3), pp. 903-910.

[6] Coventry, J. S., 2005, "Performance of a Concentrating Photovoltaic /Thermal Solar Collector," Solar Energy, 78(2), pp. 211-222.

[7] Li, M., Li, G. L., Ji, X., 2011, "The Performance Analysis of the Trough Concentrating Solar Photovoltaic/Thermal System," Energy Conversion and Management, 52(6) pp. 2378-2383

[8] Zhu, L., Boehm, R. F., Wang, Y., 2011, "Water Immersion Cooling of PV Cells in a High Concentration System," Solar Energy Materials and Solar Cells, 95(2) pp. 538-545.

[9] Zondag, H. A., de Vries, D. W., van Helden, W. G. J., van Zolingen, R. J. C., and van Steenhoven, A. A., 2003, "The Yield of Different Combined PV-Thermal Collector Designs," Solar Energy, 74(3), pp. 253-269.

[10] Fraisse, G., Ménézo, C., and Johannes, K., 2007, "Energy Performance of Water Hybrid PV/T Collectors Applied to Combisystems of Direct Solar Floor Type," Solar Energy, 81(11), pp. 1426-1438.

[11] Kim, J., and Kim, J., 2012, "The Experimental Performance of an Unglazed PV-ThermalCollector with a Fully Wetted Absorber," Energy Procedia, 30(0) pp. 144-151.

[12] Chow, T. T., Pei, G., Fong, K. F., 2009, "Energy and Exergy Analysis of Photovoltaic–Thermal Collector with and without Glass Cover," Applied Energy, 86(3) pp. 310-316.

[13] Dupeyrat, P., Ménézo, C., Wirth, H., 2011, "Improvement of PV Module Optical Properties for PV Thermal Hybrid Collector Application," Solar Energy Materials and Solar Cells, 95(8) pp. 2028-2036.

[14] Amori, K. E., and Taqi Al-Najjar, H. M., 2012, "Analysis of Thermal and Electrical Performance of a Hybrid (PV/T) Air Based Solar Collector for Iraq," Applied Energy, 98(0) pp. 384-395.

[15] Tonui, J. K., and Tripanagnostopoulos, Y., 2007, "Improved PV/T Solar Collectors

with Heat Extraction by Forced or Natural Air Circulation," Renewable Energy, 32(4), pp. 623-637.

[16] Hegazy, A. A., 2000, "Comparative Study of the Performances of Four Photovoltaic/Thermal Solar Air Collectors," Energy Conversion and Management, 41(8), pp. 861-881.

[17] Hj. Othman, M. Y., Yatim, B., Sopian, K., and Abu Bakar, M. N., 2005, "Performance Analysis of a Double-pass Photovoltaic/Thermal (PV/T) Solar Collector with CPC and Fins," Renewable Energy, 30(13), pp. 2005-2017.

[18] Assoa, Y. B., Menezo, C., Fraisse, G., 2007, "Study of a New Concept of Photovoltaic–Thermal Hybrid Collector," Solar Energy, 81(9) pp. 1132-1143.

[19] Imenes, A. G., and Mills, D. R., 2004, "Spectral Beam Splitting Technology for Increased Conversion Efficiency in Solar Concentrating Systems: a Review," Solar Energy Materials and Solar Cells, 84(1–4), pp. 19-69.

[20] Imenes, A. G., Buie, D., and McKenzie, D., 2006, "The Design of Broadband, Wide-Angle Interference Filters for Solar Concentrating Systems," Solar Energy Materials and Solar Cells, 90(11), pp. 1579-1606.

[21] Segal, A., Epstein, M., and Yogev, A., 2004, "Hybrid Concentrated Photovoltaic and Thermal Power Conversion at Different Spectral Bands," Solar Energy, 76(5), pp. 591-601.

[22] Jiang, S., Hu, P., Mo, S., and Chen, Z., 2010, "Optical Modeling for a Two-Stage Parabolic Trough Concentrating Photovoltaic /Thermal System using Spectral Beam Splitting Technology," Solar Energy Materials and Solar Cells, 94(10), pp. 1686-1696.

[23] Izumi, H., 2000, "Hybrid Solar Collector for Generating Electricity and Heat by Separating Solar Rays into Long Wavelength and Short Wavelength," U.S. 6057504.

[24] Rabl, A., 1976, "Optical and Thermal Properties of Compound Parabolic Concentrators," Solar Energy, 18(6), pp. 497-511.

[25] Carvalho, M. J., Collares-Pereira, M., Gordon, J. M., and Rabl, A., 1985, "Truncation of CPC Solar Collectors and Its Effect on Energy Collection," Solar Energy, 35(5), pp. 393-399.

[26] Weber, M. F., Stover, C. A., Gilbert, L. R., 2000, "Giant Birefringent Optics in Multilayer Polymer Mirrors," Science, 287(5462) pp. 2451-2456.

[27] Nann, S., and Emery, K., 1992, "Spectral Effects on PV-Device Rating," Solar Energy Materials and Solar Cells, 27(3), pp. 189-216.

[28] Koishiyev, G. T., 2010, "Analysis of Impact of Non-Uniformities on Thin-Film Solar Cells and Modules with 2-D Simulations,"Ph.D Thesis, Colorado State University.

[29] Howell, J. R., 1998, "The Monte Carlo Method in Radiative Heat Transfer," Journal of Heat Transfer, 120(3), pp. 547-560.

[30] Modest, M. F., 2003, Radiative Heat Transfer, Second Edition, Academic Press, pp. 653

[31] Rabl, A., 1976, "Solar Concentrators with Maximal Concentration for Cylindrical Absorbers," Appl. Opt., 15(7), pp. 1871-1873.

[32] Duffie, J. A., Beckman, W. A., 2006, Solar Engineering of Thermal Processes, Third edition, John Wiley and Sons, New York, NY.

[33] Krueger, K. R., Davidson, J. H., and Lipiński, W., 2011, "Design of a New 45 kWe High-Flux Solar Simulator for High-Temperature Solar Thermal and Thermochemical

Research," Journal of Solar Energy Engineering, Transactions of the ASME, 133(1).

[34] Renewable Resource Data Center, National Renewable Energy Laboratory, 2012, http://rredc.nrel.gov/solar/old_data/nsrdb/1961-1990/tmy2/

[35] Kuehn, T. H., Goldstein, R. J., 1976, "Correlating Equation for Natural Heat Transfer between Horizontal Circular Cylinders," Int. J. Heat Mass Transfer, Vol. 19, pp. 1127-1134

[36] Prapas, D. E., Norton, B., and Probert, S. D., 1987, "Thermal Design of Compound Parabolic Concentrating Solar-Energy Collectors," Journal of Solar Energy Engineering,109(2), pp.161-168.

[37] Churchill, S. W., and Chu, H. H. S., 1975, "Correlating Equations for Laminar and Turbulent Free Convection from a Vertical Plate," International Journal of Heat and Mass Transfer, 18(11) pp. 1323-1329.

[38] Gnielinski, V., 1976, "New Equations for Heat and Mass Transfer in Turbulent Pipe and Channel Flow," Int. Chem. Engng., vol. 16, pp. 359-368.

[39] Mattei, M., Notton, G., Cristofari, C., Muselli, M., and Poggi, P., 2006, "Calculation of the Polycrystalline PV Module Temperature Using a Simple Method of Energy Balance," Renewable Energy, 31(4), pp. 553-567.

[40] Vigil-Galán, O., Arias-Carbajal, A., Mendoza-Pérez, R., Santana, G., Sastré-Hernández, J., Contreras-Puente, G., Morales-Acevedo, A., and Tufiño-Velázquez, M., 2006, "Spectral Response of CdS/CdTe Solar Cells Obtained with Different S/Cd Ratios for the CdS Chemical Bath," Solar Energy Materials and Solar Cells, 90(15), pp. 2221-2227.

[41] AlBusairi, H. A., Muller, H. A., "Performance Evaluation of CdTe PV Modules under Natural Outdoor Conditions in Kuwait," Proc. 25th European Solar Energy Conference and Exhibition/5th World Conference on Photovoltaic Energy Conversion, pp. 3468-3470.

[42] King, D. L., Boyson, W. E., and Kratochvill, J. A., Sandia National Laboratories, 2004, "Photovoltaic Array Performance Model."

[43] Solar Rating and Certification Corporation, "https:// secure.solar-rating.org/.", accessed March 1, 2011.

Chapter 3

Alvarez, R., González, J.C., Espinós, J.P., González-Elipe, A.R., Cueva, A., Villuendas, F., 2013. Growth of silver on ZnO and SnO2 thin films intended for low emissivity applications. J. Appl. Surf. Sci. 268, 507-515.

Buratti, C., Moretti, E., 2012. Glazing systems with silica aerogel for energy savings in buildings. J. Appl. Energy 98, 396-403.

Chow, S.K.H., Li, D.H.W., Lee, E.W.M., Lam, J.C., 2013, Analysis and prediction of daylighting and energy performance in atrium spaces using daylight-linked lighting controls. J. Appl. Energy.

Chow, T., Li, C., Lin, Z., 2011. Thermal characteristics of water-flow double-pane window. Int. J. Therm. Sci. 50, 140-148.

Chow, T., Li, C., Lin, Z., 2010. Innovative solar windows for cooling-demand climate. Sol. Energ. Mat. Sol. C. 94, 212-220.

Davidsson, H., Perers, B., Karlsson, B., 2010. Performance of a multifunctional PV/T hybrid solar window. Sol. Energy 84, 365-372.

De Rosa, A., Ferraro, V., Kaliakatsos, D., Marinelli, V., 2010. Calculating indoor natural illuminance in overcast sky conditions. Appl. Energy 87, 806-813.

Du, J., Sharples, S., 2011. The variation of daylight levels across atrium walls: Reflectance distribution and well geometry effects under overcast sky conditions. Sol. Energy 85, 2085-2100.

Duffie, J.A., Beckman, W.A., 2006. Solar Engineering of Thermal Processes, Third Edition. John Wiley and Sons, New York.

Gardiner, D.J., Morris, S.M., Coles, H.J., 2009. High-efficiency multistable switchable glazing using smectic A liquid crystals. Sol. Energ. Mat. Sol. C. 93, 301-306.

Gochenour, S.J., Andersen, M., 2009. Circadian Effects of Daylighting in a Residential Environment. In Proceedings LuxEuropa, Istanbul.

Granqvist, C.G., Green, S., Niklasson, G.A., Mlyuka, N.R., von Kraemer, S., Georen, P., 2010. Advances in chromogenic materials and devices. Thin Solid Films 518, 3046-3053.

Howell, J.R., 1998. The Monte Carlo Method in Radiative Heat Transfer. J. Heat Transfer 120(3), 547-560.

Kakaç, S., Shah, R., Aung, W., 1987. Handbook of Single-Phase Convective Heat Transfer. John Wiley and Sons, New York, NY.

Kim, G., Kim, J.T., 2010. Healthy-daylighting design for the living environment in apartments in Korea. Build. Environ. 45, 287-294.

Li, D.H.W., Lam, T.N.T., Chan, W.W.H., Mak, A.H.L., 2009. Energy and cost analysis of semi-transparent photovoltaic in office buildings. Appl. Energy 86, 722-729.

Li, D.H.W., Lam, T.N.T., Wong, S.L., 2006. Lighting and energy performance for an office using high frequency dimming controls. Energy. Convers. Manage. 47, 1133-1145.

Martin-Palma, R.J., 2009. Commentary: Spectrally selective coatings on glass: solar-control and low-emissivity coatings. J. Nanophoton. 3, 030305.

Mlyuka, N.R., Niklasson, G.A., Granqvist, C.G., 2009. Thermochromic multilayer films of VO2 and TiO2 with enhanced transmittance. Sol. Energ. Mat. Sol. C. 93, 1685-1687.

Modest, M.F., 2003. Radiative Heat Transfer, Second Edition. Academic Press.

Mohelnikova, J., 2009. Materials for reflective coatings of window glass applications. Constr. Build. Mater. 23, 1993-1998.

NFRC 100-2010: Procedure for Determining Fenestration Product U-factors, 2010. National Fenestration Rating Council.

NFRC 200-2010: Procedure for Determining Fenestration Product Solar Heat Gain Coefficient and Visible Transmittance at Normal Incidence, 2010. National Fenestration Rating Council.

Page, J., Scartezzini, J.L., Kaempf, J., Morel, N., 2007. On-site performance of electrochromic glazings coupled to an anidolic daylighting system. Sol. Energy 81, 1166-1179.

Piccolo, A., Pennisi, A., Simone, F., 2009. Daylighting performance of an electrochromic window in a small scale test-cell. Sol. Energy 83, 832-844.

Plympton, P., Conway, S., Epstein, K., 2000. Daylighting in Schools: Improving Student Performance and Health at a Price Schools can Afford. American Solar Energy Society Conference, Madison.

Rabl, A., 1976. Optical and thermal properties of compound parabolic concentrators. Sol. Energy 18, 497-511.

ISO 15099:2003 Thermal performance of windows, doors and shading devices - Detailed calculations, 2003. International Organization for Standardization.

Ulavi, T.U., Davidson, J.H., Hebrink, T., 2013. Analysis of a Hybrid PV/T Concept Based on Wavelength Selective Films. ASME Energy Sustainability, Minneapolis, MN

Vandewalle, G., Balteau, E., Phillips, C., Degueldre, C., Moreau, V., Sterpenich, V., Albouy, G., Darsaud, A., Desseilles, M., Dang-Vu, T.T., Peigneux, P., Luxen, A., Dijk, D.J., Maquet, P., 2006. Daytime light exposure dynamically enhances brain responses. Curr. Biol. 16, 1616-1621.

Weber, M.F., Stover, C.A., Gilbert, L.R., Nevitt, T.J., Ouderkirk, A.J., 2000. Giant Birefringent Optics in Multilayer Polymer Mirrors. Science 287, 2451-2456.

Wright, J.L., 1996. A Correlation to Quantify Convective Heat Transfer Between Vertical Window Glazings. ASHRAE Trans. 102, Pt. 1, 940-946.

Xu, X., Gibbons, T.H., Cortie, M.B., 2006. Spectrally-selective gold nanorod coatings for window glass. Gold Bulletin 39, 156-165.

Web based references

[1] Colour and Vision Research Laboratory, CIE Photopic Luminosity function (http://www.cvrl.org/lumindex.htm), last accessed 08/20/2012

[2] Lawrence Berkeley Research Laboratory, RADIANCE (http://radsite.lbl.gov/radiance/)

[3] Integrated Environmental Solutions, IES VE Pro (http://www.iesve.com/software/ve-pro)

[4] AGC, 'Solite'(http://www.agc-solar.com/agc-solar-products/patterned-glass/solite.html), last accessed 04/20/2013

[5] Lawrence Berkeley Research Laboratory, WINDOW (http://windows.lbl.gov/software/window/window.html), last accessed 04/20/2013

Chapter 4

[1] SOLEC-Solar Energy Corporation, 'SOLKOTE Selective solar coating' "http://www.solec.org/solkote-selective-solar-coating/solkote-technical-specifications/", accessed March 1, 2012.

[2] Duffie, J. A. B., W. A., 2006, Solar Engineering of Thermal Processes, Third edition, John Wiley and Sons, New York, NY.

Appendix A

CPC Geometry

The compound parabolic concentrator with a tubular absorber was developed by Ari Rabl [1]. The concentrator is based on non-imaging optics and is designed to be a perfect concentrator within the acceptance angle. In terms of parameters (ρ, φ) shown in Fig. A.1, the x and y coordinates of the CPC are described by Eqs. (A.1)-(A.3). The concentrator is simply extruded in the z direction.

$$x_{m,\varphi} = \pm \left(\frac{D}{2} \sin \varphi - \rho \cos \varphi \right) \tag{A.1}$$

$$y_{m,\varphi} = -\frac{D}{2} \cos \varphi - \rho \sin \varphi \tag{A.2}$$

$$0 \leq z_{m,\varphi} \leq L \tag{A.3}$$

where

$$\rho = \frac{D}{2} \cdot \varphi, \qquad\qquad |\varphi| \leq \theta_c + \frac{\pi}{2}$$

$$\rho = \frac{D}{2} \cdot \frac{\varphi + \theta_c + \pi/2 - \cos(\varphi - \theta_c)}{1 + \sin(\varphi - \theta_c)}, \qquad \theta_c + \frac{\pi}{2} \leq |\varphi| \leq \frac{3\pi}{2} - \theta_c$$
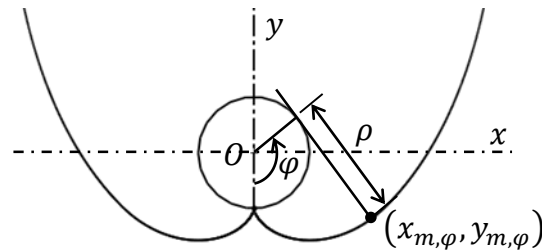
Fig. A.1 CPC coordinates in terms of parameters ρ, φ

References

[1] Rabl, A., 1976, "Solar Concentrators with Maximal Concentration for Cylindrical Absorbers," Appl. Opt., 15(7), pp. 1871-1873.

Appendix B

Additional notes on the MCRT

B.1 Convergence Criteria

For the Monte Carlo simulations, separate cases are run for beam and diffuse radiation. For beam radiation, the direction of incident radiation is fixed for a particular simulated case. For diffuse radiation, the direction is randomly assigned based on derived relations for diffuse emission from an isotropic, isothermal surface. The accuracy of the numerical results depends on the number of rays required to stochastically capture the geometrical and optical interactions within the cavity.

Since the launched rays are uniformly distributed over the CPC aperture, the minimum number of rays for convergence for beam and diffuse radiation should be based on the geometry with the maximum aperture area, $W \times L$. From among the considered geometries, the geometry with $\theta_c = 25°$, $D = 0.03$m and $L = 2$m has the largest width $W = 0.2$m considered for the hybrid PV/T application is the largest. Fig. B.1 (a) shows simulations varying $N_{i,b}$ for the CPC geometry for beam radiation normal to the CPC cover. The abscissa denotes the number of rays used in the Monte Carlo simulation and the ordinate represents the fractions of incident radiation reaching the absorber tube (red) and transmitted through the concentrator (blue). For $N_{i,b} \geq 10^5$, the quantities are constant up to 3 decimal points. Fig. B.1 (b) shows the case for diffuse radiation. The fractions of energy reaching the absorber tube and transmitted through the concentrators take longer for convergence up to 3 decimal points. $N_{i,b}$ and $N_{i,d}$ are thus selected as 10^5 and 10^6 respectively.

It is also important that the transmitted spectrum achieves convergence as well. Consider Fig. B.2 which plots the visible transmittance for a diffuse sky for the same concentrator geometry as a function of the number of rays $N_{i,d}$. Convergence up to two decimal points is obtained for $N_{i,d} \geq 10^5$. Hence, the number of rays chosen for beam and diffuse radiation are enough for convergence, both energetically and spectrally.
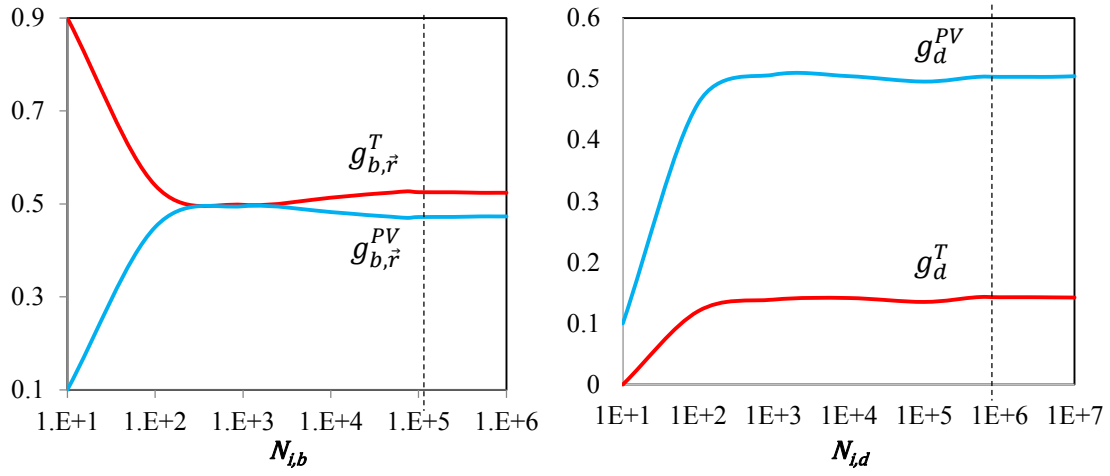
Fig. B.1 Convergence of numerical results for (a) beam radiation (normal to CPC axis) and (b) diffuse radiation as a function of launched rays for $\theta_c = 25°$, $D = 0.03$m
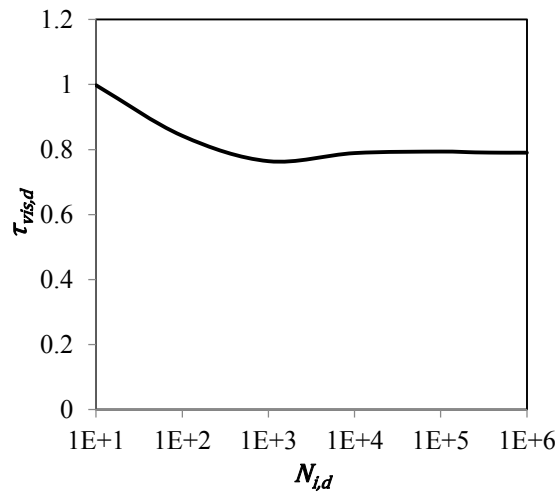
Fig. B.2 Convergence of numerical results for diffuse visible transmittance as a function of number of launched rays for $\theta_c = 25°$, $D = 0.03$m

B.2 Ray-tracing algorithm

Ray-tracing module

Update θ_{xy} and θ_{yz}

Update θ_{xy} and θ_{yz}

Equations of ray in xy and yz planes from θ_{xy} and θ_{yz}
$$y = m_{xy}x + c_{xy}$$
$$y = m_{yz}z + c_{yz}$$

Solve Ray ∩ Absorber to obtain (x_a, y_a, z_a)

$(x_a, y_a, z_a) \in$ Absorber — Y → Stop

N

Solve Ray ∩ Cover in xy and yz plane to obtain (x_c, y_c, z_c)

$(x_c, y_c, z_c) \in$ Cover — Y → Generate $R_c(0,1)$ Calculate ρ_c based on incidence angle

N

Solve Ray ∩ CPC in xy and yz plane to obtain (x_m, y_m, z_m)

$R_c < \rho_c$ — Y / N → Stop

Generate $R_m(0,1)$ Calculate ρ_m based on incidence angle and wavelength

$(x_m, y_m, z_m) \in$ CPC

$R_m < \rho_m$ — Y / N → Stop

Fig. B.3 Monte Carlo Ray-Tracing algorithm, ray-tracing module

102

Fig. B.4 Monte Carlo Ray-Tracing algorithm (Primary loop)

B.3 Implementation of the Specular Error

On account of the surface roughness of the manufactured CPC, the reflection from the CPC surface will not be perfectly specular. A specular error was defined in the model to account for the surface roughness. Literature suggests that the angular errors due to surface roughness have a normal distribution [1, 2].

In the present case, the specular error is defined as the standard deviation of a distribution of angular errors θ_s between the normal of a perfectly smooth surface, $\hat{n}$, and the normal of a real surface, $\hat{n}'$ (Fig. B.5). θ_s is thus a normally distributed variable having a mean $\mu = 0$ and a standard deviation σ_s specified as the specular error. θ_s can be find by using the inverse cumulative distribution function (or quantile function) for a normally distributed variable having a mean of 0 and a standard deviation of 1.

$$\theta_s = \sigma_s\sqrt{2}erf^{-1}(2R_{err,s} - 1) \tag{B.1}$$

where $erf^{-1}()$ is the inverse error function and $R_{err,s}$ is a generated random number uniformly distributed in (0,1). It should be noted that θ_s is normalized to ensure values between 0 and $\pi/2$ only. To define the deviation from the surface normal, the surface azimuth is required which can take any value from 0 to 2π.

$$\psi_s = 2\pi R_{err,\psi} \tag{B.2}$$
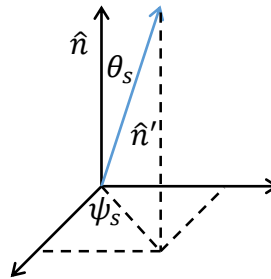
Fig. B.5 Modified surface normal to account for specular error

B.4 Component angles θ_{xy} and θ_{yz} of a three dimensional ray

The ray tracing procedure is carried out separately in the xy and yz planes. However, incident ray direction from the sun, or from a diffuse isotropic surface (in case of diffuse radiation) is specified by the polar and azimuth angles. Further, the incidence angle at the film interface to calculate the film reflectance or to account for the specular error is also required in 3 dimensions. Once a position is associated with the origin or destination of the ray, the polar and azimuth angles can be converted into the components in the xy and yz planes by considering a local coordinate system (Fig B.6). The y axis is along the surface normal at the point and z is along the length of the concentrator.

$$\theta_{xy} = \tan^{-1}(\tan\theta \sin\psi) \tag{B.3}$$

$$\theta_{yz} = \tan^{-1}(\tan\theta \cos\psi) \tag{B.4}$$

A reverse procedure is used to convert the component angles to the polar and zenith angles according to a global coordinate system.
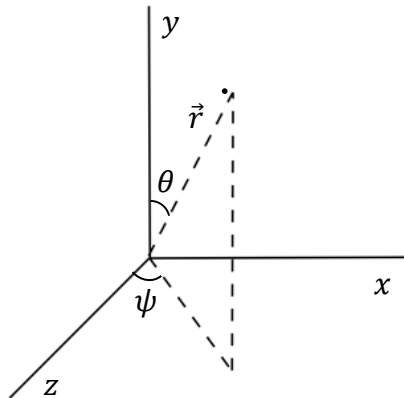
Fig. B.6 The polar and azimuth angles for a ray in the local coordinate system

Appendix C

Results from MCRT

C.1 Hybrid PV/T

Figs. C.1-C.7 → Figs. 2.8 and 2.10
Figs. C.8-C.21 → Fig. 2.10
Figs. C22-C.30 → Fig. 2.9
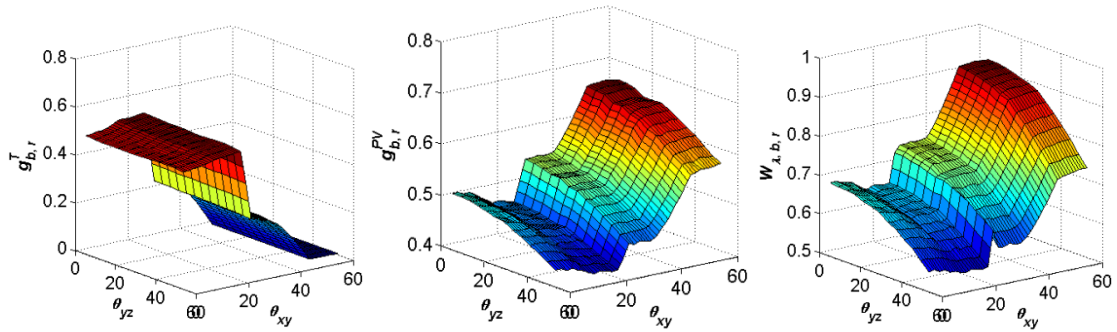

Fig. C.1 MCRT results for hybrid PV/T: $\theta_c = 25^o$, $D = 0.03$m
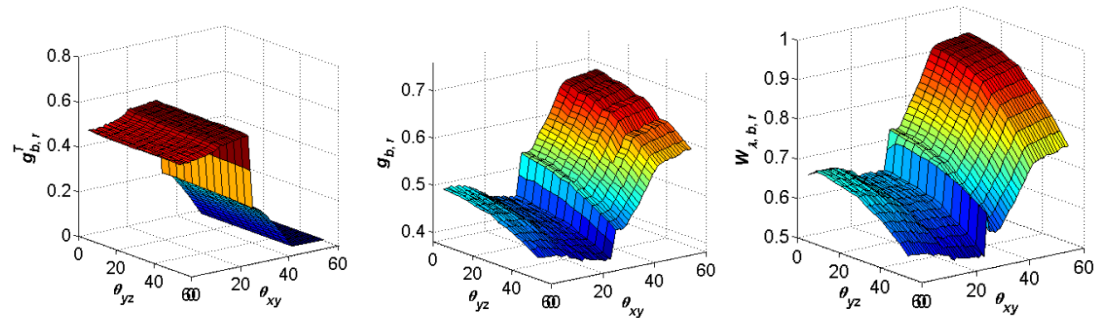
Fig. C.2 MCRT results for hybrid PV/T: $\theta_c = 30^o$, $D = 0.03$m
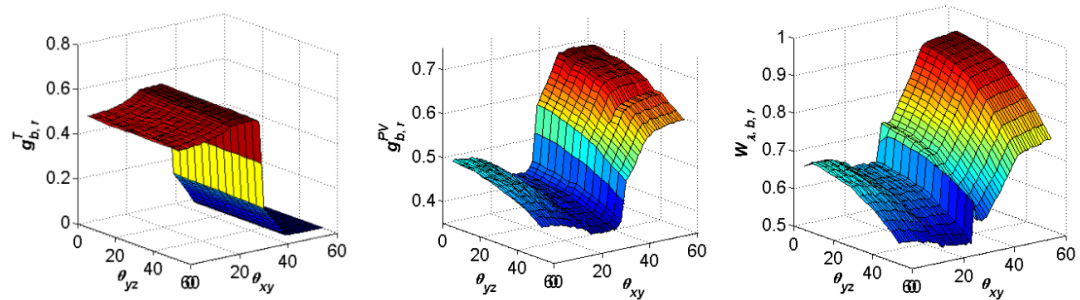
Fig. C.3 MCRT results for hybrid PV/T: $\theta_c = 35^o$, $D = 0.03$m
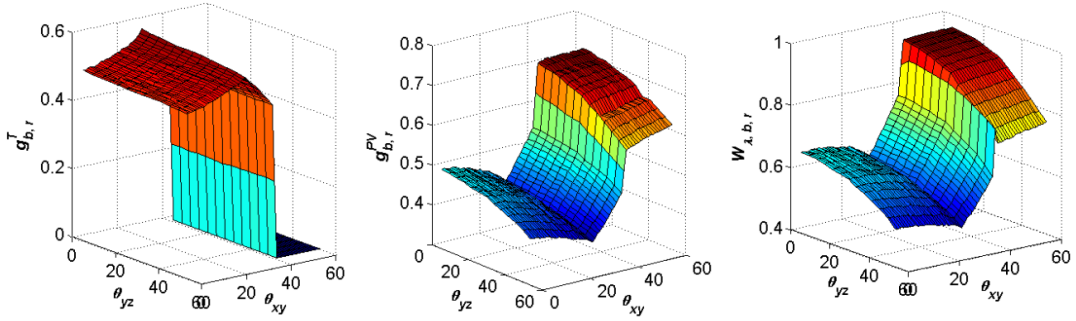
Fig. C.4 MCRT results for hybrid PV/T: $\theta_c = 40^\circ$, $D = 0.03$m
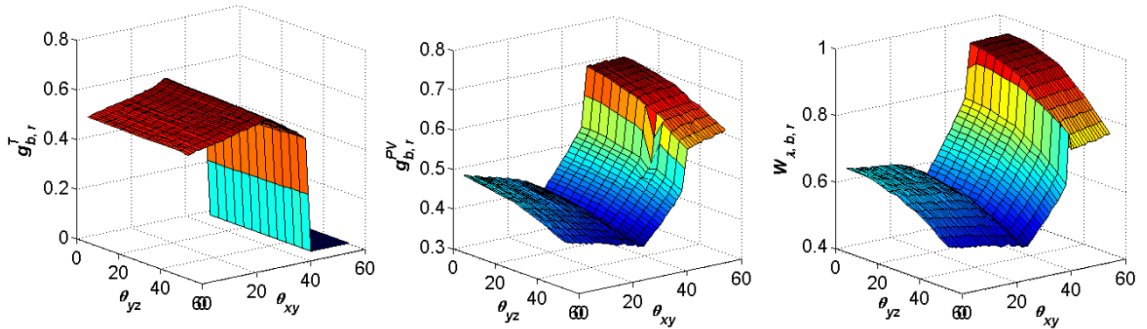
Fig. C.5 MCRT results for hybrid PV/T: $\theta_c = 45^\circ$, $D = 0.03$m
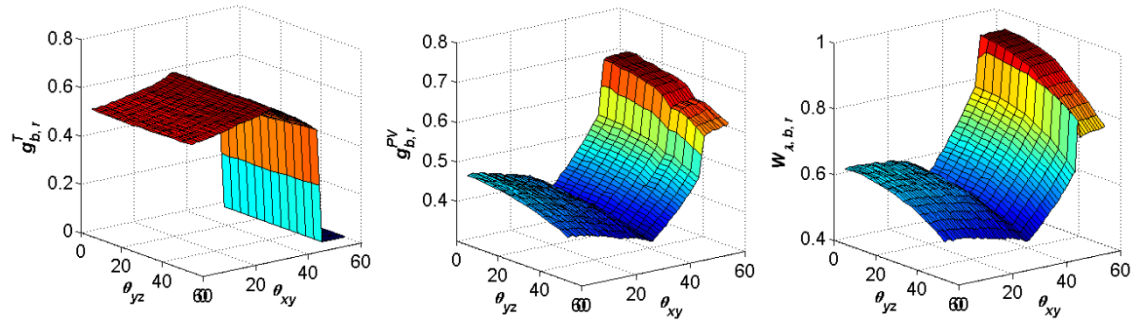
Fig. C.6 MCRT results for hybrid PV/T: $\theta_c = 50^\circ$, $D = 0.03$m
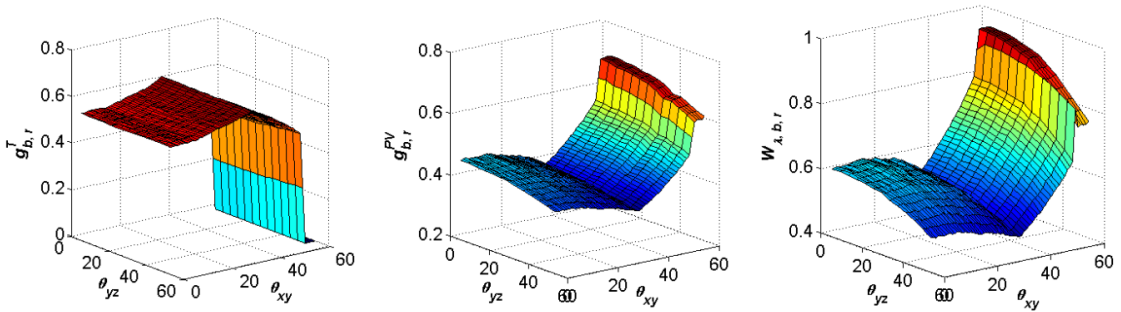
Fig. C.7 MCRT results for hybrid PV/T: $\theta_c = 55^\circ$, $D = 0.03$m

107
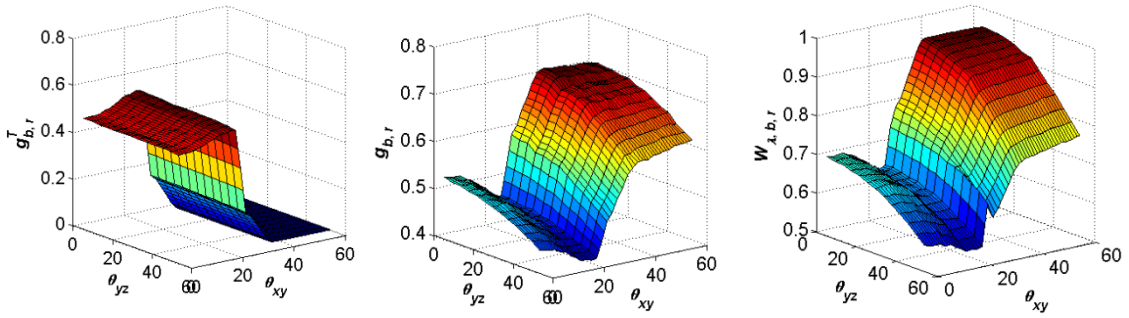
Fig. C.8 MCRT results for hybrid PV/T: $\theta_c = 25^\circ$, $D = 0.02$m
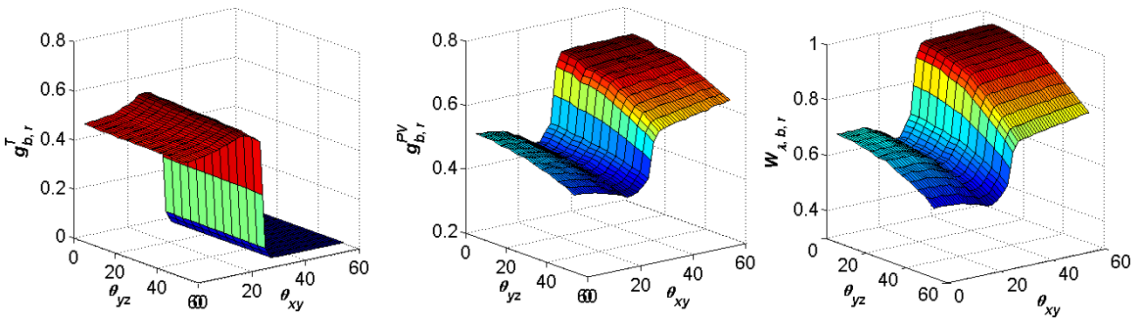
Fig. C.9 MCRT results for hybrid PV/T: $\theta_c = 30^\circ$, $D = 0.02$m
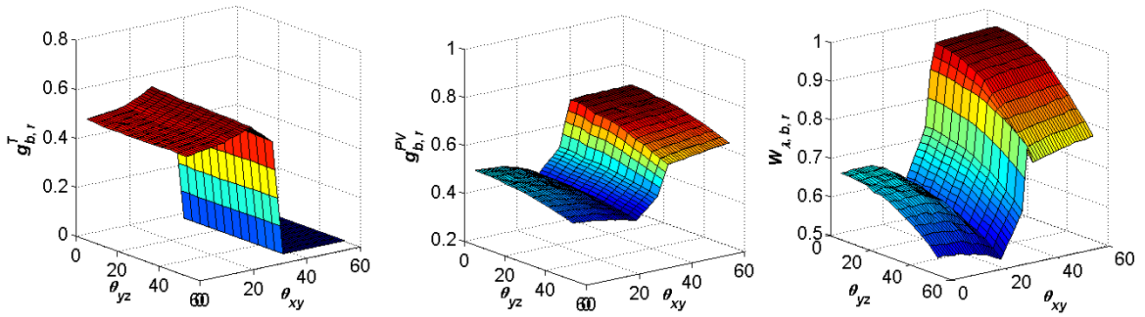
Fig. C.10 MCRT results for hybrid PV/T: $\theta_c = 35^\circ$, $D = 0.02$m
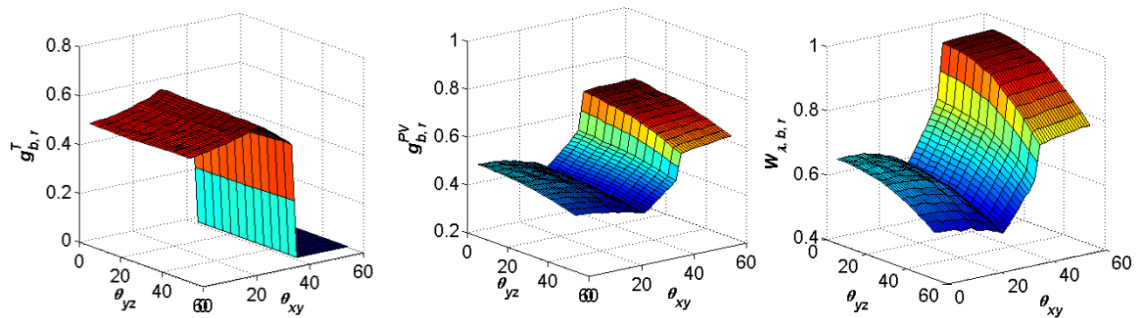

Fig. C.11 MCRT results for hybrid PV/T: $\theta_c = 40^\circ$, $D = 0.02$m
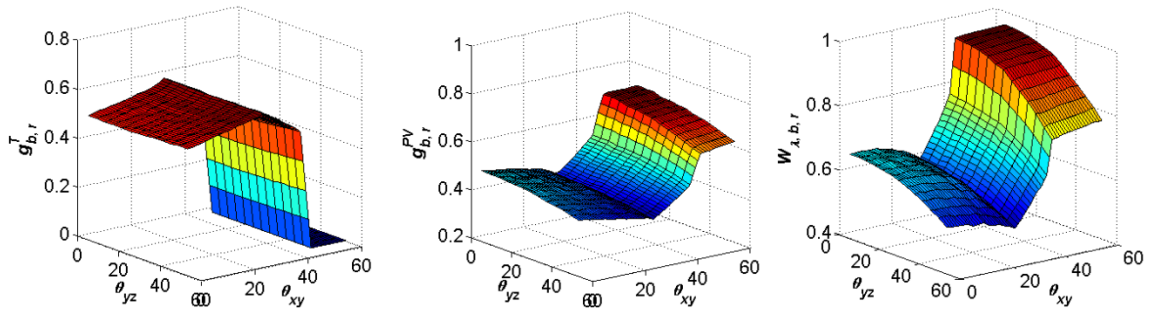
Fig. C.12 MCRT results for hybrid PV/T: $\theta_c = 45^o$, $D = 0.02$m
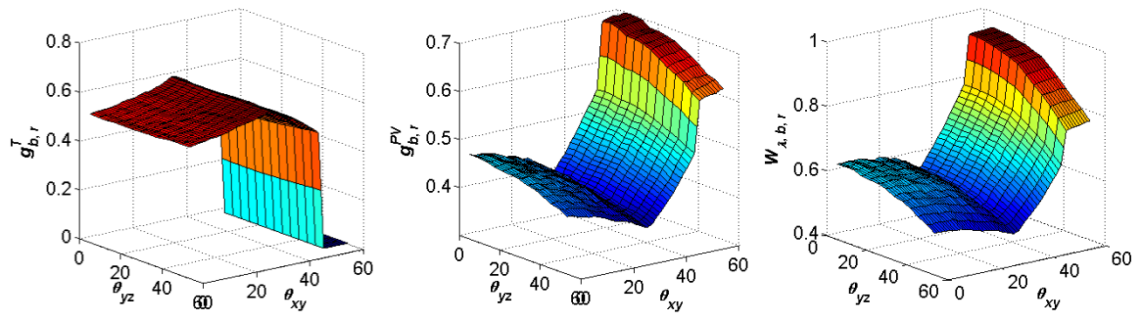
Fig. C.13 MCRT results for hybrid PV/T: $\theta_c = 50^o$, $D = 0.02$m
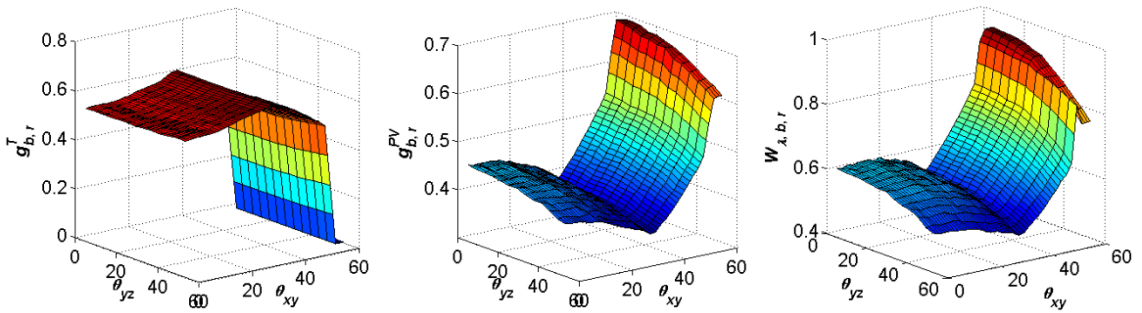

Fig. C.14 MCRT results for hybrid PV/T: $\theta_c = 55^o$, $D = 0.02$m
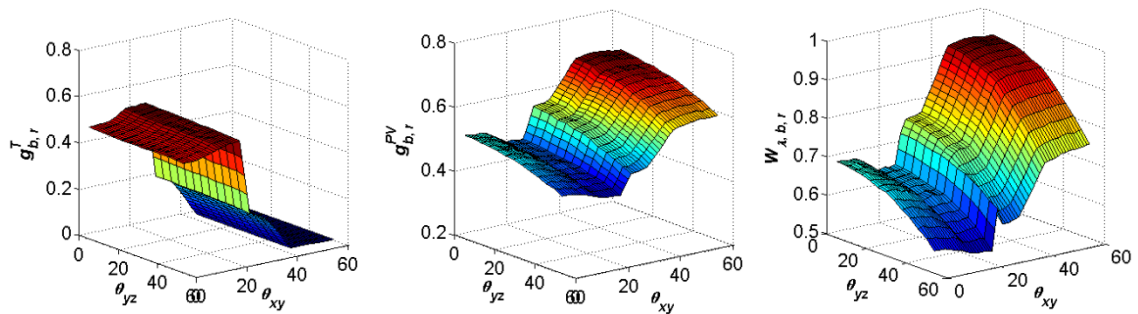
Fig. C.15 MCRT results for hybrid PV/T: $\theta_c = 25^o$, $D = 0.025$m

109
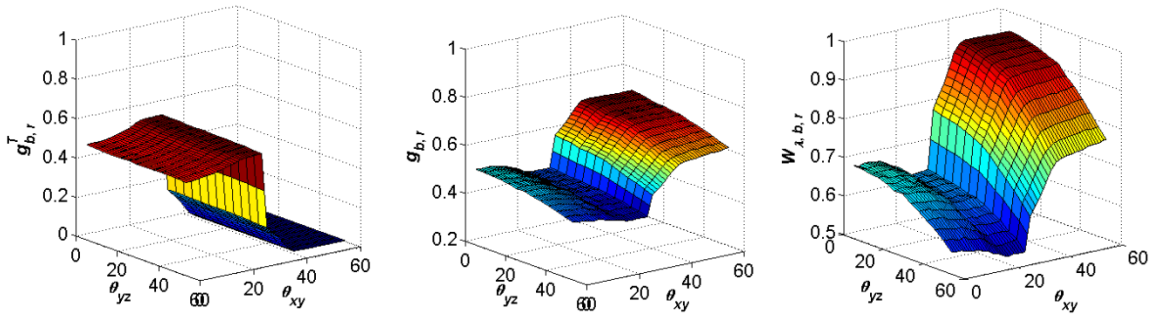
Fig. C.16 MCRT results for hybrid PV/T: $\theta_c = 30^o$, $D = 0.025$m
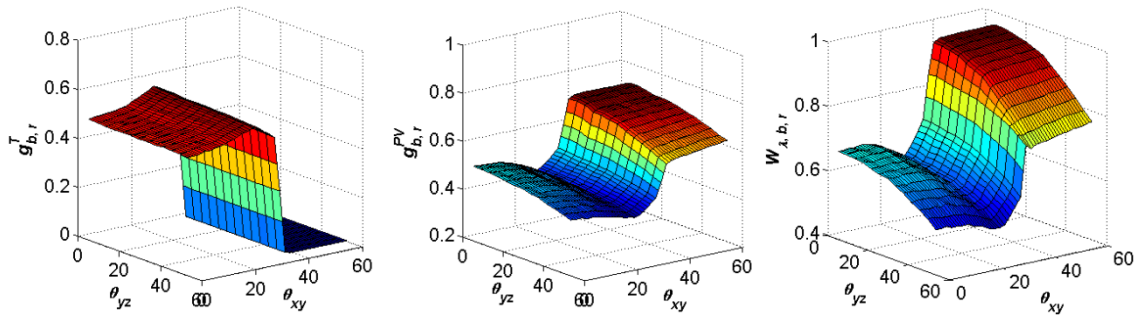
Fig. C.17 MCRT results for hybrid PV/T: $\theta_c = 35^o$, $D = 0.025$m
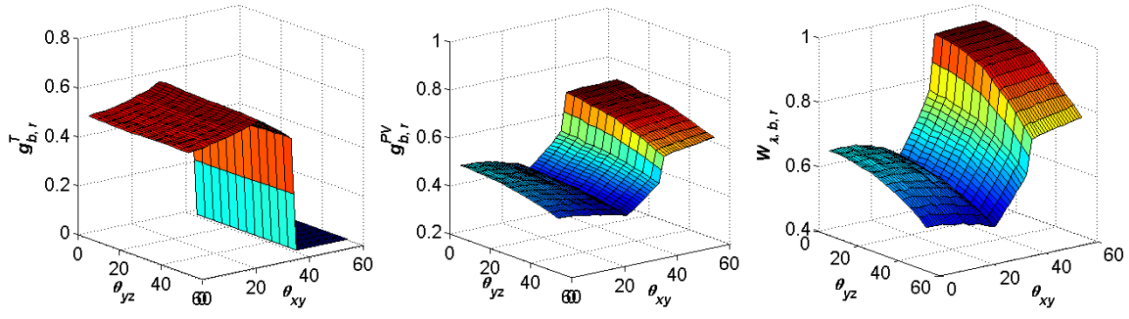
Fig. C.18 MCRT results for hybrid PV/T: $\theta_c = 40^o$, $D = 0.025$m
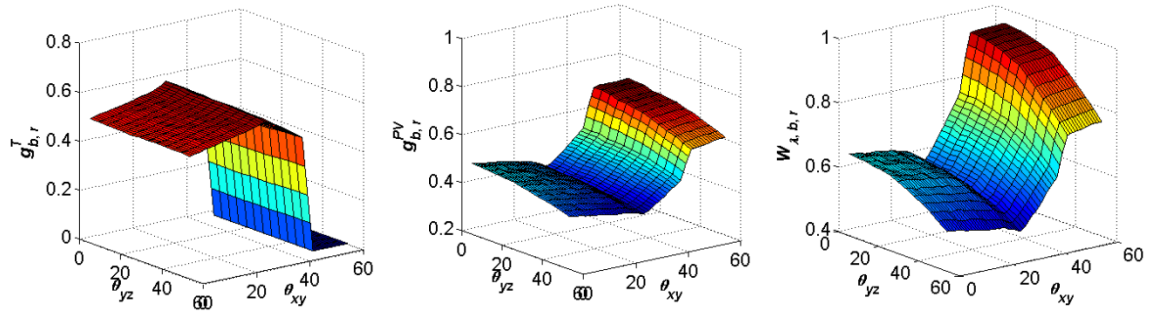
Fig. C.19 MCRT results for hybrid PV/T: $\theta_c = 45^o$, $D = 0.025$m

110
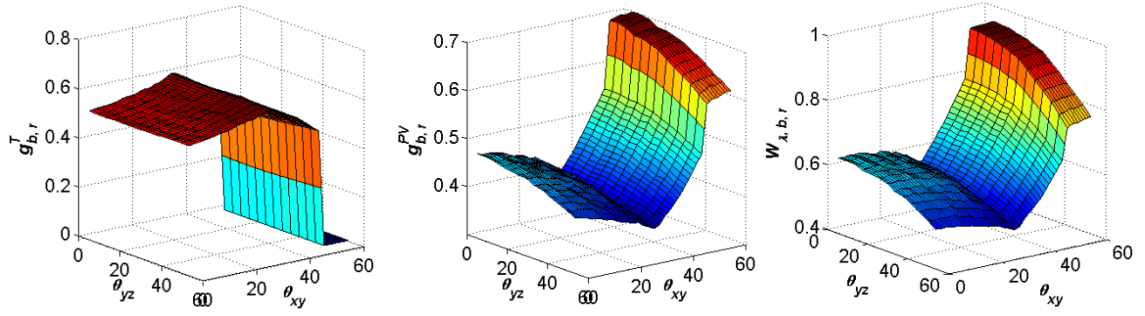
Fig. C.20 MCRT results for hybrid PV/T: $\theta_c = 50^\circ$, $D = 0.025$m
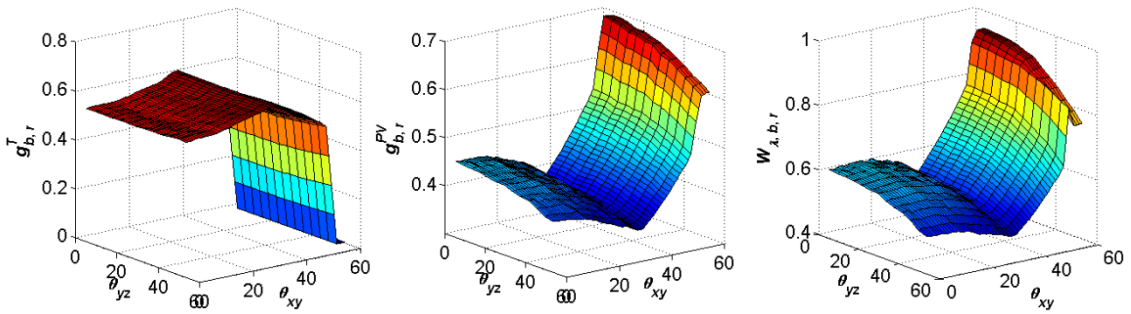
Fig. C.21 MCRT results for hybrid PV/T: $\theta_c = 55^\circ$, $D = 0.025$m
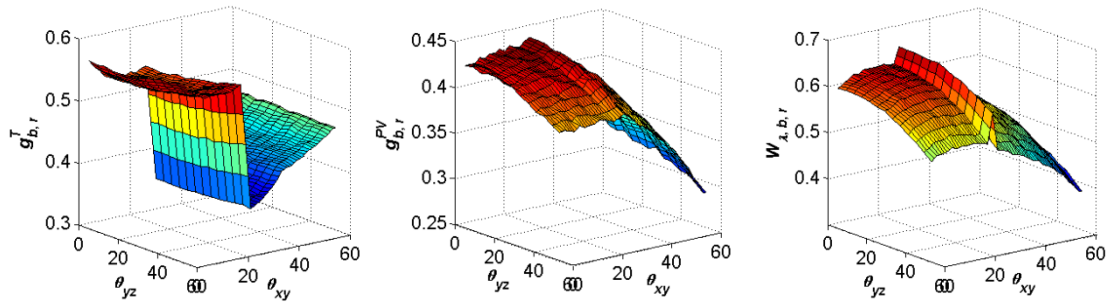
Fig. C.22 MCRT results for hybrid PV/T: $\theta_c = 25^\circ$, $D = 0.03$m, $C_e = 1.4$
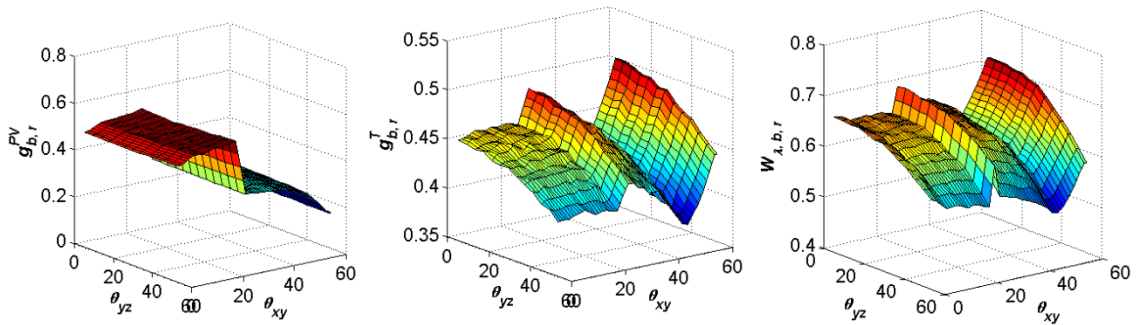
Fig. C.23 MCRT results for hybrid PV/T: $\theta_c = 25^\circ$, $D = 0.03$m, , $C_e = 1.7$
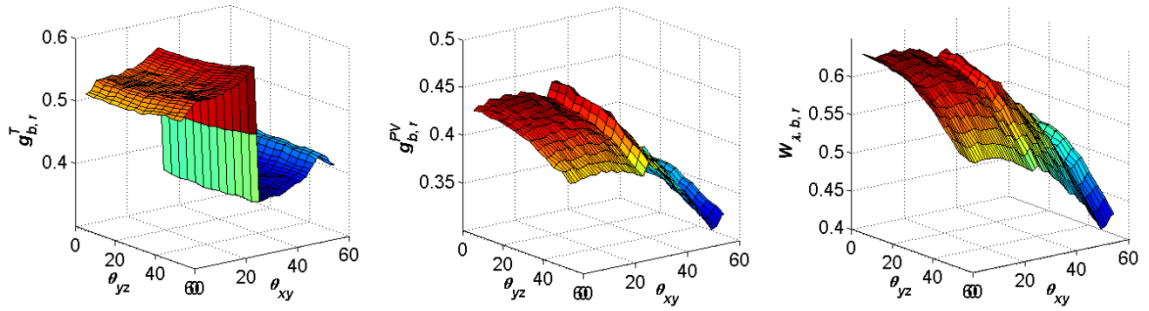
Fig. C.24 MCRT results for hybrid PV/T: $\theta_c = 30^\circ$, $D = 0.03$m, $C_e = 1.4$
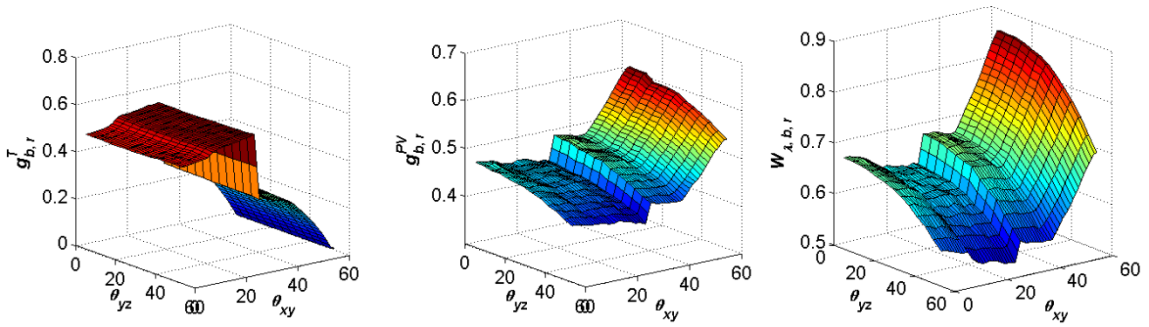
Fig. C.25 MCRT results for hybrid PV/T: $\theta_c = 30^\circ$, $D = 0.03$m, $C_e = 1.7$
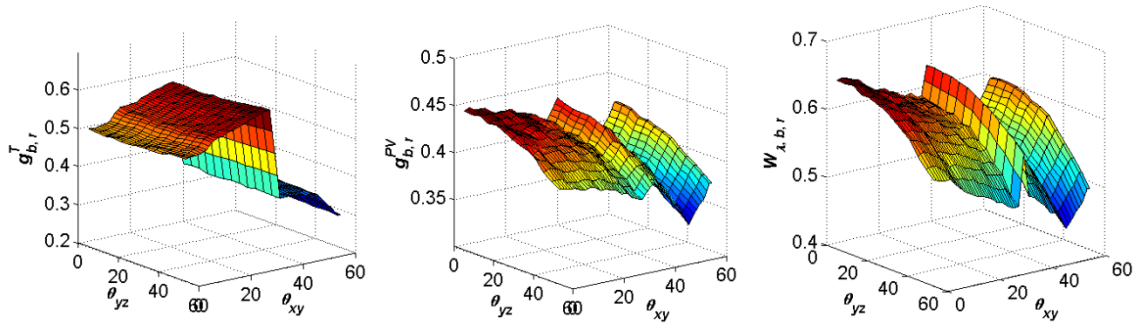
Fig. C.26 MCRT results for hybrid PV/T: $\theta_c = 35^\circ$, $D = 0.03$m, $C_e = 1.4$
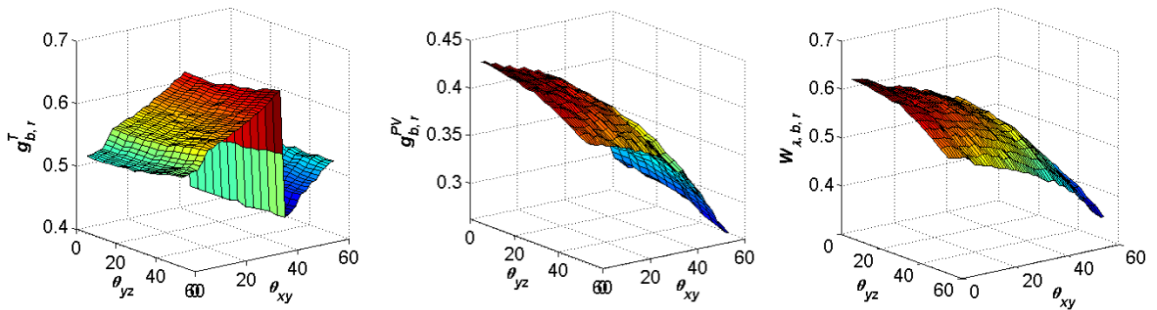
Fig. C.27 MCRT results for hybrid PV/T: $\theta_c = 40^\circ$, $D = 0.03$m, $C_e = 1.2$

112
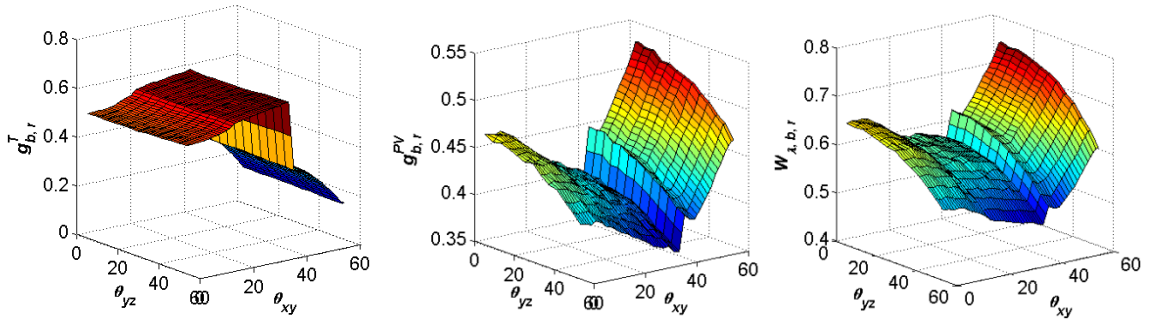
Fig. C.28 MCRT results for hybrid PV/T: $\theta_c = 40^\circ$, $D = 0.03$m, $C_e = 1.4$
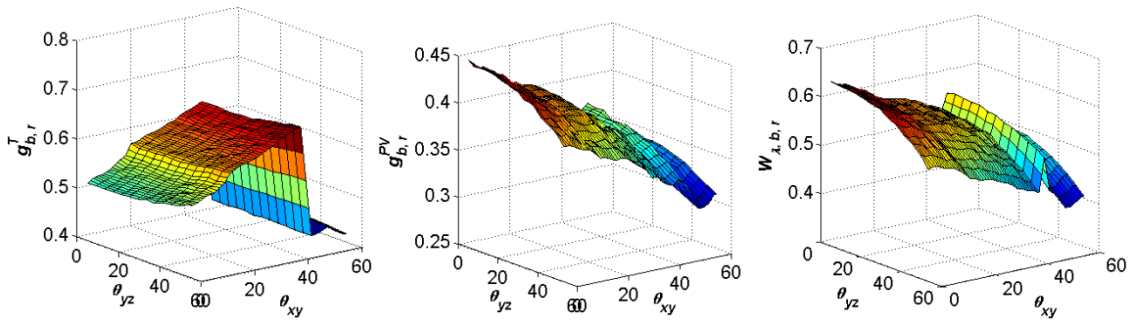
Fig. C.29 MCRT results for hybrid PV/T: $\theta_c = 45^\circ$, $D = 0.03$m, $C_e = 1.2$
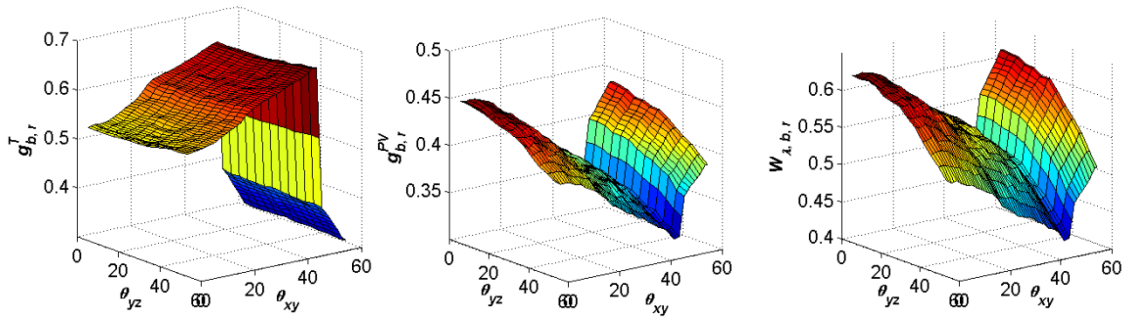

Fig. C.30 MCRT results for hybrid PV/T: $\theta_c = 50^\circ$, $D = 0.03$m, $C_e = 1.2$

113

C.2 Hybrid Solar Window

Figs. C.31-C.35 → Vertical window
Figs. C.36-C.40 → Horizontal skylight
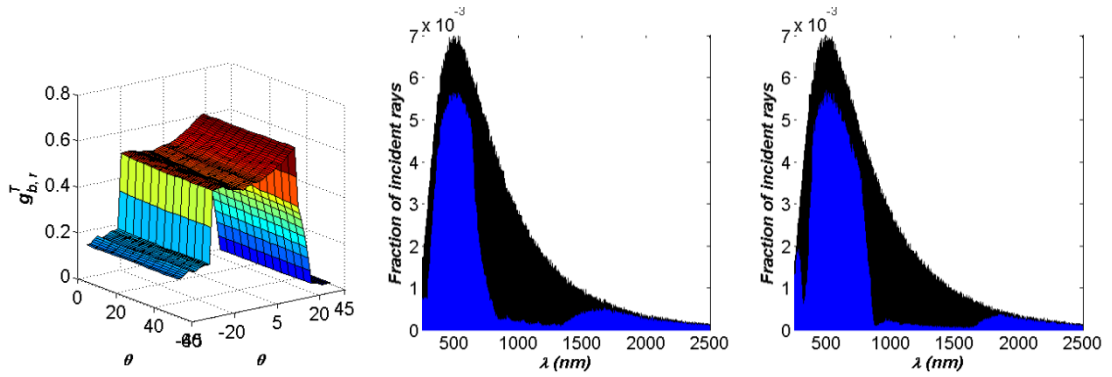
Fig. C.31 MCRT results for vertical window: $\theta_c = 25^o$, $D = 0.016$m
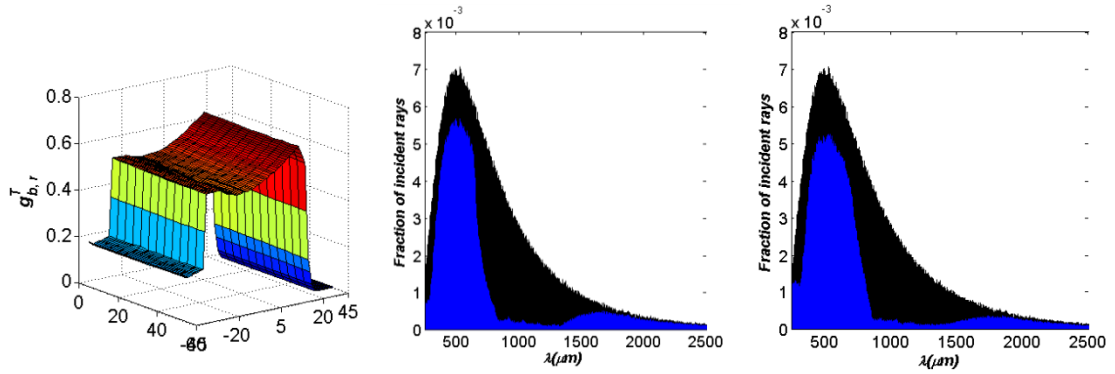
Fig. C.32 MCRT results for vertical window: $\theta_c = 30^o$, $D = 0.016$m
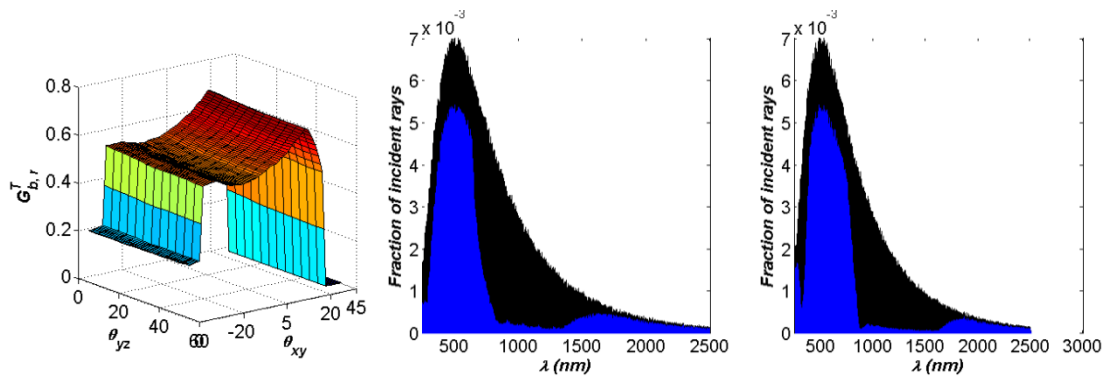

Fig. C.33 MCRT results for vertical window: $\theta_c = 35^o$, $D = 0.016$m

114
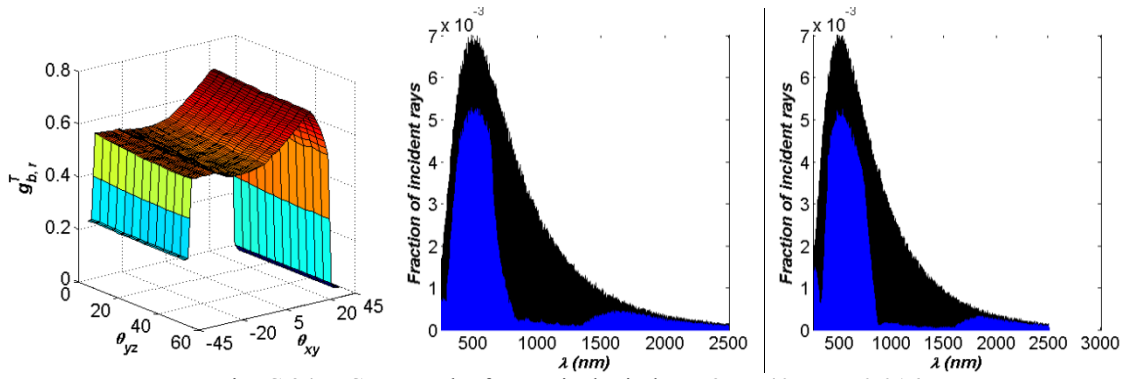
Fig. C.34 MCRT results for vertical window: $\theta_c = 40^\circ$, $D = 0.016$m
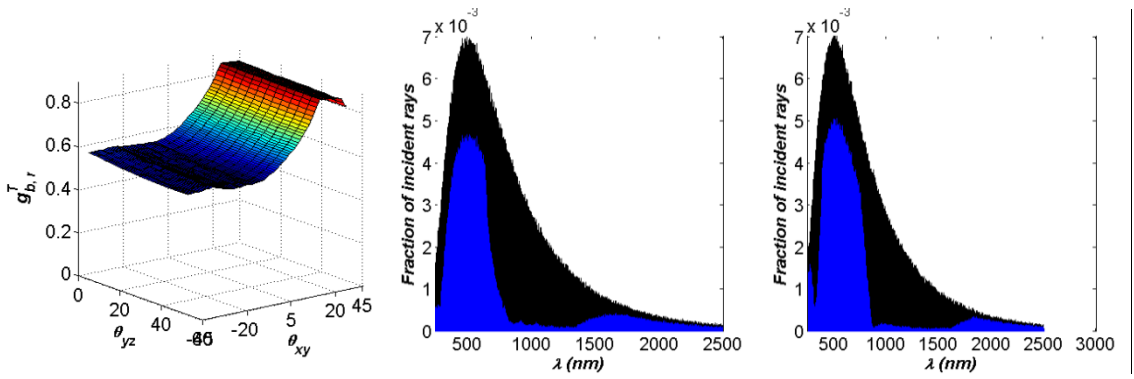
Fig. C.35 MCRT results for vertical window: $\theta_c = 45^\circ$, $D = 0.016$m
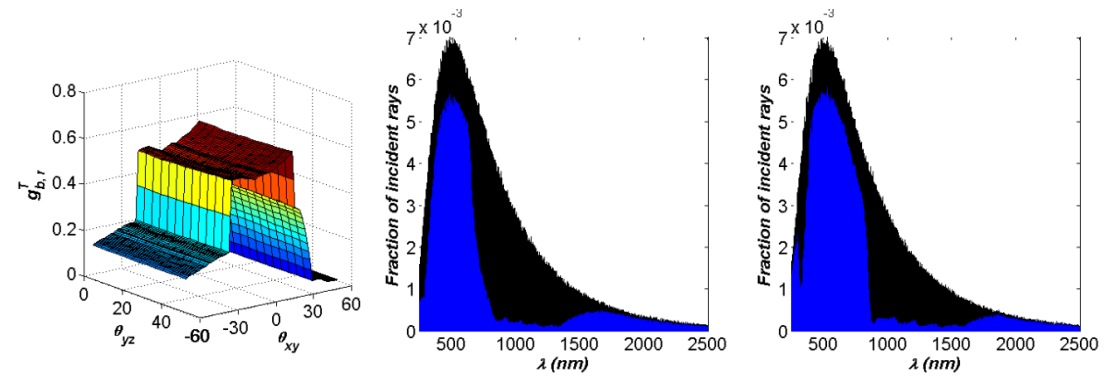
Fig. C.36 MCRT results for horizontal skylight: $\theta_c = 25^\circ$, $D = 0.016$m
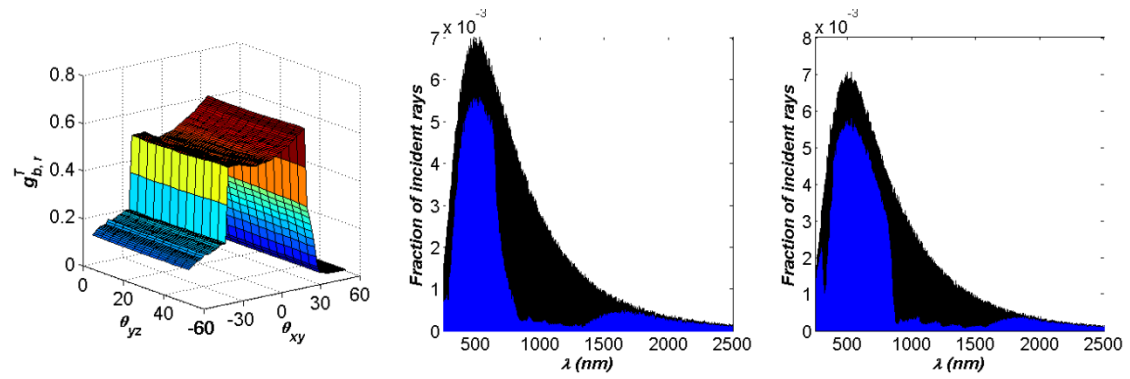
Fig. C.37 MCRT results for horizontal skylight: $\theta_c = 30^\circ$, $D = 0.016$m

115
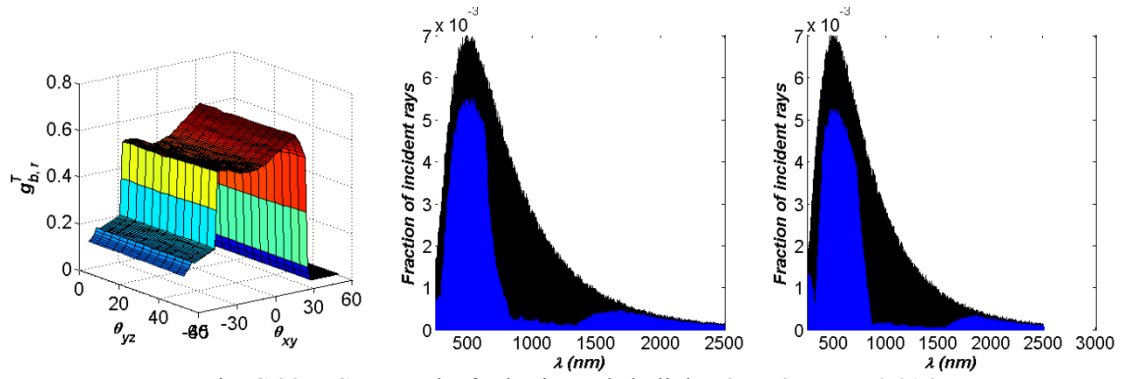
Fig. C.38 MCRT results for horizontal skylight: $\theta_c = 35°$, $D = 0.016$m
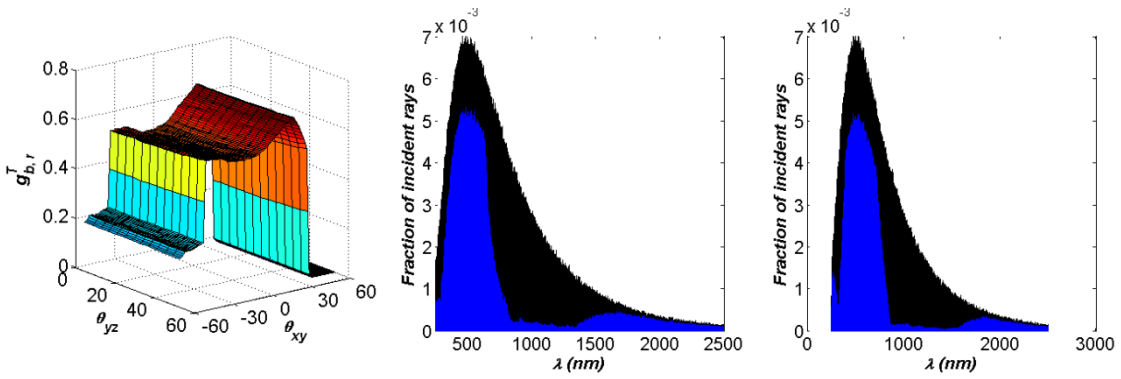

Fig. C.39 MCRT results for horizontal skylight: $\theta_c = 40°$, $D = 0.016$m
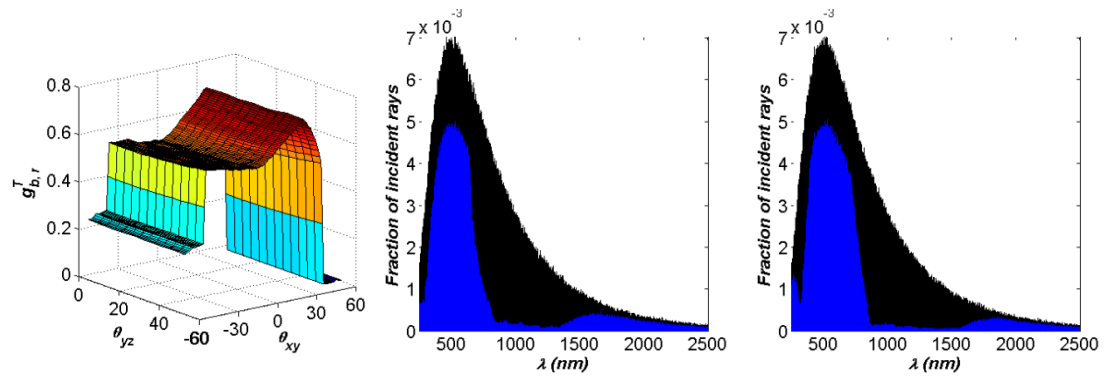
Fig. C.40 MCRT results for horizontal skylight: $\theta_c = 45°$, $D = 0.016$m

Appendix D

Additional notes on the thermal model

D.1 Convective heat transfer within the CPC cavity

Due to the non-standard shape of the CPC cavity, it is modeled as an annular region between eccentric horizontal cylinders. The overall mean convective heat transfer from the cylindrical absorber is calculated using correlations developed by Kuehn and Goldstein [1] for the conduction, laminar boundary-layer flow, and turbulent boundary-layer flow regimes. The correlation is valid for Rayleigh numbers upto 10^{10} and a wide range of Prandtl numbers. The Nusselt number for the convection part is given by

$$Nu_{D,conv} = \frac{2}{\ln\left(\frac{1+{}^2/Nu_i}{1+{}^2/Nu_o}\right)} \tag{D.1}$$

where

$$Nu_i = \left\{\left[0.518 Ra_D^{\frac{1}{4}} f_2(Pr)\right]^{15} + \left(0.1 Ra_D^{\frac{1}{3}}\right)^{15}\right\}^{\frac{1}{15}} \tag{D.2}$$

$$Nu_o = \left(\left\{\left[\left(\frac{2}{1-e^{-\frac{1}{4}}}\right)^{\frac{5}{3}} + \left[0.587 f_3(Pr) Ra_{D_o}^{\frac{1}{4}}\right]^{\frac{5}{3}}\right]^{\frac{3}{5}}\right\}^{15} + \left(0.1 Ra_{D_o}^{\frac{1}{3}}\right)^{15}\right)^{\frac{1}{15}} \tag{D.3}$$

with

$$f_2(Pr) = \left[1 + \left(\frac{0.559}{Pr}\right)^{\frac{3}{5}}\right]^{-\frac{5}{12}} \tag{D.4}$$

$$f_3(Pr) = \left[\left(1 + \frac{0.6}{Pr^{0.7}}\right)^{-5} + (0.4 + 2.6 Pr^{0.7})^{-5}\right]^{-\frac{1}{5}} \tag{D.5}$$

For the conduction part, which is dominant as Rayleigh number approaches zero, the Nusselt number is given by

$$Nu_{D,cond} = \frac{2}{\cosh^{-1}\{[D^2 + D_o{}^2 - (D_o - D)^2 \tilde{\epsilon}^2]/2DD_o\}}$$

(D.6)

$\tilde{\epsilon}$ is the eccentricity of the cylinders normalized with respect to $\left(\frac{D_o - D}{2}\right)$. The overall Nusselt number based on the absorber tube diameter is given by

$$Nu_D = \left[\left(Nu_{D,conv}\right)^{15} + \left(Nu_{D,cond}\right)^{15}\right]^{\frac{1}{15}}$$

(D.7)

The effective diameter D_o is taken to be equal to the length of the major axis of the CPC, either the height or the width. The center of the outer cylinder is fixed graphically to approximate the shape of the CPC. An example of the approximation procedure is shown in Fig. D.1.
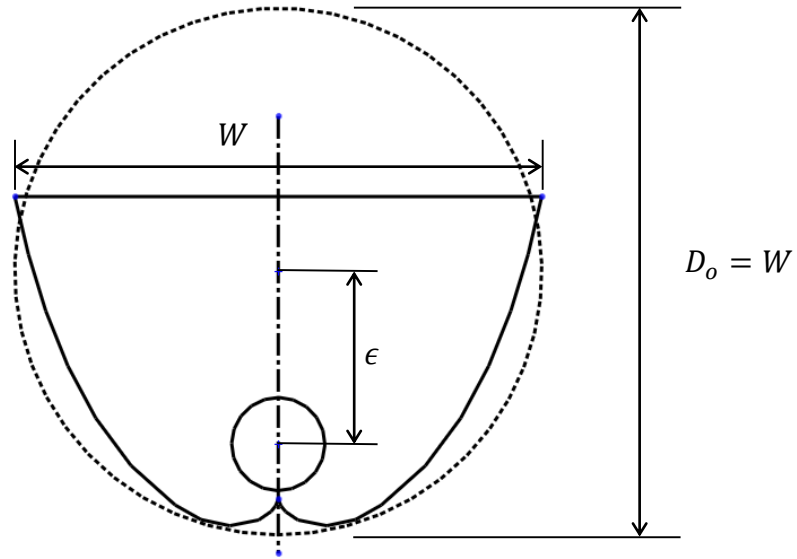

Fig. D.1 The absorber tube and the CPC cavity approximated as eccentric cylinders

The convective heat transfer coefficient from the absorber to the cover, $h_{c,a-c}$, and from the absorber to the CPC, $h_{c,a-m}$, are then calculated using equation (C.8) and (C.9). An empirical factor, f_{rat} for CPC geometries of different concentrations from 1.56 to 4.13, with an inclination of up to 30° is proposed in [2]. A value of 0.55 is used for f_{rat} for the present case. The maximum inclination of the geometries used for the present study is 45° and the assumption of the validity of f_{rat} for this case is likely to create some uncertainty in the results.

$$\frac{h_{c,a-m}}{h_{c,a-c}} = f_{rat} \tag{D.8}$$

$$h_{c,a-c} = \frac{Nu_D k}{D}\left(\frac{1}{1+f_{rat}}\right) \tag{D.9}$$

While calculating the U-factor of the window (Section 3.4.3), the absorber tube is considered to be in thermal equilibrium with the surrounding air in the cavity. In this case, the CPC is considered to be a vertical cavity having an effective gap thickness d_g equal to 90% of the maximum gap thickness. Based on a Rayleigh number for the gap thickness of the vertical cavity,

$$Nu = (Nu_1, Nu_2)_{max} \tag{D.10}$$

$$Nu_1 = 0.0673838 Ra^{1/3} \qquad 5\times10^4 < Ra \tag{D.11}$$

$$Nu_1 = 0.028154\ Ra^{0.4134} \qquad 10^4 < Ra \leq 5\times10^4 \tag{D.12}$$

$$Nu_1 = 1 + 1.7596678\text{E-}10\ Ra^{2.2984755} \qquad Ra \leq 10^4 \tag{D.13}$$

$$Nu_2 = 0.242\left(\frac{Ra}{H_w/d_g}\right)^{0.272} \tag{D.14}$$

where H_w is the height of the window.

D.2 Radiative heat transfer within the CPC cavity

The radiative heat transfer coefficients from the absorber tube to the CPC reflector and the cover, and from the reflector to the cover are derived in [4], based on the CPC geometry, possibility of multiple reflection events, and the optical properties of the cover, absorber and the reflector material. The effective emissivities for radiative heat transfer between different components are given by -

$$\varepsilon_{a-c} = \frac{\varepsilon_a \varepsilon_c \rho_m^{n_i}}{1-\rho_m^{2n_i}\rho_a\rho_c} \tag{B.10}$$

$$\varepsilon_{a-m} = \frac{1-\rho_m^{n_i}\rho_c}{1-\rho_m^{2n_i}\rho_a\rho_c}(1-\rho_m^{n_i})\varepsilon_a \tag{B.11}$$

$$\varepsilon_{m-c} = \varepsilon_c \left[\frac{1+\rho_m^{n_i}\rho_a}{1-\rho_m^{2n_i}\rho_a\rho_c}(1-\rho_m^{n_i}) + \frac{1-\rho_m^{n_o}}{1-\rho_m^{n_i}\rho_c}\left(\frac{A_c-A_a}{A_a}\right)\right] \tag{B.12}$$

n_i represents is the average number of reflections a ray undergoes when it is launched into the CPC within the CPC acceptance angle. n_o is the average number of reflections when a ray is launched into the CPC at an angle outside the acceptance angle. Both these quantities are obtained from Mote Carlo ray-tracing for each geometry. The properties of the cover, absorber tube and the wavelength selective film on acrylic for the infrared spectrum are listed in Table B.1.

Table B.1 Optical properties of the CPC components for re-radiation in the IR

	ε	ρ	τ
Cover	0.84	0.11	0.05
CPC/Selective film	0.85	0.12	0.03
Absorber	0.1	0.9	0

D.3 Thermophysical properties of working fluids

Air [5]

1. Thermal conductivity (W/mK)

k = -2.276501E-3 + 1.2598485E-4T – 1.4815235E-7T^2 + 1.73550646E-10T^3 – 1.066657E-13T^4 + 2.47663035E-17T^5

2. Specific heat capacity (kJ/kg-K)

c_p = 1.03409 – 0.284887E-3T + 0.7816818E-6T^2 – 0.4970786E-9T^3 + 0.1077024E-12T^4

3. Dynamic viscosity (Ns/m^2)

μ = -9.8601E-1 + 9.80125E-2T – 1.17635575E-4T^2 + 1.2349703E-7T^3 – 5.7971299E-11T^4

The density of air was calculated from the ideal gas law at atmospheric pressure.

Ethylene glycol (40% v/V) aqueous solution [6]

1. Thermal conductivity (W/mK)

k = -0.2581 + 0.0037T – 5e-6T^2

2. Specific heat capacity (kJ/kg-K)

c_p = 2486.9 + 3.3498T

References

[1] Kuehn, T. H., Goldstein, R. J., 1976, "Correlating Equation for Natural Heat Transfer between Horizontal Circular Cylinders," Int. J. Heat Mass Transfer, Vol. 19, pp. 1127-1134

[2] Prapas, D. E., Norton, B., and Probert, S. D., 1987, "Thermal Design of Compound Parabolic Concentrating Solar-Energy Collectors," Journal of Solar Energy Engineering,109(2), pp.161-168.

[3] Wright, J.L., 1996. A Correlation to Quantify Convective Heat Transfer Between Vertical Window Glazings. 102, Pt. 1, 940-946.

[4] Rabl, A., 1976, "Optical and Thermal Properties of Compound Parabolic Concentrators," Solar Energy, 18(6), pp. 497-511.

[5] Rohsenow, W. M., Hartnett, J. P., Cho, Y. I., 1998, Handbook of Heat Transfer, Third Edition, McGraw-Hill Professional Publishing

[6] WEBA Technology, Glycol Based Heat Transfer Fluid Technical Manual, http://www.webacorp.com/HTF-Manual.pdf, last accessed 5/1/2013

Appendix E

Uncertainty Analysis

This appendix provides the uncertainty in measured and calculated quantities, including both bias and precision error. The Root-Sum-of-Squares (RSS) [1] method was used for calculating the propagation of error in calculated quantities, resulting from individual measurements x_i. Let R be a calculated quantity that is a function of n measured quantities, x_i having an uncertainty Δx_i.

$$R = f(x_1, x_2, \ldots, x_n) \qquad \text{(E.1)}$$

The uncertainty in the calculated quantity is given by

$$\Delta R = \sqrt{\sum_{i=1}^{n} \theta_i \Delta x_i} \qquad \text{(E.2)}$$

$$\theta_i = \frac{\partial R}{\partial x_i} \qquad \text{(E.3)}$$

Measured quantities

All instrument output signals were measured using a Agilent 34970A Data Acquisition Unit. The has an accuracy of $\pm 0.0035\%$ of the reading + 0.0005% of the range for voltage measurement, which is negligible in comparison to the uncertainty in the instruments. Table E.1 lists the uncertainty in difference measured variables. Table E..2 lists the uncertainty in thermophysical properties of the fluid due to the uncertainty in measurement of temperature. Table E.3 lists the uncertainty in quantities calculated from the measured variables.

References

[1] Figliola, R. S., Beasley, D. E., 1995, Theory and Design for Mechanical Measurements, Second Edition, John Wiley and Sons, New York, NY.

Table E.1 Uncertainty in measured quantities

Variable	Instrument	Absolute Uncertainty	Relative Uncertainty
L B	Tape measure	± 2mm	$\pm 0.26\%$ $\pm 0.25\%$
$G_{b,\hat{n}}$	Eppley Model NIP Pyreheliometer	$\pm 1.2\%$	$\pm 1.2\%$
G_h $G_{d,h}$	Eppley Model PSP Pyranometer	$\pm 1.5\%$	$\pm 1.5\%$
T_{fi}	Type T thermocouple	$\pm 0.5^{\circ}$C	$\pm 1.8\%$-± 2.1
T_{fo}			$\pm 1.7\%$-± 1.9
T_b			$\pm 1.9\%$-± 2.2
$\dot{m}$	Micromotion Model D40 mass flow meter	$\pm 0.2\%$+0.0000667 kg/s	$\pm 1\%$

Table E.2 Uncertainty in thermophysical properties for ethylene glycol/water solution

Property	Equation	Relative Uncertainty
c_p	2486.9 + 3.3498T	<0.05% (Negligible)

Table E.3 Uncertainty in calculated values, obtained using root-sum-of-squares method

Variable	Uncertainty calculation	Relative Uncertainty
Aperture area $A_c = L \times B$	$\left(\dfrac{\Delta A_c}{A_c}\right)^2 = \left(\dfrac{\Delta L}{L}\right)^2 + \left(\dfrac{\Delta B}{B}\right)^2$	$\pm 0.36\%$
Total diffuse radiation on vertical $G_{d,v} = \dfrac{G_{d,h}}{2} + \dfrac{0.2 G_h}{2}$	$\left(\Delta G_{d,v}\right)^2 = \left(0.5\Delta G_{d,h}\right)^2 + \left(0.1\Delta G_h\right)^2$	$\pm 1.5\%$
Total radiation on vertical $G = G_{b,v} + G_{d,v}$	$\left(\Delta G_v\right)^2 = \left(\Delta G_{b,v}\right)^2 + \left(\Delta G_{d,v}\right)^2$	$\pm 1\%$-$\pm 1.5\%$
Mass flow rate per unit aperture area $\dot{m} = \dfrac{\dot{m}}{A_c}$	$\left(\dfrac{\Delta \dot{m}}{\dot{m}}\right)^2 = \left(\dfrac{\Delta \dot{m}}{\dot{m}}\right)^2 + \left(\dfrac{\Delta A_c}{A_c}\right)^2$	$\pm 1.1\%$
Temperature rise through the collector $\Delta T_f = T_{fo} - T_{fi}$	$\left(\Delta T_f\right)^2 = \left(\Delta T_{fo}\right)^2 + \left(\Delta T_{fi}\right)^2 = 0.7^{\circ}$C	$\pm 1\%$-$\pm 35\%$ (average $\pm 26\%$)
Useful energy $Q_u = \dot{m} c_p \Delta T_f$	$\left(\dfrac{\Delta Q_u}{Q_u}\right)^2 = \left(\dfrac{\Delta \dot{m}}{\dot{m}}\right)^2 + \left(\dfrac{\Delta c_p}{c_p}\right)^2 + \left(\dfrac{\Delta\left(\Delta T_f\right)}{\Delta T_f}\right)$	$\pm 21\%$-$\pm 35\%$ (average $\pm 26\%$)